UNIVERSITÀ
DEGLI STUDI
FIRENZE

DOTTORATO DI RICERCA IN
INGEGNERIA INDUSTRIALE
(*Indirizzo in SCIENZE ED IGEGNERIA DEI MATERIALI*)

CICLO XVIII

COORDINATORE
Prof. De Lucia Maurizio

Magnetic Nanostructures: a promising approach towards RE-free permanent magnets

Settore Scientifico Disciplinare ING-IND/22

Dottoranda
Dott.ssa Lottini Elisabetta

Tutori
Prof. Caneschi Andrea

Dott. Sangregorio Claudio

Coordinatore
Prof. De Lucia Maurizio

Anni 2012/2015

Table of contents

Chapter 1

Introduction

During the last decades, due to the demand of new generation high-technology materials, the research activity focused on nanomaterials has increased exponentially. Currently, the scientific community is achieving a progressively deeper ability in designing, synthesizing and manipulating structures at the nanoscale, revealing their excellent and unique optical, electrical, catalytic, mechanical, biological and magnetic properties. Such properties arise from the finely tuned nanostructure of these materials, e.g. size, shape or combination of different nano-sized materials. However, the fabrication and characterization of nanomaterials remain challenging, and considerable efforts are required to explore synthetic procedures for innovative nanostructured materials. Moreover, the great interest in nanosystems research can be understood not only in terms of fundamental knowledge of materials properties, but also considering the large variety of applications such as medicine and pharmacology, data storage, refrigeration, electronics, optics, ceramics and insulators industry, mechanics, sensors, catalysis, polymers industry, energy storage and production (solar cells, battery, permanent magnet, etc), as schematically summarized in Table 1.1. [1]

The unique properties of nanomaterials arise from their reduced size. In fact, below 100 nm several properties of matter are strongly altered with respect to their bulk counterparts and often novel phenomena are observed. As the material size reduces to a comparable size respect to the characteristic length scale (e.g., electron mean free path, domain wall width, diffusion length, superconducting coherence length, etc.), indeed, *finite-size effects* in the related physical or chemical properties occur. [25] Apart from *finite-size effects*, the reduction of the dimensions of the material to the nanoscale implies a dramatic increase in the fraction of atoms located at the surface, whose behaviour is strongly affected by alterations in coordination number, symmetry of the local environment and matrix interaction. [25,26] The combination of *finite-size effects* and *surface effects* leads to various and complex modifications of materials properties, which enhance their versatility.

Table 1.1: Schematic classification of main applications for nanoparticles.

Area of interest	Application Examples
Biological	Diagnosis (fluorescence labelling, contrast agents for magnetic resonance) [2–4] Medical therapy (drug delivery, hyperthermia) [5–7]
Chemical	Catalysis (fuel cells, photocatalytic devices and production of chemicals) [8–10]
Electronic	High performance delicate electronics [11] High performance digital displays [12,13]
Energetic	High performance batteries (longer-lasting and higher energy density) [14] High-efficiency fuel cells [15] High-efficiency solar cells [16]
Magnetic	High density storage media [17] Magnetic separation [18] Highly sensitive biosensing [19] Permanent magnets [20]
Mechanical	Mechanical devices with improved wear and tear resistance, lightness and strength, anti-corrosion abilities [11,21]
Optical	Anti-reflection coatings [22] Specific refractive index for surfaces [23] Light based sensors [24]

Different nanomaterials can be classified according to their dimensionality (*D*): [27]

- *Quasi-zero-dimensional* (*0D*): nanoparticles, clusters and quantum dots with none of their three dimensions larger than 100 nm (three dimensions in the nanoscale).
- *One-dimensional* (*1D*): nanowires and nanotubes with two dimensions in the nanoscale.
- *Two-dimensional* (*2D*): thin films and multilayers with only one dimension in the nanoscale.
- *Three-dimensional* (*3D*): mesoporous structures and 3D arrays of nanoparticles.

Among nanostructured systems, the present work is focused on quasi-zero-dimensional materials and, in particular, on magnetic nanoparticles. These nanoparticles are usually composed by magnetic transition metals (iron, cobalt, manganese and nickel) and/or rare-earth elements (samarium, lanthanum, niobium, etc.) which can be present as metals, metallic alloys, oxides, other related ceramic compounds (nitrides, borides, etc.) or organometallic compounds. [28] Normally their structure is crystalline, although also amorphous phases can exhibit peculiar magnetic behaviours. The fundamental motivation for the study of magnetic nanoparticles is the considerable modification in the magnetic properties occurring as the material is reduced to the nanoscale, particularly when the

critical length which mainly governs the physical properties of the system (e.g., domain wall width) is comparable to or larger than the particle size. Probably, the single domain magnetic regime and the related superparamagnetic behaviour, which are a direct consequence of finite-size effects, are the best known features of magnetic nanoparticles. [29–31] On the other hand, it has been demonstrated that surface effects (large surface-to-volume ratio) and inter-particle and particle-matrix interactions (dipole-dipole interaction, exchange-coupling, etc.) also play an important role in the final magnetic properties of the system, leading to some effects such as high field irreversibility, high saturation field, extra anisotropy contributions or shifted loops after field cooling. [32–36] The magnetic properties of nanoparticles are also determined by many further factors, such as chemical composition, crystalline structure, particle size, shape and morphology. In principle, by changing one or more of these parameters it is possible to control, to a certain extent, the magnetic characteristics of the material. Therefore, during the last decade the range of application of magnetic nanoparticles has remarkably increased thanks to the combination of the size-dependent properties of magnetic nanoparticles and the possibility of tuning them through the control of synthetic parameters . In particular, magnetic nanoparticles are currently used in magnetic seals in motors, [37] magnetic inks, [38] magnetic recording media, [17] magnetic separation, [18] magnetic resonance contrast media (MRI), [4] highly sensitive biosensing assays, [19] drug delivery, [39] and hyperthermia. [7]. Moreover, magnetic nanoparticles have shown remarkably promising properties, which can be exploited in the permanent magnet research area.

Permanent magnets are key elements of many technological devices that have a direct use in several aspects of contemporary life because of their role in the transformation of energy from one form to another. [40,41] Indeed, the possibility of maintaining large magnetic flux both in absence of an applied magnetizing field and upon modification of the environment (demagnetizing field, temperature, etc.) is a unique feature which allows permanent magnet to be used in a wide variety of applications, as summarized in Table 1.2.

Table 1.2: Schematic classification of applications for permanent magnets and list of some examples. [42]

Category	Application Examples
Alternative energy	Energy storage systems Power generation systems Wind, wave, tidal power systems
Appliances	Household appliance motors and air conditioners Security systems Water pumps
Automotive and transportation	Electric bicycles and hybrid/electric vehicles Electric fuel pumps Starter motors and brushless DC motors

Computer and office automation	Hard disk drive and CS-ROM spindle motors Printer and fax motors Voice coil matron and pick-up motors
Consumer electronics	Cell phones Speakers, microphones and headsets VCRs, cameras and DVD player
Factory automation	Magnetic coupling and bearings Motors, servo motors and generators Pumps
Medical industry	MRI equipment Surgical tools and medical implants
Military	Communication systems, radar, satellites Vehicles, watercraft, avionics Weapon systems, precision-guided munitions

The potential applications of a permanent magnet are determined by the energy density that can be stored in the material and which is described in term of *maximum energy product*, *(BH)max*, (see Figure 1.1). In particular, $(BH)_{max}$ is an expression of the combination of the operative flux density (the magnetic induction, in working condition) and the magneto-motive force (the resistance of the magnet to demagnetization, *i.e.* the coercive force).

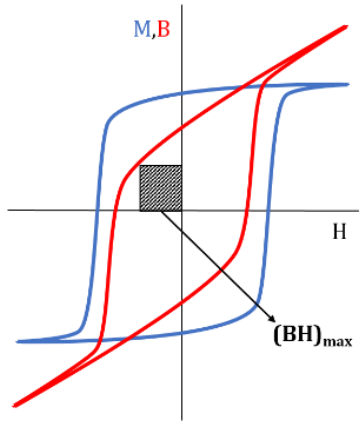

Figure 1.1: Typical magnetization (*M,* blue curve) and magnetic induction (*B,* red curve) dependence on the applied field (H) for a permanent magnet. The maximum energy product ($(BH)_{max}$) corresponds to the area of the largest rectangle that can be inscribed under the demagnetizing branch of the *B(H)* curves at negative fields (the second quadrant).

The materials exhibiting large magnetic induction values are mainly transition metals Fe, Co and Ni and their alloys but, on the other hand, they have low magnetic anisotropy, and consequently low coercive force. Higher magnetic anisotropy requires materials with non-centrosymmetric structures comprising ions with high values of orbital moment. The materials with the largest magnetic performance are composed of rare-earths (RE) and

transition metals alloys, such as $Nd_2Fe_{14}B$ and $SmCo_5$, where the large magnetic induction values of transition metals are combined with the high magnetic anisotropy of RE. More in detail, as reported in Figure 1.2, the energy product of RE-based permanent magnets is between 100-400 kJm^{-3}, while it is much smaller for the rest of magnetic materials (ca. 30 kJm^{-3} for ferrites and 45 kJm^{-3} for Alnico).

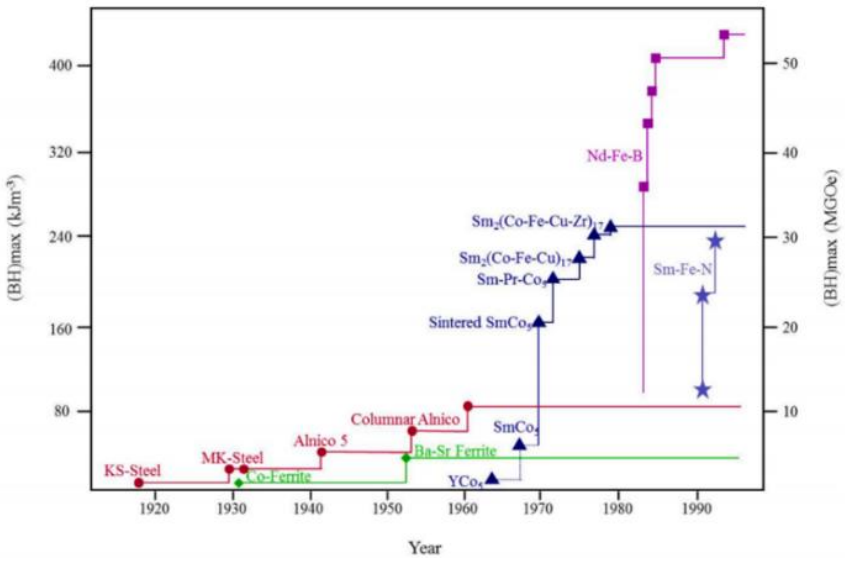

Figure 1.2: The development of permanent magnets in the 20th Century. $(BH)_{max}$ has improved steadily, doubling every 12 years. [41]

From these considerations, it emerges that RE-based magnets are required for high performance applications or microscalable devices of high technological impact due to their performance-to-size ratio. Therefore, many industries depend critically on the production of such type of magnets. This is a major problem for E.U., and other developed country as most of the mines and reserves are under the monopoly of mainly only one country (China). As a consequence, the production of devices containing RE elements is potentially subject to price fluctuations which may arise from restrictive export politics. Actually, the possibility of sudden price oscillations come into reality in 2011 during the so-called "RE-crisis" when, as reported in Figure 1.3, the cost increase of RE exceeded 600% in few months, after some restrictions imposed to the exportation in RE-based raw-materials towards Japan. Besides, RE elements refinement requires environmental harmful processes whose reduction efforts are expected to further raise their price. Such fluctuations are becoming frighteningly relevant considering the large range of applications of RE, particularly those related to automotive industry (e.g., components of motors, alternators, gearboxes), renewable energy (e.g., components of wind and hydroelectric turbines) and data storage (e.g., hard disk drive), which are exponentially growing. The global market for permanent magnets is expected to move 14 billion Euros in 2020.

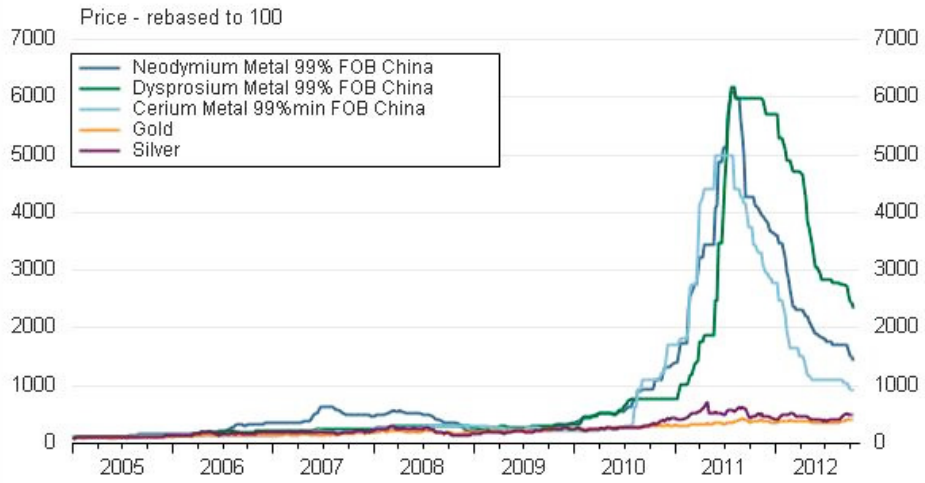

Figure 1.3: Rare earths *vs.* gold and silver price increases from 2005 to 2012: 2011 "RE-crisis" is delineated by peaks in Nd, Dy and Ce price rise.

Therefore, it does not surprise if the report of the Ad-hoc Working Group of European Community, on defining critical raw materials depicts RE elements as the group with the highest supply risk. [43] Hence, the criticality of RE has brought forward that it is of great strategic, geographic and socio-economic importance to consider the development of permanent magnets without or with reduced amounts of these elements. Starting from these remarks, the European Union's Research and Innovation funding programme is supporting several research projects investigating different strategies for rare-earth elements substitution or reduction in permanent magnet application. [44–47]

Importantly, a relevant number of key technologies requires magnets with moderate energy product within the range of 35-100 kJm^{-3}. This "no man's land" application area includes fundamental fields such as diverse components for transport (mainly automotive industry) and energy (with new generation of friendly environmental platforms such as wind turbines or photovoltaics, and more classical ones such as refrigeration motors). Currently, this gap is filled by low-performing RE-based magnets simply because ferrites energy products reach only the lower limit. However, it has been shown for "already effective" RE-based permanent magnets that their performance can be significantly improved through their microstructure and the composition optimization. [48,49] Therefore, it can be argued that the same approach would result in similar improvements on the magnetic properties of transition metal-based nanostructures. Consequently, the research on both nanostructured ferrites and transition metal alloys has grown exponentially, with the aim of understanding the correlation between properties and material nanostructure and achieving enhanced performances for permanent magnet applications. [20,28,40,42,50–54]

The present work moves within this contest, as it addresses the design and development of novel RE-free nanostructured materials for permanent magnet applications. In particular,

ferrite-based magnetic materials doped with transition metal ions (cobalt, manganese, zinc) are studied with particular attention to the correlation between their magnetic properties and nanostructure. The study of ferrite-based nanomaterials was carried out considering two different strategies:

(a) In a first step the magnetic behaviour of single-phase ferrites nanocrystals with enhanced anisotropy was analysed, in order to better understand the correlation between the final properties and particle size, shape, crystallinity, composition, etc. To carry out this task, we prepared monodisperse nanocrystals with controlled size, shape and stoichiometry and studied the size/shape-dependent evolution of their magnetic properties.

(b) In a second step, we prepared hybrid bi-magnetic core|shell nanoparticles) focussing on the aftermath and required conditions of exchange-coupling establishment between the two moieties. In particular, crystalline nanocomposites presenting spring-magnet or exchange-bias behaviour were analysed in order to assess the possibility of improving the material performances by control of the interface quality as well as of the relative amount or size of the two magnetic phases.

Within these approaches, different chemical-physical effects cooperate together to define material magnetization and anisotropy, and thus the performances as permanent magnets. The main properties which we want to exploit can be schematized as follows:

(I) *Size effects.* Reducing the particle size to the single domain regime, particularly close to the single-to-multidomain threshold, the coercivity increases enhancing the performances of the material.

(II) *Magnetocrystalline anisotropy* of highly anisotropic metal oxides can be transmitted to low-anisotropy metal with large magnetic induction values through exchange-coupling and interface effects.

(III) *Chemical composition.* Through different doping of ferrite nanoparticles it is possible to modify directly the material properties, increasing in turn magnetic anisotropy, saturation magnetization, ordering temperature and structural features.

(IV) *Surface anisotropy.* With magnets formed by nanoparticles (*0D* materials) the overall contribution of the surface anisotropy is enhanced leading to higher average anisotropy. In addition, the creation of proper interfaces in specific exchange-coupled systems could be used to tune exchange-coupling interaction optimizing the material performances.

The present work is structured in the following sections:

Chapter 2. A brief summary of the theory of magnetism and magnetic materials is presented with particular attention to nanostructured systems and related aspects such as *size-effects* and *interaction effects*.

Chapter 3. The preparation of *0D* materials is discussed both from the theoretical point of view and regarding technical aspects. In particular, bottom-up colloid chemical synthesis is described considering different synthetic procedures.

Chapter 4. The synthesis and characterization of narrowly distributed cobalt ferrite nanocrystals in a broad range of particle size and fixed stoichiometry is reported. Consequently, the size/shape-dependence of magnetic properties of nanoparticles is discussed in terms of their potential applications in the field of permanent magnets.

Chapter 5. The synthesis of core|shell bi-magnetic nanoparticles formed by cubic spinel ferrites doped with different divalent ions (cobalt, manganese and zinc) is investigated. Subsequently magnetic characterization is discussed in order to assess the establishment of exchange-coupling interactions to obtain spring-magnets. In addition, the magnetic behaviour of nanocomposites based on cobalt ferrite and cobalt-iron alloy is analysed in order to investigate the spring-magnet behaviour under different coupling regimes.

Chapter 6. The synthesis and magnetic properties of core|shell bi-magnetic nanoparticles formed by cobalt ferrite and mixed cobalt-iron monoxide exhibiting exchange-bias is presented. In particular, the exchange-coupling effects are analysed in terms of the size of the cobalt-iron monoxide component. In addition, a detailed investigation is discussed which allows better understanding the mechanism driving the formation of a high quality interface.

Chapter 7. The final section briefly summarizes the main conclusions obtained from the experimental work presented above. These conclusions are then used as a basis for a more general discussion on feasibility of the proposed approach for the realization of RE-free permanent magnets and to comment on its perspective.

References

[1] K.J. Klabunde, Nanoscale Materials in Chemistry, Wiley-Interscience, New York, 2001.

[2] V.A. Sinani, D.S. Koktysh, B.-G. Yun, R.L. Matts, T.C. Pappas, M. Motamedi, et al., Collagen Coating Promotes Biocompatibility of Semiconductor Nanoparticles in Stratified LBL Films, Nano Lett. 3 (2003) 1177–1182. doi:10.1021/nl0255045.

[3] Y. Zhang, N. Kohler, M. Zhang, Surface modification of superparamagnetic magnetite nanoparticles and their intracellular uptake, Biomaterials. 23 (2002) 1553–1561. doi:10.1016/S0142-9612(01)00267-8.

[4] T.-J. Yoon, H. Lee, H. Shao, R. Weissleder, Highly magnetic core-shell nanoparticles with a unique magnetization mechanism., Angew. Chem. Int. Ed. Engl. 50 (2011) 4663–6. doi:10.1002/anie.201100101.

[5] J. Gao, H. Gu, B. Xu, Multifunctional Magnetic Nanoparticles: Design, Synthesis, and Biomedical Applications, Acc. Chem. Res. 42 (2009) 1097–1107. doi:10.1021/ar9000026.

[6] A. Solanki, J.D. Kim, K.-B. Lee, Nanotechnology for regenerative medicine: nanomaterials for stem cell imaging, Nanomedicine. 3 (2008) 567–578. doi:10.2217/17435889.3.4.567.

[7] O. Salata, Applications of nanoparticles in biology and medicine, J. Nanobiotechnology. 2 (2004) 3. doi:10.1186/1477-3155-2-3.

[8] H.L. Xin, J.A. Mundy, Z. Liu, R. Cabezas, R. Hovden, L.F. Kourkoutis, et al., Atomic-Resolution Spectroscopic Imaging of Ensembles of Nanocatalyst Particles Across the Life of a Fuel Cell, Nano Lett. 12 (2012) 490–497. doi:10.1021/nl203975u.

[9] Z. Liu, Y. Qi, C. Lu, High efficient ultraviolet photocatalytic activity of BiFeO3 nanoparticles synthesized by a chemical coprecipitation process, J. Mater. Sci. Mater. Electron. 21 (2010) 380–384. doi:10.1007/s10854-009-9928-x.

[10] A. Murugadoss, P. Goswami, A. Paul, A. Chattopadhyay, “Green” chitosan bound silver nanoparticles for selective C–C bond formation via in situ iodination of phenols, J. Mol. Catal. A Chem. 304 (2009) 153–158. doi:10.1016/j.molcata.2009.02.006.

[11] F.R. Marciano, L.F. Bonetti, R.S. Pessoa, J.S. Marcuzzo, M. Massi, L.V. Santos, et al., The improvement of DLC film lifetime using silver nanoparticles for use on space devices, Diam. Relat. Mater. 17 (2008) 1674–1679. doi:10.1016/j.diamond.2008.03.007.

[12] J.H. Fendler, Chemical Self-assembly for Electronic Applications, Chem. Mater. 13 (2001) 3196–3210. doi:10.1021/cm010165m.

[13] J.E. Millstone, D.F.J. Kavulak, C.H. Woo, T.W. Holcombe, E.J. Westling, A.L. Briseno, et al., Synthesis, Properties, and Electronic Applications of Size-Controlled Poly(3-hexylthiophene) Nanoparticles, Langmuir. 26 (2010) 13056–13061. doi:10.1021/la1022938.

[14] C.D. Wessells, R.A. Huggins, Y. Cui, Copper hexacyanoferrate battery electrodes with long cycle life and high power., Nat. Commun. 2 (2011) 550. doi:10.1038/ncomms1563.

[15] B. Bogdanović, M. Felderhoff, S. Kaskel, A. Pommerin, K. Schlichte, F. Schüth, Improved Hydrogen Storage Properties of Ti-Doped Sodium Alanate Using Titanium Nanoparticles as Doping Agents, Adv. Mater. 15 (2003) 1012–1015. doi:10.1002/adma.200304711.

[16] X. Chen, B. Jia, J.K. Saha, B. Cai, N. Stokes, Q. Qiao, et al., Broadband Enhancement in Thin-Film Amorphous Silicon Solar Cells Enabled by Nucleated Silver Nanoparticles, Nano Lett. 12 (2012) 2187–2192. doi:10.1021/nl203463z.

[17] G. Reiss, A. Hütten, Magnetic nanoparticles: Applications beyond data storage, Nat. Mater. 4 (2005) 725–726. doi:10.1038/nmat1494.

[18] I.S. Lee, N. Lee, J. Park, B.H. Kim, Y.-W. Yi, T. Kim, et al., Ni/NiO Core/Shell Nanoparticles for Selective Binding and Magnetic Separation of Histidine-Tagged Proteins, J. Am. Chem. Soc. 128 (2006) 10658–10659. doi:10.1021/ja063177n.

[19] H. Lee, T.-J. Yoon, R. Weissleder, Ultrasensitive Detection of Bacteria Using Core-Shell Nanoparticles and an NMR-Filter System, Angew. Chemie Int. Ed. 48 (2009) 5657–5660. doi:10.1002/anie.200901791.

[20] G.C. Papaefthymiou, Nanoparticle magnetism, Nano Today. 4 (2009) 438–447. doi:10.1016/j.nantod.2009.08.006.

[21] L. Shi, D.S. Shang, Y.S. Chen, J. Wang, J.R. Sun, B.G. Shen, Improved resistance switching in ZnO-based devices decorated with Ag nanoparticles, J. Phys. D. Appl. Phys. 44 (2011) 455305. doi:10.1088/0022-3727/44/45/455305.

[22] K.C. Krogman, T. Druffel, M.K. Sunkara, Anti-reflective optical coatings incorporating nanoparticles, Nanotechnology. 16 (2005) S338–S343. doi:10.1088/0957-4484/16/7/005.

[23] H. Chen, X. Kou, Z. Yang, W. Ni, J. Wang, Shape- and Size-Dependent Refractive Index Sensitivity of Gold Nanoparticles, Langmuir. 24 (2008) 5233–5237. doi:10.1021/la800305j.

[24] J.N. Anker, W.P. Hall, O. Lyandres, N.C. Shah, J. Zhao, R.P. Van Duyne, Biosensing with plasmonic nanosensors, Nat. Mater. 7 (2008) 442–453. doi:10.1038/nmat2162.

[25] G. Cao, Y. Wang, Nanostructures and Nanomaterials: Synthesis, Properties, and Applications, Second Ed., World Scientific Publishing Co. Pte. Ltd., SingaporeSingapore, 2011.

[26] E. Roduner, Size matters: why nanomaterials are different, Chem. Soc. Rev. 35 (2006) 583. doi:10.1039/b502142c.

[27] N. Taniguchi, On the basic concept of nanotechnology, in: Proc. Int. Conf. Prod. Eng., Japan Society of Precision Engineering, Tokyo, 1974: pp. 18–23.

[28] A.-H. Lu, E.L. Salabas, F. Schüth, Magnetic Nanoparticles: Synthesis, Protection, Functionalization, and Application, Angew. Chemie Int. Ed. 46 (2007) 1222–1244. doi:10.1002/anie.200602866.

[29] D.L. Leslie-Pelecky, R.D. Rieke, Magnetic Properties of Nanostructured Materials, Chem. Mater. 8 (1996) 1770–1783. doi:10.1021/cm960077f.

[30] C.P. Bean, J.D. Livingston, Superparamagnetism, J. Appl. Phys. 30 (1959) S120. doi:10.1063/1.2185850.

[31] M. Knobel, W.C. Nunes, L.M. Socolovsky, E. De Biasi, J.M. Vargas, J.C. Denardin, Superparamagnetism and Other Magnetic Features in Granular Materials: A Review on Ideal and Real Systems, J. Nanosci. Nanotechnol. 8 (2008) 2836–2857.

[32] X. Batlle, A. Labarta, Finite-size effects in fine particles: magnetic and transport properties, J. Phys. D. Appl. Phys. 35 (2002) R15–R42. doi:10.1088/0022-3727/35/6/201.

[33] R.H. Kodama, S.A. Makhlouf, A.E. Berkowitz, Finite Size Effects in Antiferromagnetic NiO Nanoparticles, Phys. Rev. Lett. 79 (1997) 1393–1396. doi:10.1103/PhysRevLett.79.1393.

[34] H. Kachkachi, M. Noguès, E. Tronc, D.A. Garanin, Finite-size versus surface effects in nanoparticles, J. Magn. Magn. Mater. 221 (2000) 158–163. doi:10.1016/S0304-8853(00)00390-5.

[35] M. Knobel, W.C. Nunes, A.L. Brandl, J.M. Vargas, L.M. Socolovsky, D. Zanchet, Interaction effects in magnetic granular systems, Phys. B Condens. Matter. 354 (2004) 80–87. doi:10.1016/j.physb.2004.09.024.

[36] J.. Dormann, D. Fiorani, E. Tronc, On the models for interparticle interactions in nanoparticle assemblies: comparison with experimental results, J. Magn. Magn. Mater. 202 (1999) 251–267. doi:10.1016/S0304-8853(98)00627-1.

[37] M. Zahn, Magnetic Fluid and Nanoparticle Applications to Nanotechnology, J. Nanoparticle Res. 3 (2001) 73–78. doi:10.1023/A:1011497813424.

[38] W. Voit, W. Voit, L. Belova, W. Zapka, K.V. Rao, Application of inkjet technology for the deposition of magnetic nanoparticles to form micron-scale structures, IEE Proc. - Sci. Meas. Technol. 150 (2003) 252–256. doi:10.1049/ip-smt:20030692.

[39] M. Arruebo, R. Fernández-Pacheco, M.R. Ibarra, J. Santamaría, Magnetic nanoparticles for drug delivery, Nano Today. 2 (2007) 22–32. doi:10.1016/S1748-0132(07)70084-1.

[40] O. Gutfleisch, M. a Willard, E. Brück, C.H. Chen, S.G. Sankar, J.P. Liu, Magnetic Materials and Devices for the 21st Century: Stronger, Lighter, and More Energy Efficient, Adv. Mater. 23 (2011) 821–842. doi:10.1002/adma.201002180.

[41] K.J. Strnat, Modern permanent magnets for applications in electro-technology, Proc. IEEE. 78 (1990) 923–946. doi:10.1109/5.56908.

[42] F. Jimenez-Villacorta, L.H. Lewis, Advanced Permanent Magnetic Materials, in: J.M. Gonzalez Estevez (Ed.), Nanomagnetism, One Central Press, 2014: pp. 160–189.

[43] Critical Raw Materials, Eur. Comm., http://ec.europa.eu/growth/sectors/raw-materials/specific-interest/critical/index_en.htm.

[44] NANOPYME, www.nanopyme-project.eu.

[45] ROMEO, http://www.romeo-fp7.eu/romeo.htm.

[46] VENUS, http://www.venusmotorproject.eu/.

[47] REFREEPERMAG, http://refreepermag-fp7.eu/.

[48] S. Sugimoto, Current status and recent topics of rare-earth permanent magnets, J. Phys. D. Appl. Phys. 44 (2011) 064001. doi:10.1088/0022-3727/44/6/064001.

[49] R. Skomski, J.M.D. Coey, Giant energy product in nanostructured two-phase magnets, Phys. Rev. B. 48 (1993) 15812–15816. doi:10.1103/PhysRevB.48.15812.

[50] E.F. Kneller, R. Hawig, The exchange-spring magnet: a new material principle for permanent magnets, IEEE Trans. Magn. 27 (1991) 3588–3560. doi:10.1109/20.102931.

[51] E.E. Fullerton, J. Jiang, S.. Bader, Hard/soft magnetic heterostructures: model exchange-spring magnets, J. Magn. Magn. Mater. 200 (1999) 392–404. doi:10.1016/S0304-8853(99)00376-5.

[52] A. López-Ortega, M. Estrader, G. Salazar-Alvarez, A.G. Roca, J. Nogués, Applications of exchange coupled bi-magnetic hard/soft and soft/hard magnetic core/shell nanoparticles, Phys. Rep. 553 (2015) 1–32. doi:10.1016/j.physrep.2014.09.007.

[53] J. Nogués, J. Sort, V. Langlais, V. Skumryev, S. Suriñach, J.S. Muñoz, et al., Exchange bias in nanostructures, Phys. Rep. 422 (2005) 65–117. doi:10.1016/j.physrep.2005.08.004.

[54] M. Vasilakaki, K.N. Trohidou, J. Nogués, Enhanced magnetic properties in antiferromagnetic-core/ferrimagnetic-shell nanoparticles., Sci .Rep. 5 (2015) 9609. doi:10.1038/srep09609.

Chapter 2

Magnetism in nanostructures

Since this thesis is focused on the investigation of the magnetic behaviour of novel nanostructured materials, in this Chapter the basic concepts needed to understand the physical behaviour of magnetic materials and, particularly, of magnetic nanoparticles, are briefly overviewed.

2.1 Magnetic materials

Any substance gives rise to a response to the application of an external applied field (***H***), known as *magnetic induction* (***B***). The relationship between ***B*** and ***H*** depends on the material and is expressed as (in SI units):

$$\boldsymbol{B} = \mu_0(\boldsymbol{H} + \boldsymbol{M}) \qquad 2.1$$

where μ_0 is the *vacuum permeability* ($\mu_0 = 4\pi \cdot 10^{-7}\ Hm^{-1}$) and ***M*** the *magnetization* of the material. In turn, ***M*** is defined as the material *magnetic moment* (***m***) per unit of volume (V).

$$\boldsymbol{M} = \frac{\boldsymbol{m}}{V} \qquad 2.2$$

The magnetization of the material depends on the applied field and, when it is not too large, ***M*** is proportional to ***H***:

$$\boldsymbol{M} = \chi \boldsymbol{H} \qquad 2.3$$

where χ is the *magnetic susceptibility* and describes the magnetization degree of the material in response to ***H***. The magnetic susceptibility is a property of the material and it is commonly used to classify different magnetic behaviours.

More in detail, the magnetic moment of a material and, thus, its magnetic susceptibility depends on the individual atoms and more precisely on their electrons, which have a

magnetic moment because of their motion. In addition, the nucleus has a small magnetic moment which is negligible compared to that of the electrons. In particular, there are two contributions to the electron magnetic moment: the *orbital moment* ($\boldsymbol{l_e}$), related to electron spatial movement around the atomic nucleus, and the *spin moment* ($\boldsymbol{s_e}$), related to the revolution of the electron around its own axis. The atomic magnetic moment is the vector sum of all its electronic moments and, in accordance with *Pauli exclusion principle*, can give rise to two possibilities:

(I) The magnetic moments of the electrons are so oriented that they cancel one another out and the atom as a whole has no net magnetic moment.
(II) The cancellation of electronic moments is only partial and the atoms is left with a net magnetic moment.

In turn, the magnetic moment of a material is the vector sum of the magnetic moment of constituent atoms. Nevertheless, although each atom has a net magnetic moment, in the absence of an external field the magnetic moments are randomly oriented and the net magnetic moment is zero. However, such representation is appropriate for non-interacting atomic magnetic moments, while in the case of interacting systems a net magnetization can be observed. Indeed, neighbouring magnetic moments are subject to a force, which depends on the relative orientation of the electron spins, i.e. the *exchange force*. In particular, the *exchange interaction energy*, E_{ex}, between two atoms *i* and *j* can be written as follows:

$$E_{ex} = -2J_{ex}\boldsymbol{S_i}\boldsymbol{S_j} = -2J\boldsymbol{S_i}\boldsymbol{S_j}cos\varphi \qquad 2.4$$

where J_{ex} is the *exchange integral* and $\boldsymbol{S}$ the spin angular momentum. If J_{ex} is positive, E_{ex} is minimized when the spins are parallel ($cos\varphi = 1$); if J_{ex} is negative, E_{ex} has minimum when the spins are antiparallel ($cos\varphi = -1$). Therefore, the sign and value of J_{ex}, which depends on the nature and arrangement of interacting atoms, gives rise to different ordered magnetic materials. [1]

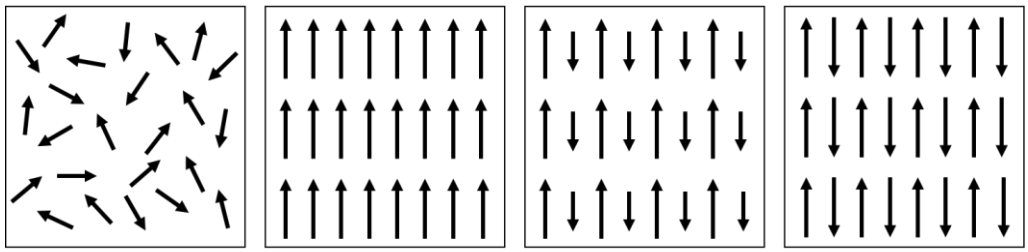

Figure 2.1: Schematic description of magnetic moment order in magnetic materials.

2.1.1 Diamagnetic materials

In the presence of an applied field, all atoms display the *diamagnetic effect*; i.e., a change in the orbital motion of the electrons producing a field opposing to the external one. In fact, when the magnetic field is applied, extra currents are generated in the atoms by electromagnetic induction. In accordance with the *Lenz law*, the current generates an induced magnetic moment proportional to the applied field and with opposite direction. Thus, the magnetic susceptibility of diamagnetic materials is negative (Equation 2.3). Moreover, because of the nature of the diamagnetic effect, χ is independent of the magnetic field and temperature (see Figure 2.2).

However, diamagnetism is such a weak phenomenon that only those atoms that have no net magnetic moment, i.e., atoms with completely filled electronic shells, are classified as diamagnetic. In other materials the diamagnetism is overshadowed by the much stronger interactions between atomic magnetic moments and applied field.

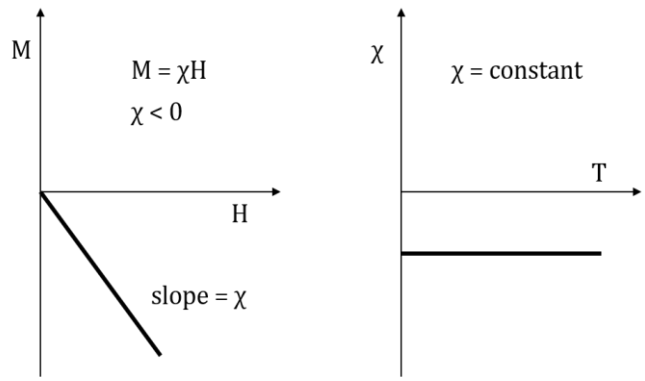

Figure 2.2: Field dependence of magnetization of diamagnetic materials (left) and temperature dependence of the magnetic susceptibility (right).

2.1.2 Paramagnetic materials

Contrary to the diamagnetic ones, paramagnetic (PM) materials have unpaired electrons and, thus, present a net atomic magnetic moment. However, in PM materials, atomic magnetic moments have only weak exchange interaction with their neighbours and the thermal energy causes their random alignment. Therefore, the material has no net magnetic moment until a magnetic field is applied. Indeed, as the field is turned on, the atomic moments start to align resulting in a macroscopic magnetization of the material. For small applied field only a fraction of atomic moments is deflected along the field direction, which increases linearly with the applied field. A further increase in the applied field results in a deviation from the linear behaviour; the M vs field curve then is described by the Langevin function until the saturation value, at which all atomic moments are aligned, is reached. Moreover, the alignment degree decreases as temperature increases because of the

disordering effect of the thermal energy. Therefore, the susceptibility has a positive value, which is inversely proportional to the temperature as expressed by the well-known *Curie law*:

$$\chi = \frac{C}{T} \qquad 2.5$$

Where C is the *Curie constant* and it is typical of the considered material.

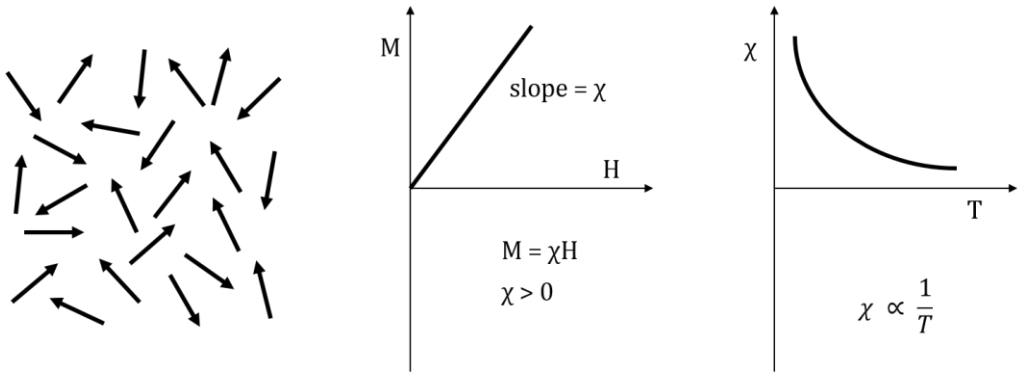

Figure 2.3: From the left: relative spin orientation when no magnetic field is applied, field dependence of the magnetization and temperature dependence of the magnetic susceptibility in paramagnetic materials.

2.1.3 Ordered magnetic materials

Like paramagnets, ferromagnetic (FM), ferrimagnetic (FiM) and antiferromagnetic (AFM) materials have unpaired electrons. However, such materials present a strong *exchange interaction* (H_{ex}) between atomic moments. Therefore, they are characterize by an ordered network of magnetic moments at room temperature, which could be aligned parallel or antiparallel as described in Equation 2.4. In particular, a positive value of J_{ex}, i.e. parallel-aligned spin moments, leads to FM materials; while negative values to FiM or AFM ones.

Since FM materials have the all the atomic moments parallel one to each other, they are characterized by the presence of a net magnetic moment even without an applied field. This spontaneous magnetization is maximum at 0 K, (M_0), where all the atomic moments are perfectly parallel aligned. As the temperature increases, the thermal energy introduces some disorder in the alignment, which makes the magnetization to decrease, until a critical temperature, called *Curie temperature* (T_C), is reached, where the thermal energy overcomes the exchange interaction and the material assumes a PM behaviour. Therefore, T_C depends on the strength of the exchange interaction between the atomic magnetic moments and it is typical of each considered material. Accordingly, in FM materials the temperature dependence of susceptibility can be expressed by the *Curie-Weiss law*:

$$\chi = \frac{C}{T - \theta} \qquad 2.6$$

where θ is the temperature at which the susceptibility becomes infinite and it is equal to T_C of the FM material.

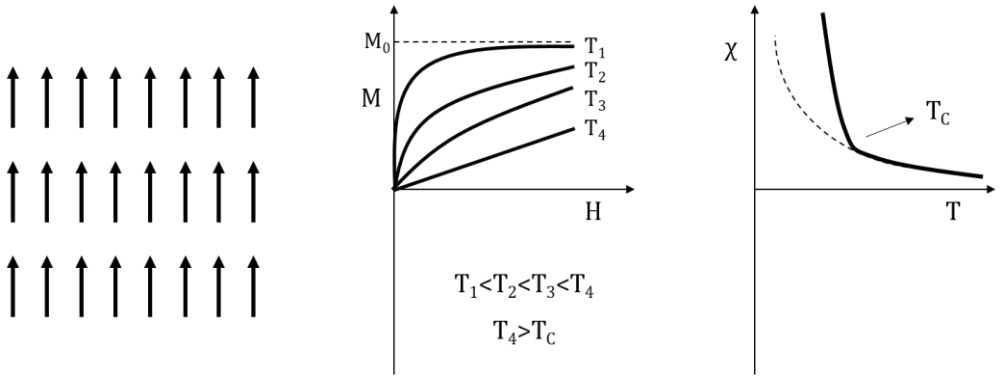

Figure 2.4: From the left: relative spin orientation when no magnetic field is applied (at T = 0 K); field dependence of first magnetization at different temperatures; temperature dependence of magnetic susceptibility of ferromagnetic substances.

On the contrary, FiM and AFM materials present negative values of J_{ex} leading to an antiparallel alignment of neighbouring atomic magnetic moments. Such materials can be schematized through the combination of two antiparallel aligned magnetic sub-lattices, inside of which magnetic moments are parallel-aligned. While in AFM materials the magnetic sub-lattices compensate each other nullifying the total magnetization, in FiM systems they have different values resulting in a net magnetization. Therefore, FiM materials can be imaged as FM ones where the net magnetization corresponds to the difference between the values of the two sub-lattices. Consequently, FiM materials can be treated as FM ones and their behaviour can be described by the *Curie-Weiss law* (Equation 2.6) presenting a characteristic ordering temperature (T_C) above which the material becomes PM.

Similarly, AFM materials are characterized by an ordering temperature, called. *Néel temperature* (T_N), above which they start to behave like PM phases. Indeed, above T_N, AFM materials follow the *Curie-Weiss law* (see Equation 2.6), where θ has negative value. However, unlike FM materials θ does not coincide with T because of the effects of superexchange interactions (i.e., next-nearest-neighbour interactions).

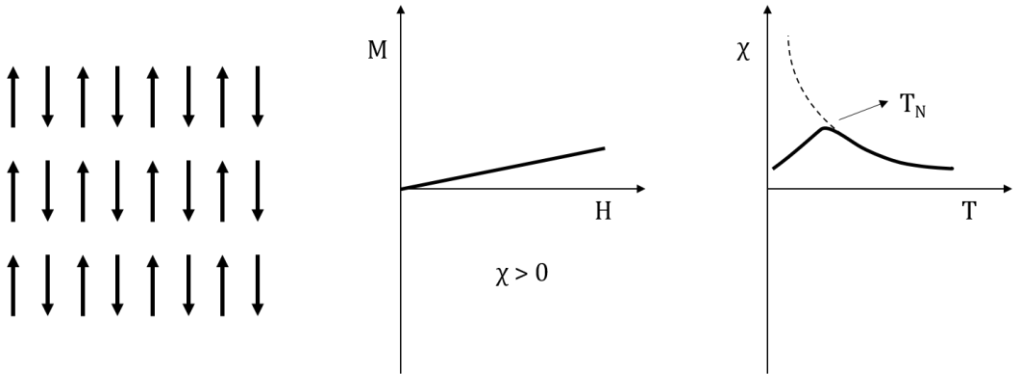

Figure 2.5: From the left: relative spin orientation when no magnetic field is applied (at T = 0 K), field dependence of magnetization and temperature dependence of magnetic susceptibility in antiferromagnetic materials.

2.1.4 Magnetic domains and hysteresis

As described above, the exchange interaction tends to align atomic magnetic moments. In particular, in order to be minimized the exchange anisotropy requires the entire magnetic material has completely aligned moments. However, in ordered magnetic systems there are other contributions to the total energy that must be considered to understand the final configuration of the material: the *magnetocrystalline energy*, originated from spin-orbit coupling forcing a specific magnetic moment orientation and the *magnetostatic energy*, arising from the presence of a net magnetic moment originating a magnetic field. [1,2]

More in detail, in FM, or FiM, crystals, as a consequence of the spin-orbit coupling, the magnetization tends to preferably align along certain crystallographic directions. Because along these directions it is easier to magnetize a sample to saturation, i.e., the saturation value is reached at a lower field, they are called *easy axes*. On the contrary, there exist directions along which is more difficult to magnetize the sample, which are called *hard axes*. Therefore, the alignment along the preferred crystallographic directions corresponds to a minimum of the magnetocrystalline anisotropy energy, defined as the difference in energy between magnetizing a sample along the easy and hard axes, and any deviation from the preferred crystallographyc directions results in an increase in the energy of the system.

In addition, because of the order of magnetic moments, FM or FiM materials have a macroscopic magnetization, which originates a magnetic field both around and inside the material. This field, known as *demagnetizing field* ($\boldsymbol{H_d}$), is oriented in such a way that it magnetizes the material in the opposite direction with respect to its own magnetization. Thus, $\boldsymbol{H_d}$ causes a magnetostatic energy that is proportional to the field and depends on the shape of the material. This energy can be minimized by dividing the material into domains (see Figure 2.6).

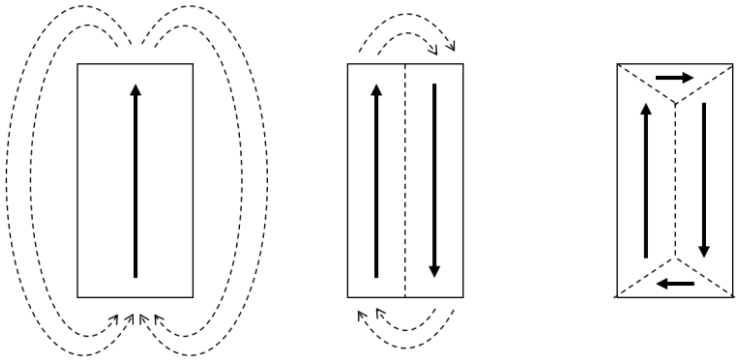

Figure 2.6: Reduction of the demagnetizing field, and hence of the magnetostatic energy, by domains formation.

However, it has to be taken into account that the presence of domains results in the formation of *domain walls*, i.e. the interface between adjacent domains, gives rise to an other energy contribution, which is proportional to the domains area. The schematic presentation of a 180° domain wall in a FM material, reported in Figure 2.7, illustrates this contribution: the magnetic moments within the wall are not parallel one to,each other, hence the exchange energy is higher inside the domain wall than in the domain. In addition, the dipole moments of the atoms within the wall are not pointing in the easy direction of magnetization (they are not at 180° one to each other), thus they have also higher magnetocrystalline energy.

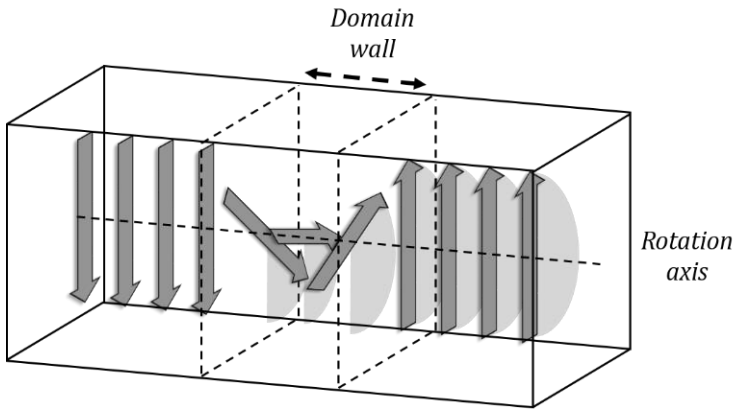

Figure 2.7: Schematic representation of a 180° domain wall.

The energy contribution per units of area, called *domain wall energy*, E_w depends on the material magnetocrystalline anisotropy and strength of the exchange interaction between neighbouring atoms:

$$E_w = 2\sqrt{KA} \qquad 2.7$$

where K is the anisotropy energy constant and A is the exchange energy density.

The thickness of the walls (δ) will also vary in relation to these parameters as described by the following equation:

$$\delta = \pi \sqrt{\frac{A}{K}} \qquad 2.8$$

Therefore, a strong magnetocrystalline anisotropy favours narrow walls, whereas a strong exchange interaction will favour wider walls.

Accordingly, a global minimum energy of the system can be achieved by the balance between exchange, magnetostatic and magnetocrystalline energies, resulting in a specific number, size and shape of domains that will depend on the composition, crystallographic structure, size and shape of the material. The presence of domains strongly affects the magnetic behaviour of FM, or FiM, materials. In fact, in the absence of an applied fields, the domains are arranged so as to reduce the magnetostatic energy and therefore the material net magnetization (see Figure 2.6). When an external field is applied, the domain whose magnetization is parallel to the field direction starts to grow decreasing the other domains. The domains growth occurs through wall motion, as showed in Figure 2.8.

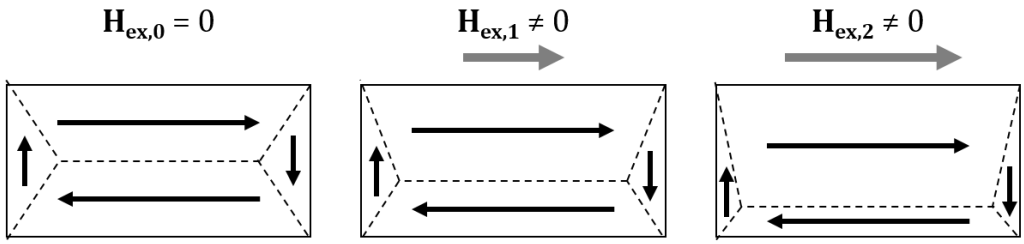

Figure 2.8: Schematic representation of the domain wall motion as an external field is applied ($H_{ex,1} < H_{ex,2}$).

Eventually, if the applied field is large enough to eliminate all domain walls, a single domain with its magnetization aligned along the easy axes oriented most closely to the applied field will remain. A further increase in magnetization can only occur by rotating the magnetic moments from the easy axis into the direction of the applied field. Once all magnetic moments are aligned with the applied field, the maximum value of magnetization is reached. This value is called *saturation magnetization* (M_S). The field at which M_S is reached is larger the higher the magnetocrystalline anisotropy of the material is. Then, once removed the applied field, the magnetic moments rotate back to their easy axis of magnetization. In addition, magnetostatic energy pushes the domain wall motion back to their initial configuration. However, the domain walls movement should pass through imperfections of the material such as defects or crystal dislocations. Such imperfections have associated an energy contribution because exchange-interaction are not minimized, i.e., parallel/antiparallel alignment is not fulfilled, and that are eliminated as the walls move across them; thus, it is necessary to provide some energy to a domain wall to move it across

these imperfections. Accordingly, when the applied field is removed, the material cannot return to the initial domain configuration but maintains a net magnetization know as *remanent magnetization* (M_R). On the contrary, in order to demagnetize the material ($M=0$) it is necessary to apply an external field in the opposite direction with respect to the magnetizing one; this field takes the name of *coercive field* (H_C).

Therefore, FM and FiM materials present a hysteretic response of the magnetization to an applied field as shown in Figure 2.9.

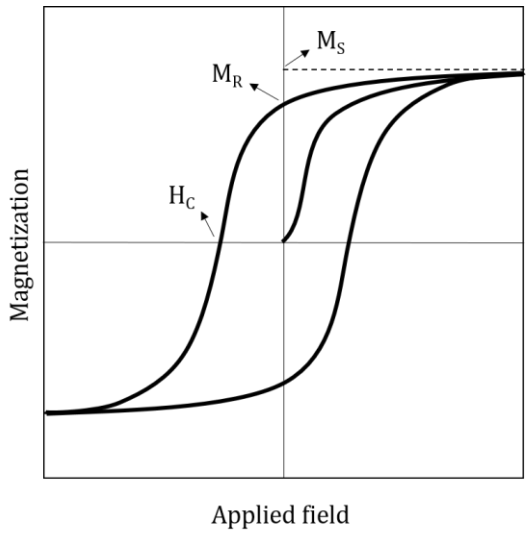

Figure 2.9: Hysteresis loop of a magnetic material.

The shape of the hysteresis loop depends on the nature of the material, its size, its crystallinity and purity. In particular, it is possible to distinguish between two main classes of magnetic materials according to the different behaviour:

(I) *Hard* magnetic materials, which are characterized by high H_C values (few tens Oe).
(II) *Soft* magnetic materials, which are characterized by low H_C values (hundreds Oe).

2.2 Magnetic properties of nanoparticles

As previously reported, matter behaves differently when its size is reduced to the nanoscale. In general, structure-sensitive properties are affected by *finite-size effects* once the size of the material is comparable to their characteristic length scale. In particular, the domain walls thickness, which falls in the nanometric range, is one of the characteristic lengths affecting material magnetic behaviour. Moreover, also the increase in the ratio between surface and volume, typical of the nanostructures, produces further effects, such as surface

anisotropy, atomic disorder, spin frustration and core-surface extra exchange anisotropy. [3–5]

2.2.1 Single magnetic domain nanoparticles

As described above, the formation of magnetic domains in bulk materials occurs in order to reduce the magnetostatic energy of the system. However, when the size of the material becomes smaller than the domain walls thickness, the energy gain obtained by the formation of a multi domain structure is lower than the energy spent for the wall formation, leading to a single domain system. In particular, for a spherical particle the critical diameter (d_{sd}), below which it consists of a single domain, is given by the following equation. [6–8]

$$d_{sd} = \frac{18E_w}{\mu_0 M_S^2} \qquad 2.9$$

In most common magnetic material d_{sd} is in the range of 20-800 nm, depending on its magnetization, anisotropy and exchange energy. [6] The main consequence of being in the single domain region is that changes in the material magnetization cannot longer occur through domain wall motion but require the rotation of all the spins, resulting in an enhancement in the coercivity of the system. [9] Indeed, spin rotation is opposed by the magnetocrystalline and exchange anisotropy forces, which are usually much greater than the local forces opposing movement of a domain wall.

2.2.2 Single magnetic domain nanoparticles

The Stoner and Wohlfarth model [10] describes the energy related to the magnetization reversal in terms of the material anisotropy. The model assumes a coherent rotation of all the spin in a particles and the presence of a uniaxial anisotropy (the system is characterized by a single easy axis of magnetization) thus the energy density of the system can be written as:

$$E_B = KVsin^2(\theta) + HM_S cos(\phi - \theta) \qquad 2.10$$

where θ is the angle between M and the magnetization easy axis, and ϕ the angle between H and the magnetization easy axis (see Figure 2.10). In particular, the first term ($KVsin^2(\theta)$) refers to the magnetic anisotropy and the second one ($HMcos(\phi-\theta)$) is the Zeeman energy corresponding to the torque energy on the particle moment by the external field.

As illustrated in Figure 2.10, when $H=0$ the Zeeman term is zero and there exist two equilibrium states for $\theta=0$ and $\theta=\pi$. The energy barrier separating these two states is equal to KV. This is the magnetic anisotropy energy of the system, [11] and corresponds to the energy for the magnetization reversal to occur.

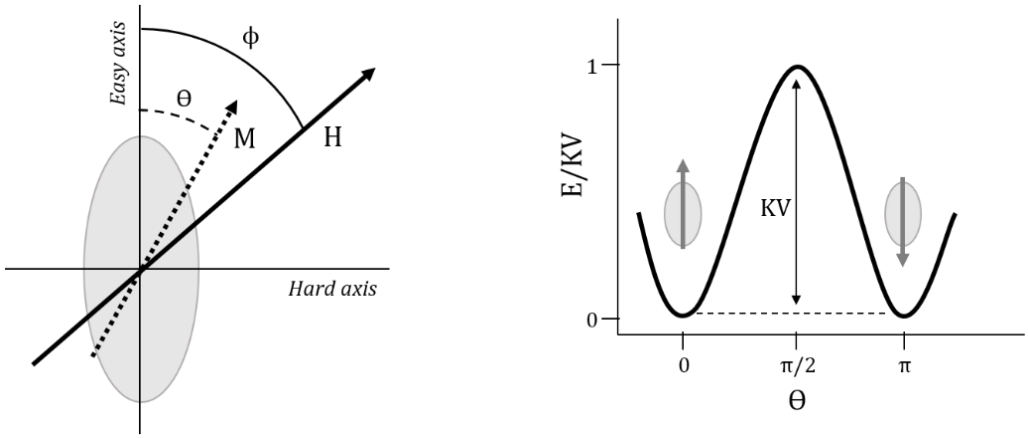

Figure 2.10: Stoner and Wohlfarth model: definition of the axis system (*left*) and angular dependence of the energy for a zero external field (*right*).

On the other hand, for a fixed temperature, the presence of an applied field will modify the particle energy through the Zeeman term. If $H < 2K/M_S$ the system energy maintains two minima although they are no more equivalent in energy; in particular the lowest level will be the one closest to the applied field direction. On the contrary, if $H \geq 2K/M_S$ only a single minimum will be present. The H value at which the energy of the system starts to present only one minimum ($H_0 = 2K/M_S$) is called *anisotropy field*.

2.2.3 Superparamagnetism

Since the energy barrier of a single domain particle with uniaxial anisotropy is KV, as the volume decreases, it becomes increasingly smaller. Eventually, for particle of few nanometers, the term KV becomes sufficiently small, that, even in the absence of an external field, the thermal energy (k_BT, where k_B is the Boltzman's constant) is sufficient to induce magnetic fluctuations and spontaneous reverse of the magnetization from one easy direction to the other. In these conditions the system acts like a paramagnet (see section 1.1.2), however the magnetic moment value is much higher, because it corresponds to the sum of 10^2-10^5 spins. For this reason, this state is called superparamagnetic state. [9,11,12]The temperature at which the system reaches the superparamagnetic state depends on particles volume and anisotropy. In order to maintain the exchange energy unchanged, in the superparamagnetic state the thermal fluctuations reverse all the atomic magnetic moment of the particles at the same time keeping them parallel (or antiparallel), i.e. the magnetization reversal occurs through *coherent rotation* of all the atomic magnetic moment moments.

In addition, for a given temperature, it is possible to introduce a *relaxation time* (τ) for the magnetization reversal.

$$\tau = \tau_0 \exp\left(\frac{KV}{k_B T}\right) \qquad 2.11$$

where τ_0 is a time constant characteristic of the material and usually is of the order of 10^{-9}-10^{-12} s for non interacting ferro/ferrimagnetic particles. The magnetic behaviour of single domain particles is then strongly time dependent, i.e. the observed magnetic state of the system depends on the characteristic measuring time of the used experimental technique, τ_m. Therefore, it can be defined a temperature, called *blocking temperature* (T_B), at which the relaxation time equals the measuring one ($\tau = \tau_m$):.

$$T_B = \frac{KV}{k_B ln\left(\frac{\tau_m}{\tau_0}\right)} \qquad 2.12$$

Consequently, being T_B dependent on the time scale of the measurements, for experimental techniques with $\tau_m > \tau$ the system reaches the thermodynamic equilibrium in the experimental time window and a superparamagnetic behaviour is observed. On the contrary, when $\tau_m < \tau$ quasi-static properties (similar to bulk materials) are obtained, i.e. the particles are in the *blocked regime*. Therefore, a nanoparticle's assembly at a given temperature can be both in superparamagnetic and blocked regime depending on the measuring technique. In particular, for typical ZFC-FC measurement as those often used in this work, τ_m = 100 s and, assuming τ_0=10^9, Equation 2.12 becomes:

$$T_B = \frac{KV}{25 k_B} \qquad 2.13$$

It has to be reminded that, these relations are obtained for monodisperse, non-interacting, single domain nanoparticles. In fact, being T_B proportional to the volume of the particles, the presence of a size distribution implies also a distribution of T_B values. Besides, inter-particle interactions, which will be discussed later, can increase T_B due to extra energy terms introduced by the dipolar and/or exchange interactions.

2.2.4 Surface effects

In the previous paragraphs, it has been reported how *finite-size effects* affect the magnetic properties of nanoparticles; however, the reduction of particles size to the nanoscale leads to further modification in the material magnetic behaviour due to the increased ratio between surface and volume. In fact, in few nanometers particles, the number of atoms on the surface is no longer negligible with respect to the inner atoms and *surface effects* become relevant. Surface atoms suffer by the break in the coordination sphere resulting in a lack of symmetry, which often reflects in surface spin disorder, [3,11] e.g. canted spin, frustration and spin-glass behaviour. In particular, *spin canting* arises from the fact that the change in the surface atom coordination may lead to a change in the lattice constant of the material. In

this situation, a local change in the direction of the magnetization easy axis can occur, canting the superficial spin with respect to the inner ones. [13,14] Magnetic *frustration* arises from the reduced numbers of magnetic neighbours at the particle surface or around defects in the interior. [15–17] In addition spin canting and frustration could result in a deficiency of long-range magnetic ordering and leading to the so-called *spin-glass-like* behaviour. [18,19]

As a result, the ideal model where all the spins undergo to the coherent reversal of the magnetization is no longer valid. It is possible to consider the system to be composed of two phases: a crystalline core governed by the magnetic bulk properties, and a disordered surface layer. [3,11,20] Therefore, the *effective anisotropy*, K_{eff}, for a core|surface spherical nanoparticle with diameter d can be defined as:

$$K_{eff} = K + \frac{6}{d} K_S \qquad 2.14$$

where K is the anisotropy constant of the ordered core region and K_S is the surface anisotropy constant, taking into account the contribution of the disordered surface layer. Thus surface anisotropy increases the overall particle anisotropy and enhances the coercive field. Given the increasing role of the surface anisotropy contribution as the size decreases, the increase in H_C is strongly related with the reduction of the particle size. [21] Moreover, the presence of the surface disorder has reported to affect also the saturation magnetization of the material, resulting both in a M_S reduction or enhancement. Indeed, while canted spins lead to a decrease in spins orientation with field and thus to a decreased M_S, [22,23] frustration can cause an uncompensation between antiparallel sub-lattices producing a larger M_S. [24–26] In addition, the instauration of a spin-glass-like behaviour has been reported to cause large irreversibility field in the hysteresis loops (i.e., the loops do not close up to high fields) and lack of saturation even for extremely large fields. [13,14] In addition, the spin-glass state can create an exchange field interaction between core and surface regions, which is responsible for the experimentally observed loop shifts in the field axis after a field cooling, i.e. *exchange bias* (H_E, see below). [19]

Interestingly, also AFM nanoparticles present novel properties which are drastically different from the bulk properties due to surface and finite-size effects,. Particularly, below T_N the presence of the surface magnetism can lead to FM-like properties, with finite M_S and large H_C. Other effects such as changes in T_N can also take place. [27–29] On the other hand, an exchange coupling between the spin-glass surface and the AFM core can occur producing an enhanced H_C and the presence of H_E. [23,24]

2.3 Interaction effects in nanostructures

As reported above, FM or FiM nanoparticles in the *blocked state* are characterized by the presence of a net magnetic moment even in absence of an external applied field. Therefore, blocked nanoparticles produce a magnetic field, which can interact with the magnetic moment of neighbouring nanoparticles. Such interaction, known as *dipole-dipole interaction*, is a long-range anisotropic interaction which strength depends on the distance between the nanoparticles and on the degree of mutual alignment. In particular, dipole-dipole interactions modify the energy barrier of each particle (that arising from the anisotropy contribution, KV), which in the limit of weak interactions becomes:

$$E_a = V(K + H_{int}M) \qquad 2.15$$

where H_{int} represents the *mean interaction field*. [30] On the other hand, as interaction strength increases, the evolution of the system occurs through a complex series of energy minima, changing as nanoparticles reverse their magnetization. Extensive experimental and theoretical works agree that the interaction among magnetic particles plays a fundamental role in the magnetic behaviour of granular systems. [31–36] Despite of this, there exist several inconsistencies. For example several theoretical models predict the increase of the T_B with strength of the dipolar interactions, i.e. increasing particle concentration or decreasing particle distance. [30,33,36] On the other hand, in the weak interaction limit some theoretical models propose the opposite dependence of T_B with the dipole-dipole interaction strength. Both different behaviours have been experimentally reported. [32–34,36] Dipole-dipole interactions can also affect the shape of the hysteresis loop in magnetic nanoparticles. In fact, when the particles are randomly oriented, the reduction of the inter-particle distance can cause a decrease in the energy barrier of the system and thus to its coercivity. This behaviour has been both theoretically predicted [37,38] and experimentally demonstrated. [39] In contrast, when the particles are not randomly oriented the coercivity can increase or decrease depending on the type of arrangement. [40,41]

If nanoparticles are in close proximity, *exchange interactions* between surface atoms can also be operative because of the overlap of their wave functions resulting in a modification of the energy barrier of the system. Therefore, since this interaction is related to surface atoms, it is appreciable only in nanostructured materials, i.e. when the surface-to-volume ratio is large. As a matter of fact, exchange interaction is an interfacial effect, which takes place by the direct contact between subsequent layers. Two main exchange effects can appear:

(I) *Exchange-spring* arising from the interface contact between two FM, or FiM, phases.
(II) *Exchange bias* originated usually from interface contact between an AFM phase and a FM, or FiM, one. However, it can occur in other type of bi-magnetic systems (FM-FM, FiM-FiM) or spin-glass materials.

However, in most of the single-phase magnetic nanoparticles synthesized via wet chemistry, exchange inter-particle effects are avoided due to organic molecules covering the particles. Conversely, these effects appear in hybrid nanostructure, e.g. core|shell nanoparticles or heterodimers, where the different magnetic phases are in direct contact.

2.3.1 Exchange-spring magnets

Historically, studies on exchange-spring magnets are strictly related to attempt of enhancing permanent magnet performances producing an increase in the area of the hysteresis loops. In fact, Kneller and Hawig [42] proposed a new concept to develop permanent magnets based on exchange-coupled magnetic nanocomposites where a hard-FM phase, characterized by high magnetocrystalline anisotropy (large H_C), and a soft phase with high magnetic moment (large M_S) are coupled through exchange interactions, producing a so-called exchange-spring permanent magnet. The behaviour of these systems can be primarily understood from the intrinsic parameters of the hard and soft phases, as the resultant hysteresis loop should maintain a high H_C close to that of the hard phase and a large M_S close to the soft phase one. [43]

More in detail, the exchange coupling results in the following modifications of the magnetic properties (see Figure 2.11):

(I) *Remanence ($R=M_R/M_S$) enhancement*. In accordance with Stoner-Wohlfarth prediction, [10] in a non-interacting ensemble of single-domain grains with uniaxial magnetocrystalline anisotropy and isotropic distribution of easy axes, $M_R = 0.5M_S$. However, if neighbouring grains are coupled through exchange interaction, interfacial magnetic moments of the soft grains are aligned parallel to the magnetic moments of the hard ones resulting in $M_R > 0.5M_S$.

(II) *Coercive field variation*. Due to exchange interaction, interfacial atoms of the soft phases are characterized by a larger coercivity, which tends to that of the hard one. At the same time, exchange interaction between grains leads to a reduced coercivity of the hard phase. Indeed, when the demagnetizing field reverses the moments in some grains, they tend to reverse the moments in the neighbouring ones by exchange coupling. As a result, the final coercive field of the system assumes an intermediate value between those of the two magnetic phases.

(III) *Demagnetizing curve modification*. If all the soft phase is exchange-coupled with the hard one, both phases reverse their magnetization at the same nucleation field (H_N) and the demagnetizing curve in the second quadrant is convex like for a single-phase material. Conversely, if the interfacial atoms are only a fraction of the entire soft phase, the magnetization reversal of the uncoupled fraction of soft phase occurs at significantly lower fields than the H_N of the system. Hence, the demagnetizing curve in the second quadrant has a concave shape.

(IV) *Spring-magnet behaviour*. In the demagnetizing process, the reversal of magnetic moments is reversible when the applied field is smaller than H_N, i.e. before the hard phase starts to reverse its magnetization. However, for $H < H_N$ the moments of the soft phase can already have reversed their magnetization and, as the field is removed, they return reversibly to their original direction due to the coupling with the hard phase. Thus, because of the large contribution of the soft phase to the final M value, the reversible magnetization of the hard-soft two-phase magnets is much larger than that of conventional hard magnets. Therefore, the magnetic behaviour recalls the one of a mechanical spring, whence the name spring-magnet.

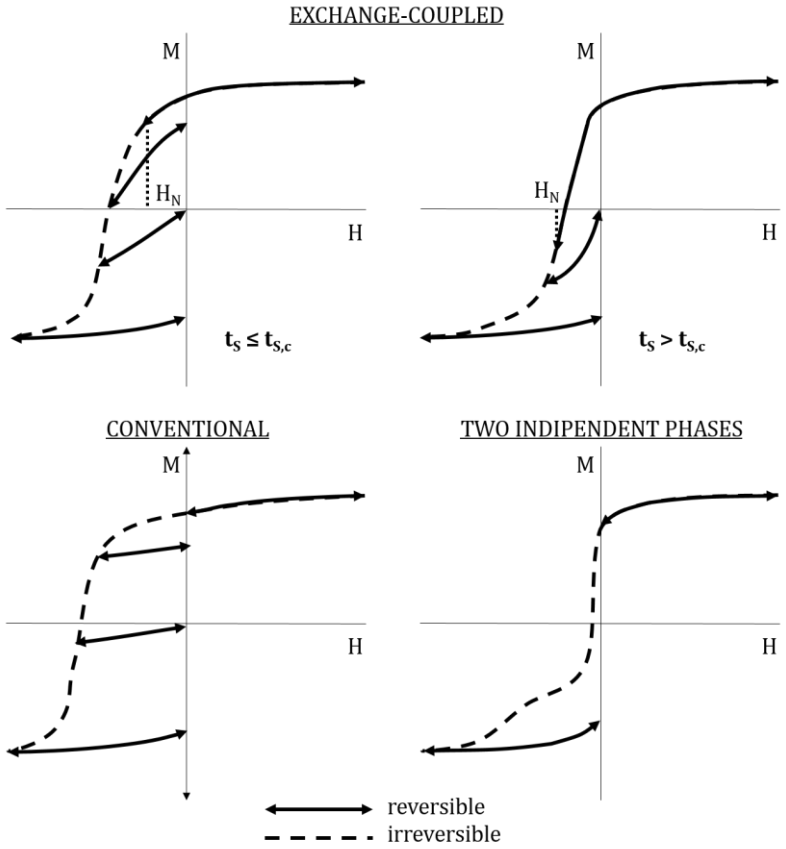

Figure 2.11: Scheme of typical demagnetization curves *M(H)* in bi-magnetic systems. Top: exchange-spring magnet with $t_S \leq t_{S,c}$ (left) and $t_S > t_{S,c}$ (right) Bottom: conventional single ferromagnetic phase magnet (left) and mixture of two independent ferromagnetic phases with largely different hardness (right). [42]

All these modifications in the magnetic behaviour are strictly affected by the fraction of exchange-coupled soft phase and, since exchange-coupling occurs at the interface, by its thickness (t_S). In particular, there exists a critical thickness of the soft phase ($t_{S,c}$), below

which the system is completely exchange-coupled, corresponding roughly to twice the width of a domain wall in the hard phase (δ_H).

$$t_{S,c} = 2\delta_H = 2\left(\pi\sqrt{\frac{A_H}{K_H}}\right) \qquad 2.16$$

where A_H and K_H are the exchange and anisotropy constants of the hard phase, respectively. Therefore, the two different behaviours described in point (III) can occur when $t_S \leq t_{S,c}$ and $t_S > t_{S,c}$. In particular, when $t_S \leq t_{S,c}$ the system behaves as a single phase with averaged magnetic properties of the two phases and its nucleation field, which controls the reversibility of the demagnetizing process, is given by the following equation:

$$H_N = \frac{2(t_H K_H + t_S K_S)}{t_H M_H + t_S M_S} \qquad 2.17$$

where $K_{H/S}$ and $M_{H/S}$ are the anisotropy constants and the magnetization of the hard/soft phases, respectively. On the other hand, when $t_S > t_{S,c}$ the magnetization reversal of the soft phase occurs at fields well below the nucleation field. Indeed, the soft phase remains parallel to the hard one until the applied field reaches the exchange field (H_{ex}) given by:

$$H_{ex} = \frac{\pi^2 A_S}{2M_S t_S^2} \qquad 2.18$$

Then, once the applied field exceeds H_{ex}, magnetic reversal proceeds via a twist of the uncoupled soft phase magnetization while the coupled fraction remains strongly pinned at the interface as shown in Figure 2.12. The spins in the uncoupled soft phase exhibit continuous rotation, as in a magnetic domain wall, with the angle of rotation increasing with increasing the distance from the interface. However, due to exchange coupling interaction with neighbouring spins, once the external field is removed the magnetization rotates back along the hard phase direction.

In has to be pointed out that the partial reversibility of the demagnetizing process occurs both in the totally and partially exchange-coupled systems (i.e., $t_S \leq t_{S,c}$ and $t_S > t_{S,c}$, respectively). However, in the latter case the phenomenon is more prominent and, being $M_S > M_H$, it can occur also when the net magnetization of the material has opposite direction to the hard phase. Therefore, spring-like behaviour, and thus the spring-magnet definition, is commonly associated to materials which present inhomogeneous magnetization reversal.

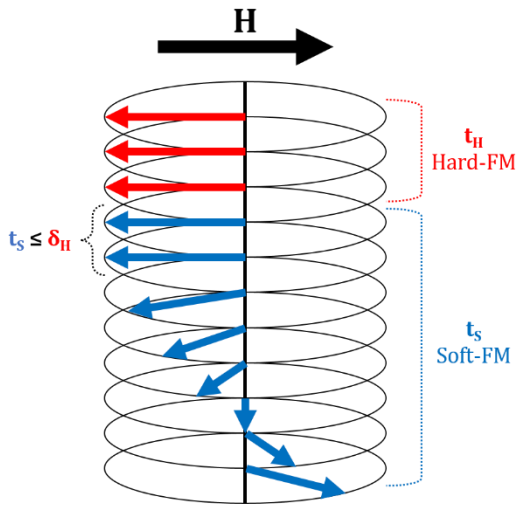

Figure 2.12: Schematic diagram of soft magnetic phase switching in a unidimensional exchange-spring magnet.

2.3.2 Exchange bias

Exchange bias, firstly reported by Meiklejohn and Bean in 1956, [44] arises from exchange-coupling interactions between AFM and FM, or FiM, materials. In particular, exchange bias manifests as a horizontal hysteresis loop shift and an enhancement of the coercivity, as the system is cooled through the T_N of the AFM (with T_C of the FM, or FiM, larger than T_N) in the presence of an applied field. [45] In addition, exchange bias has also been observed in other type of bi-magnetic systems, e.g. FM-FM, FiM-FiM or spin-glass materials, where, due to its random character, spin-glasses can play the role of both the AFM and FM phases. [46]

As for exchange-coupling effects occurring in spring-magnets, exchange-bias is appreciable only in nanostructured materials since it is a surface related effect. More in detail, assuming a nanostructured AFM-FM system with $T_C > T_N$, when a static external field is applied and the system is cooled down from a temperature below T_C ($T_C > T > T_N$) to a temperature below T_N ($T < T_N$), the hysteresis loop shifts horizontally, i.e. moves its centre from $H = 0$ to $H_E \neq 0$ in the opposite direction of the cooling field. Moreover, the material shows an increased coercivity, i.e. a widening of the hysteresis loop. Both these effects, reported separately in Figure 2.13, disappear as the measuring temperature approaches to the AFM T_N, confirming the role of the AFM-ordered structure in inducing the observed features.

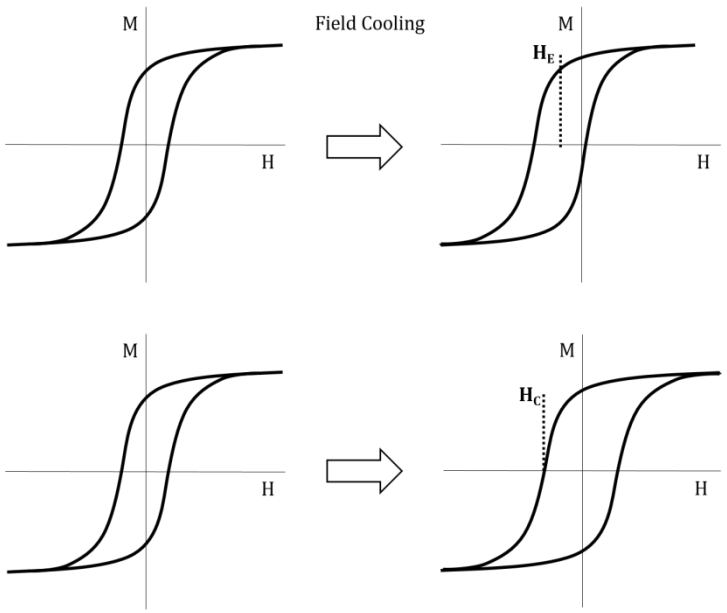

Figure 2.13: Schematic representation of the two main effects induced by the AFM-FM exchange coupling, the loop shift (top) and coercivity enhancement (bottom). [46]

This unusal magnetic behaviour can be explained in term of a new type of induced *unidirectional anisotropy* (K_{ua}), presenting a $K_{ua}cos(\theta)$ angular dependence, different from the $K_u sin^2(\theta)$ of the common uniaxial anisotropy (see Equation 2.10). As can be seen in Figure 2.14 the energy of a system with uniaxial anisotropy presents two minima at 0° and 180°, while the exchange bias induced anisotropy produces a unique minimum at 0°. Therefore, the two opposite direction along the easy axis of an uniaxial anisotropy system do not longer have the same energy, which is now minimized only in the $\theta = 0$ direction.

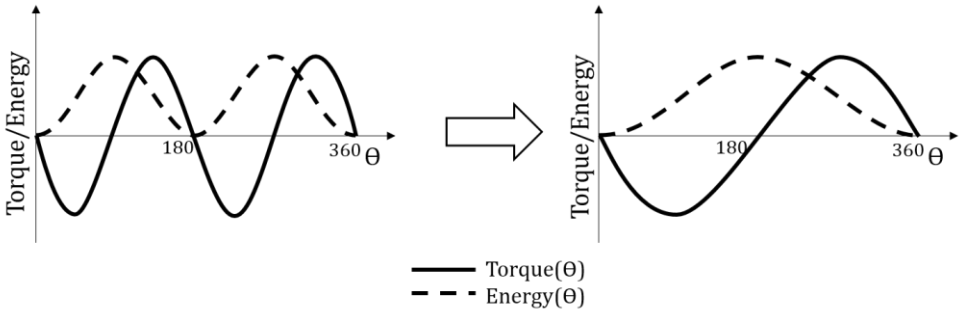

Figure 2.14: Change from uniaxial (left) to unidirectional anisotropy (right); solid lines represent torque measurements ($sin(\theta)$) and dashed ones the global magnetic energy ($sin^2(\theta)$). [46]

Even if the cause of exchange bias in nanoparticles is still not completely understood, usually the observed unidirectional anisotropy and the loop shift are explained in terms of parallel alignment of the interfacial FM and AFM uncompensated spins occurring during the

field cooling process. [45,46] This coupling entails an extra energy barrier for FM spin to reverse leading the system to behave as show in Figure 2.15.

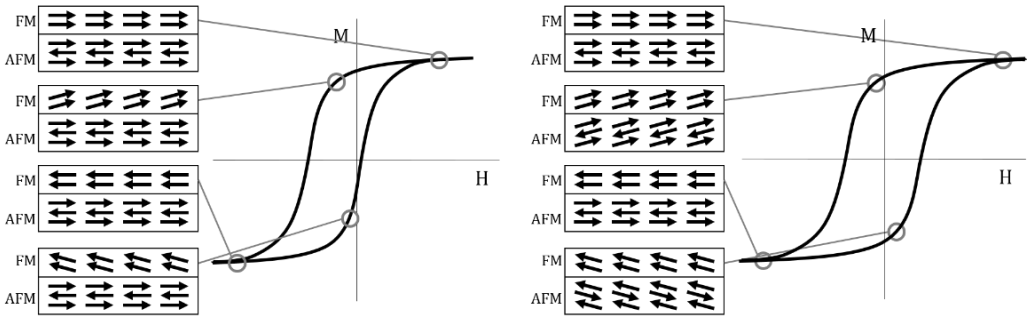

Figure 2.15: Schematic diagram of magnetic behaviour during a hysteresis loops for a AFM-FM spins system with large K_{AFM} (left) and with small K_{AFM} (right). [46]

More in detail, above T_N of the AFM, the spins of both phases are aligned in the same direction of the external field (***H***), but as the temperature decreases below T_N the spins of the AFM align antiparallel to each other with the interfacial layer parallel to the FM and thus to ***H***. Then, during the demagnetizing process two different situations can occur depending on the anisotropy constant of the two phases: if $K_{AFM} \gg K_{FM}$, when the FM starts reversing its magnetization, the exchange-coupling interaction with the AFM, whose spins remain pinned in the original direction, increases the coercive value at negative fields. Conversely, during the magnetization process from negative saturation, exchange-coupling interaction with AFM promotes the magnetization reversal in the direction of the cooling field decreasing the coercive value at positive field. As a result, the hysteresis loop shifts to the left in the field axis and is now centered in $-H_E$ instead that on the origin. On the other hand, if $K_{AFM} \leq K_{FM}$, the two phases reverse their magnetization together. Then, the energy needed to switch FM spins becomes larger in both branches of the hysteresis loop, since the FM has to drag AFM spins. Therefore, the final loop shows an enhancement of both coercive fields..

Assuming the magnetization to rotate coherently and that the FM and AFM easy axes are parallel, the energy per unit surface in the AFM-FM exchange coupled system can be expressed as:

$$\frac{E}{S} = -\ HM_{FM}t_{FM}cos(\theta-\beta) + \ K_{FM}t_{FM}sin^2(\beta) + \ K_{AFM}t_{AFM}cos^2(\alpha) - \ J_{INT}cos(\beta-\alpha) \qquad 2.19$$

where H is the applied magnetic field, M_{FM} is the saturation magnetization in the FM, t_{FM} and t_{AFM} are the thicknesses of the FM and AFM layers, respectively, K_{FM} and K_{AFM} are the magnetic anisotropies and J_{INT} is the exchange coupling constant at the interface. The angles α, β and θ are the angles between the spins in the AFM and the AFM easy axis, the direction

of the spins in the FM and the FM easy axis and the direction of H and the FM easy axis, respectively. As can be seen from the different energy terms, if no coupling exists between the two phases and H is turned off, the overall energy of the AFM-FM system reduces to the terms due to the FM and the AFM magnetic anisotropies (2nd and 3rd terms). When a magnetic field is applied, a work has to be carried out to rotate the spins in the FM (1st term). Finally, the 4th term represents the AFM-FM coupling.

Assuming that the AFM has a very large anisotropy and that its spins remain pinned along their direction and do not rotate with the field ($\alpha = 0$), we obtain that the horizontal shift for the hysteresis loop is given by

$$H_E = \frac{J_{INT}}{M_{FM} t_{FM}} \qquad 2.20$$

Conversely, for low values of the AFM anisotropy the rotation of both the FM and AFM spins is more energetically favourable and no horizontal shift is induced. However, since the overall anisotropy of the system is changed, an increase of the coercivity is induced. [44,47]

In has to be pointed out that, Equation 2.20 slightly overestimates H_E value because of the assumptions of having homogeneous layers in the x-y plane, sharp interface, coherent magnetization reversal and parallel uncompensated spins of both phases. Therefore, more complex approaches have been developed accounting lateral magnetic structure of the layers, different spin configuration, interface roughness and domain walls formation. [45,46,48] Nevertheless, even if it provides a simplified view of the system, Equation 2.20 indicates that H_E is inversely proportional to the FM thickness. This aspect can have a dramatic effect in nanostructured system as nanoparticles, since the FM thicknesses involved are rather small and, thus, large loop shift would be expected. Besides, H_C dependence with t_{FM} follows a similar trend increasing as t_{FM} decreases.

On the other hand, the dependence of H_E on the AFM thickness is more complicated (t_{AFM}). The general trend is that for thick AFM layers, e.g. over 20 nm, H_E is independent of the thickness of the AFM layer. As the AFM thickness is reduced, H_E decreases abruptly and finally, for thin enough AFM layers (usually few nm), when $K_{AFM} t_{AFM} < J_{INT}$, H_E becomes zero. Therefore, it is possible to define the critical AFM thickness, above which H_E disappears and H_C drops to the value of the uncoupled FM, with the following equation: [46]

$$t_{AFM}^{crit.} = \frac{J_{INT}}{K_{AFM}} \qquad 2.21$$

Remarkably, the theory of exchange bias systems assumes that $T_C > T_N$, however, it has been extensively proved that exchange bias also occurs in inverted systems where $T_C < T_N$. [49–52] In some cases, it was observed that the H_E induced in these systems can persist also into the PM state of the FM ($T > T_C$) and close to T_N. This effect has been proposed to arise from the moments of the FM layer at the interface which are polarized by the magnetic field even

in the PM regime. Under certain conditions, these polarized moments couple with the AFM leading to the exchange bias properties. [51,52]

References

[1] B.D. Cullity, C.D. Graham, Introduction to Magnetic Materials, Second Ed., Wiley-IEEE Press, 2011.

[2] S. Chikazumi, Physics of Ferromagnetism, Oxford University Press, 2009.

[3] X. Batlle, A. Labarta, Finite-size effects in fine particles: magnetic and transport properties, J. Phys. D. Appl. Phys. 35 (2002) R15–R42. doi:10.1088/0022-3727/35/6/201.

[4] G.C. Papaefthymiou, Nanoparticle magnetism, Nano Today. 4 (2009) 438–447. doi:10.1016/j.nantod.2009.08.006.

[5] D. Peddis, C. Cannas, A. Musinu, G. Piccaluga, Magnetism in Nanoparticles: Beyond the Effect of Particle Size, Chem. - A Eur. J. 15 (2009) 7822–7829. doi:10.1002/chem.200802513.

[6] J.L. Dormann, D. Fiorani, E. Tronc, Magnetic Relaxation in Fine-Particle Systems, in: Adv. Chem. Physics, Vol. 98, John Wiley & Sons, Inc., 2007. doi:10.1002/9780470141571.ch4.

[7] J. Frenkel, J. Doefman, Spontaneous and Induced Magnetisation in Ferromagnetic Bodies., Nature. 126 (1930) 274–275. doi:10.1038/126274a0.

[8] C. Kittel, Theory of the Structure of Ferromagnetic Domains in Films and Small Particles, Phys. Rev. 70 (1946) 965–971. doi:10.1103/PhysRev.70.965.

[9] D.L. Leslie-Pelecky, R.D. Rieke, Magnetic Properties of Nanostructured Materials, Chem. Mater. 8 (1996) 1770–1783. doi:10.1021/cm960077f.

[10] E.C. Stoner, E.P. Wohlfarth, A Mechanism of Magnetic Hysteresis in Heterogeneous Alloys, Philos. Trans. R. Soc. A Math. Phys. Eng. Sci. 240 (1948) 599–642. doi:10.1098/rsta.1948.0007.

[11] M. Knobel, W.C. Nunes, L.M. Socolovsky, E. De Biasi, J.M. Vargas, J.C. Denardin, Superparamagnetism and Other Magnetic Features in Granular Materials: A Review on Ideal and Real Systems, J. Nanosci. Nanotechnol. 8 (2008) 2836–2857.

[12] C.P. Bean, J.D. Livingston, Superparamagnetism, J. Appl. Phys. 30 (1959) S120. doi:10.1063/1.2185850.

[13] D. Li, Z. Han, J.G. Zheng, X.L. Wang, D.Y. Geng, J. Li, et al., Spin canting and spin-flop transition in antiferromagnetic Cr2O3 nanocrystals, J. Appl. Phys. 106 (2009) 053913. doi:10.1063/1.3213100.

[14] X. Batlle, X. Obradors, M. Medarde, J. Rodríguez-Carvajal, M. Pernet, M. Vallet-Regí, Surface spin canting in BaFe12O19 fine particles, J. Magn. Magn. Mater. 124 (1993) 228–238. doi:10.1016/0304-8853(93)90092-G.

[15] C.J. Serna, F. Bødker, S. Mørup, M.P. Morales, F. Sandiumenge, S. Veintemillas-Verdaguer, Spin frustration in maghemite nanoparticles, Solid State Commun. 118 (2001) 437–440. doi:10.1016/S0038-1098(01)00150-8.

[16] E. Winkler, R.D. Zysler, M.V. Mansilla, D. Fiorani, Surface anisotropy effects in NiO nanoparticles, Phys. Rev. B. 72 (2005) 132409. doi:10.1103/PhysRevB.72.132409.

[17] R.H. Kodama, S.A. Makhlouf, A.E. Berkowitz, Finite Size Effects in Antiferromagnetic NiO Nanoparticles, Phys. Rev. Lett. 79 (1997) 1393–1396. doi:10.1103/PhysRevLett.79.1393.

[18] R.H. Kodama, A.E. Berkowitz, E.J. McNiff, Jr., S. Foner, Surface Spin Disorder in NiFe 2 O 4 Nanoparticles, Phys. Rev. Lett. 77 (1996) 394–397. doi:10.1103/PhysRevLett.77.394.

[19] B. Martínez, X. Obradors, L. Balcells, A. Rouanet, C. Monty, Low Temperature Surface Spin-Glass Transition in γ- Fe2O3 Nanoparticles, Phys. Rev. Lett. 80 (1998) 181–184. doi:10.1103/PhysRevLett.80.181.

[20] H. Kachkachi, M. Noguès, E. Tronc, D.A. Garanin, Finite-size versus surface effects in nanoparticles, J. Magn. Magn. Mater. 221 (2000) 158–163. doi:10.1016/S0304-8853(00)00390-5.

[21] D.A. Dimitrov, G.M. Wysin, Effects of surface anisotropy on hysteresis in fine magnetic particles, Phys. Rev. B. 50 (1994) 3077–3084. doi:10.1103/PhysRevB.50.3077.

[22] T.J. Daou, J.-M. Greneche, S.-J. Lee, S. Lee, C. Lefevre, S. Bégin-Colin, et al., Spin Canting of Maghemite Studied by NMR and In-Field Mössbauer Spectrometry, J. Phys. Chem. C. 114 (2010) 8794–8799. doi:10.1021/jp100726c.

[23] J. Mazo-Zuluaga, J. Restrepo, F. Muñoz, J. Mejía-López, Surface anisotropy, hysteretic, and magnetic properties of magnetite nanoparticles: A simulation study, J. Appl. Phys. 105 (2009) 123907. doi:10.1063/1.3148865.

[24] X.H. Huang, J.F. Ding, G.Q. Zhang, Y. Hou, Y.P. Yao, X.G. Li, Size-dependent exchange bias in La 0.25 Ca 0.75 Mn O 3 nanoparticles, Phys. Rev. B. 78 (2008) 224408. doi:10.1103/PhysRevB.78.224408.

[25] D. Tobia, E. Winkler, R.D. Zysler, M. Granada, H.E. Troiani, Size dependence of the magnetic properties of antiferromagnetic Cr 2 O 3 nanoparticles, Phys. Rev. B. 78 (2008) 104412. doi:10.1103/PhysRevB.78.104412.

[26] F. Liu, M.R. Press, S.N. Khanna, P. Jena, Magnetism and local order: Ab initio tight-binding theory, Phys. Rev. B. 39 (1989) 6914–6924. doi:10.1103/PhysRevB.39.6914.

[27] R.N. Bhowmik, R. Ranganathan, Enhancement of surface magnetization in antiferromagnetic nanoparticles, Solid State Commun. 141 (2007) 365–368. doi:10.1016/j.ssc.2006.11.029.

[28] M. Ghosh, K. Biswas, A. Sundaresan, C.N.R. Rao, MnO and NiO nanoparticles: synthesis and magnetic properties, J. Mater. Chem. 16 (2006) 106–111. doi:10.1039/B511920K.

[29] J.M. Wesselinowa, Size and anisotropy effects on magnetic properties of antiferromagnetic nanoparticles, J. Magn. Magn. Mater. 322 (2010) 234–237. doi:10.1016/j.jmmm.2009.08.045.

[30] S. Shtrikman, E.P. Wohlfarth, The theory of the Vogel-Fulcher law of spin glasses, Phys. Lett. A. 85 (1981) 467–470. doi:10.1016/0375-9601(81)90441-2.

[31] M. Knobel, W.C. Nunes, A.L. Brandl, J.M. Vargas, L.M. Socolovsky, D. Zanchet, Interaction effects in magnetic granular systems, Phys. B Condens. Matter. 354 (2004) 80–87. doi:10.1016/j.physb.2004.09.024.

[32] J. Dormann, D. Fiorani, E. Tronc, On the models for interparticle interactions in nanoparticle assemblies: comparison with experimental results, J. Magn. Magn. Mater. 202 (1999) 251–267. doi:10.1016/S0304-8853(98)00627-1.

[33] J.L. Dormann, L. Bessais, D. Fiorani, A dynamic study of small interacting particles: superparamagnetic model and spin-glass laws, J. Phys. C Solid State Phys. 21 (1988) 2015–2034. doi:10.1088/0022-3719/21/10/019.

[34] W. Luo, S.R. Nagel, T.F. Rosenbaum, R.E. Rosensweig, Dipole interactions with random anisotropy in a frozen ferrofluid, Phys. Rev. Lett. 67 (1991) 2721–2724. doi:10.1103/PhysRevLett.67.2721.

[35] M. Sasaki, P.E. Jönsson, H. Takayama, P. Nordblad, Comment on "Memory Effects in an Interacting Magnetic Nanoparticle System," Phys. Rev. Lett. 93 (2004) 139701. doi:10.1103/PhysRevLett.93.139701.

[36] S. Mørup, E. Tronc, Superparamagnetic relaxation of weakly interacting particles, Phys. Rev. Lett. 72 (1994) 3278–3281. doi:10.1103/PhysRevLett.72.3278.

[37] D. Kechrakos, K.N. Trohidou, Magnetic properties of dipolar interacting single-domain particles, Phys. Rev. B. 58 (1998) 12169–12177. doi:10.1103/PhysRevB.58.12169.

[38] K. Trohidou, M. Vasilakaki, Magnetic Behaviour of Core/Shell Nanoparticle Assemblies: Interparticle Interactions Effects, K. Trohidou, M. Vasilakaki. 2010. Magn. Behav. Core/Shell Nanoparticle Assem. Interparticle Interact. Eff. Acta Phys. Pol. A 117 374-378. 2 (2010) 374–378. https://www.infona.pl//resource/bwmeta1.element.bwnjournal-article-appv117n253kz (accessed September 18, 2015).

[39] S. Gangopadhyay, G.C. Hadjipanayis, C.M. Sorensen, K.J. Klabunde, Effect of particle size and surface chemistry on the interactions among fine metallic particles, IEEE Trans. Magn. 29 (1993) 2619–2621. doi:10.1109/20.280847.

[40] A. Lyberatos, E.P. Wohlfarth, A monte carlo simulation of the dependence of the coercive force of a fine particle assembly on the volume packing factor, J. Magn. Magn. Mater. 59 (1986) L1–L4. doi:10.1016/0304-8853(86)90002-8.

[41] D. Kechrakos, K.N. Trohidou, M. Vasilakaki, Magnetic properties of dense nanoparticle arrays with core/shell morphology, J. Magn. Magn. Mater. 316 (2007) e291–e294. doi:10.1016/j.jmmm.2007.02.122.

[42] E.F. Kneller, R. Hawig, The exchange-spring magnet: a new material principle for permanent magnets, IEEE Trans. Magn. 27 (1991) 3588–3560. doi:10.1109/20.102931.

[43] E.E. Fullerton, J.. Jiang, S.. Bader, Hard/soft magnetic heterostructures: model exchange-spring magnets, J. Magn. Magn. Mater. 200 (1999) 392–404. doi:10.1016/S0304-8853(99)00376-5.

[44] W.H. Meiklejohn, C.P. Bean, New Magnetic Anisotropy, Phys. Rev. 102 (1956) 1413–1414. doi:10.1103/PhysRev.102.1413.

[45] J. Nogués, I.K. Schuller, Exchange bias, J. Magn. Magn. Mater. 192 (1999) 203–232. doi:10.1016/S0304-8853(98)00266-2.

[46] J. Nogués, J. Sort, V. Langlais, V. Skumryev, S. Suriñach, J.S. Muñoz, et al., Exchange bias in nanostructures, Phys. Rep. 422 (2005) 65–117. doi:10.1016/j.physrep.2005.08.004.

[47] W.H. Meiklejohn, Exchange Anisotropy—A Review, J. Appl. Phys. 33 (1962) 1328. doi:10.1063/1.1728716.

[48] M. Kiwi, Exchange bias theory, J. Magn. Magn. Mater. 234 (2001) 584–595. doi:10.1016/S0304-8853(01)00421-8.

[49] J.W. Cai, K. Liu, C.L. Chien, Exchange coupling in the paramagnetic state, Phys. Rev. B. 60 (1999) 72–75. doi:10.1103/PhysRevB.60.72.

[50] X.W. Wu, C.L. Chien, Exchange coupling in ferromagnet/antiferromagnet bilayers with comparable TC and TN, Phys. Rev. Lett. 81 (1998) 2795–2798. doi:10.1103/PhysRevLett.81.2795.

[51] M.G. Blamire, M. Ali, C.-W. Leung, C.H. Marrows, B.J. Hickey, Exchange Bias and Blocking Temperature in Co / FeMn / CuNi Trilayers, Phys. Rev. Lett. 98 (2007) 217202. doi:10.1103/PhysRevLett.98.217202.

[52] K.D. Sossmeier, L.G. Pereira, J.E. Schmidt, J. Geshev, Exchange bias in a ferromagnet/antiferromagnet system with T[sub C]≪T[sub N], J. Appl. Phys. 109 (2011) 083938. doi:10.1063/1.3572258.

Chapter 3

Synthesis of magnetic nanoparticles

Because of the large range of applications requiring increasing variety of nanoparticles with different size, shape, composition, etc., many different methods have been developed for nanoparticles production. In particular, being at intermediate size between bulk materials and molecules or structures at atomic level, nanoparticles can be obtained through two different strategies: the "*top-down*" approach, which employs physical methods for the size reduction of bulk materials, and the "*bottom-up*" approach, where nanostructures are grown starting from constituent atoms or molecules. [1–5] Top-down approach includes milling or attrition, repeated quenching and lithography. The main advantage of most of these techniques is the possibility to yield a large amount of material, although often the synthesis of uniform-sized nanoparticles and their size and shape control is very difficult to achieve. Moreover, as is the case of milling, nanoparticles may contain a significant amount of impurities from the milling medium and defects arising from the milling process. Conversely, *bottom-up* approach allows obtaining nanoparticles with controlled size and size distribution, despite generally only sub-gram quantities can be produced. Among *bottom-up* synthetic techniques, the colloidal chemical synthesis allows the formation of various-shaped nanoparticles and hybrid nanostructure where different materials are combined providing new and innovative materials not present as bulk phases.

Because of the high control on particles morphology, shape, size-distribution, composition and structure required for an accurate analysis of the correlation between magnetic properties and nanostructure, in the present work *bottom-up* colloidal chemical synthesis was used for nanoparticles preparation. Therefore, in this Chapter we will briefly discuss the theoretical and technical aspects of this technique.

3.1 Nucleation and growth theory

The mechanism of formation of monodisperse nanoparticles is composed of two main processes: nucleation and growth. [6–8] Although these two processes are strongly correlated, from the theoretical point of view they can be described separately, so that a better understanding of the driving forces at the basis of each of them can be realized. The first theory, which is based on the conceptual separation of nucleation and growth into two stages, was reported by LaMer in 1950. [9,10] According to the LaMer mechanism, the process of nucleation and growth can be divided into three steps:

(I) a rapid increase in the concentration of free monomers (i.e., the minimum subunit of bulk crystal) in solution;
(II) the monomer undergoes "*burst nucleation*" i.e., many nuclei are generated at the same time, which significantly reduces the concentration of free monomers in solution avoiding additional nucleation;
(III) the particle growth occurs under the control of the diffusion of the monomers through the solution.

The three stages are shown in Figure 3.1 where the concentration of the monomers, in term of monomers supersaturation (see Equation 3.1), is schematically plotted as a function of time.

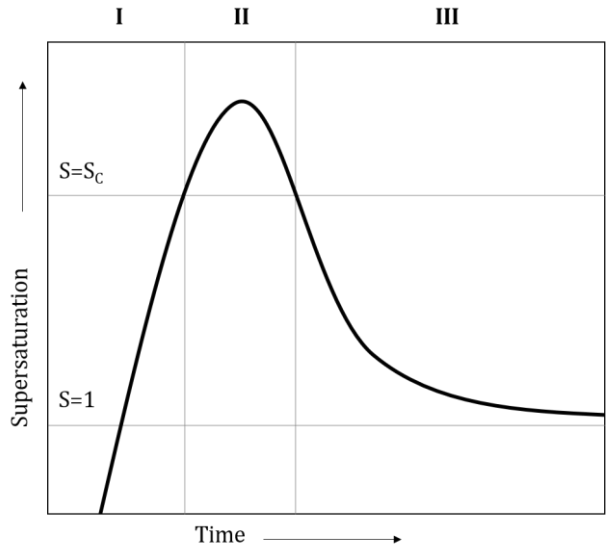

Figure 3.1: LaMer plot figuring supersaturation (*S*) evolution with time.

Therefore, in order to obtain monodisperse particles it is necessary to induce a single nucleation event preventing additional nucleation during the subsequent growth process. This will ensure that the growth of each formed nucleus will be the same. Consequently, any variation in particle size, size-distribution and shape can be achieved controlling these two

stages. In general, the final size depends mainly on the nucleation process, while the size-distribution and shape depend on the growth one. The nucleation and growth steps are affected by many parameters such as nanoparticles interface energy, chemical potential of the monomers, and the different atomic species in the monomers and particles. Moreover, also stabilizing agents, as surfactants, which are usually involved in the reaction intermediate, play an important role in both steps, which will be separately discussed in the following sections.

3.1.1 Nucleation

The term "nucleation" refers to the process of spontaneous formation of the smallest stable crystallites. In this process, many nuclei are generated at the same time, and then start to grow without additional nucleation. The nucleation process involves basically an initial homogeneous solution which is transformed into a heterogeneous one due to the formation of the nuclei. Since the solution needs to spontaneously change from a homogeneous to a heterogeneous system, there exists a high energy barrier for nucleation. Therefore, for the homogeneous nucleation to occur, i.e. the nucleation in absence of pre-existing nuclei or seeds, favourable kinetic and thermodynamic conditions are required. In contrast, heterogeneous nucleation is governed by pre-existing nuclei in the solution, i.e. it starts from a heterogeneous initial solution, where the nanocrystals grow on the pre-existing nuclei, consequently avoiding the need to overcome the high energy barrier for nuclei formation. [6–9,11]

The homogeneous nucleation takes place when the supersaturation, S, of the precursors overcomes its critic value (S_C) (see Figure 3.1). As soon as nuclei are formed, the precursors supersaturation decreases below S_C, avoiding, thus, further nucleation processes. [9] The energy barrier, which must be overcome to reach the nucleation step, is thermodynamically represented by the sum of two contributions: the Gibbs free energy needed to create a nucleus per unit of volume (ΔG_V) and the surface energy of the formed nucleus (ΔG_S) given by. [12]

$$\Delta G_V = -\frac{RT}{V_M} lnS \quad \text{where} \quad S = \frac{C}{C_S} \tag{3.1}$$

$$\Delta G_S = \gamma A \tag{3.2}$$

where R is the gas constant, T the temperature, V_M the molar volume of the bulk crystal, C the precursor concentration, C_S the saturation concentration of the precursor, γ the surface free energy per unit area and A the surface area of the formed nuclei. In Equation 3.1 when the concentration overcomes the supersaturation regime ($C > C_S$), lnS reaches positive values leading to negative ΔG_V. On the contrary, ΔG_S is always positive. Then, combining both equations and assuming spherical shape of the nuclei, the total Gibbs free energy becomes:

$$\Delta G = 4\pi r^2\gamma + \frac{4}{3}\pi r^3 \Delta G_V \qquad 3.3$$

where r is the radius of the formed nuclei. Because of the opposite signs of the two contributions, a plot of ΔG versus r has a maximum (see Figure 3.2). The value of r at which ΔG is maximum is called the critical radius, r_C, and corresponds to the minimum radius of a nucleus that can form spontaneously in the supersaturated solution.

$$r_C = \frac{-2\gamma}{\Delta G_V} = \frac{2\gamma V_M}{RTlnS} \qquad 3.4$$

Substituting Equation 3.4 into Equation 3.3 gives the critical free energy, ΔG_{crit}, which is the free energy necessary to form a stable nucleus.

$$\Delta G_{crit} = \frac{16\pi\gamma^3}{3(\Delta G_V)^2} = \frac{16\pi\gamma^3 V_M^2}{3(RTlnS)^2} \qquad 3.5$$

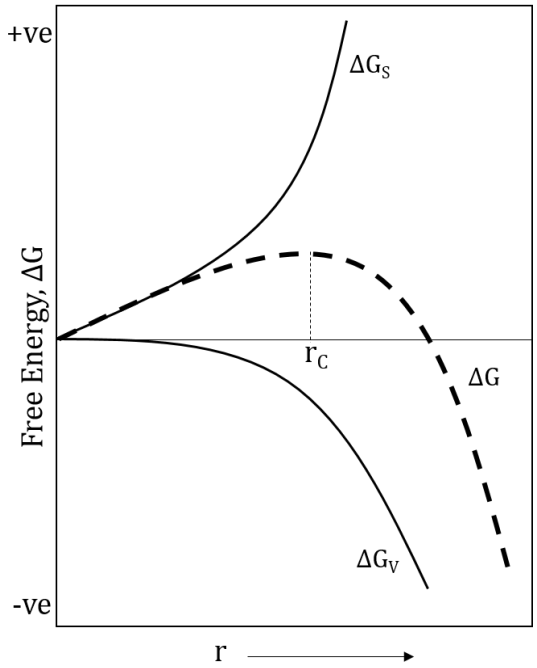

Figure 3.2: Free energy diagram for nucleation explaining the existence of a "critical nucleus". [13]

The nucleation rate, $\dot{N}$, defined as the rate of increase of the number of particle, N, can be expressed by an Arrhenius law: [12]

$$\dot{N} = \frac{dN}{dt} = A\,exp\left[-\frac{\Delta G_{crit}}{k_B T}\right] = A\,exp\left[\frac{16\pi\gamma^3 V_M^2}{3k_B^3 T^3 N_A^2 (lnS)^2}\right] \quad 3.6$$

It should be noted that it is hard to define exactly a S_C level at which nucleation begins; indeed, because of energy fluctuation in the solution, nucleation and re-dissolution could happen at any concentration. [8] In fact, the nucleus can form even in unsaturated solution; on the other hand, the formed particles can re-dissolve unless they are stable enough to resist the free energy fluctuation of their surroundings. However, rewriting Equation 3.6 with S expressed as a function of $\dot{N}$, it emerges another necessary condition related to the degree of supersaturation:

$$lnS = \left[\frac{16\pi\gamma^3 V_M^2}{3k_B^3 T^3 ln(A/\dot{N})}\right]^{1/2} \quad 3.7$$

Namely, to start the accumulation of the nuclei, the nucleation rate should be high enough to overcome the re-dissolution rate of the particles. Thus, we can define S_C as the point at which the nucleation rate is sufficiently high that the number of nuclei increases even while smaller nuclei may dissolve away.

3.1.2 Growth

The growth process can be divided in two different steps: first the monomers formation, diffusion and adsorption at the particle surface, and, after, the monomers reaction at the surface and the particle growth. [8] As a typical kinetic problem, the growth rate can be easily treated by choosing the slowest mechanism as the limiting step. Taking into account that nucleation, monomers formation and monomer reaction are instantaneous processes, the diffusion can be considered as the limiting step of the entire process. [6,8,9,11] Therefore, the growth of nanoparticle can be expressed in term of the flux of the monomers (J), i.e. the monomer diffusion to the particle surface. In the Reiss model, [6,14] also called *growth by diffusion,* the growth rate of spherical particles depends solely on J according to the following relationship:

$$J = \frac{4\pi r^2}{V_M}\frac{dr}{dt} \quad 3.8$$

Moreover, applying the Fick's first law J is also given by:

$$J = 4\pi x^2 D\frac{dC}{dx} \quad 3.9$$

where D is the diffusion coefficient, C the monomer concentration, x ($\geq r$) is the monomer distance inside the solution from the centre of the particle and r is the particle radius.

Therefore, assuming D to be constant with x and integrating $C(x)$ in the entire diffusion layer, Equation 3.9 becomes:

$$J = 4\pi x^2 D\left(C_{bulk} - C_{surf}\right) \qquad 3.10$$

where C_{bulk} and C_{surf} are the bulk and surface concentration, respectively. Then, combining equations 3.8 and 3.10 it is possible to relate the growth rate to the monomer diffusion:

$$\frac{dr}{dt} = \frac{V_M D}{r}\left(C_{bulk} - C_{surf}\right) \qquad 3.11$$

Consequently, if C_{bulk} and C_{surf} are considered constant for all the particles, the growth rate is inversely proportional to the nanoparticle radius. This implies that the growth rate of a particle decreases as the radius increases, and, thus, the size-distribution of the nanoparticles is always smaller than the distribution of the nuclei. This is a self-regulating mechanism of the size-distribution during the growth process and it is often referred to as the *focusing effect*. [6,15]

However, Reiss model is an oversimplification of the process not accounting for the reaction kinetics of crystal growth and its size dependence. Indeed, during the growth process, precipitation and dissolution of the particles occur simultaneously. Therefore, in order to figure out the general size dependence of the process, both mechanisms have to be considered.

$$nM^{sol} \underset{k_d}{\overset{k_p}{\rightleftharpoons}} M_n^{crist} \qquad 3.12$$

where M^{sol} and M^{crist} refer to monomers in solution and in the crystal, while k_p and k_d are the reaction rate constants for precipitation and dissolution, respectively. From the activated complex theory, the reaction rate constants are related to the change in chemical potential, $\mu(r)$, with respect to the bulk values, μ^0:

$$k_p = k_p^0 \, exp\left[-\alpha\frac{\Delta\mu}{RT}\right] \qquad 3.13$$

$$k_d = k_d^0 \, exp\left[(1-\alpha)\frac{\Delta\mu}{RT}\right] \qquad 3.14$$

where α is the transfer coefficient and k^0 the rate constant for the bulk crystal. [16] In particular, the change of $\mu(r)$ arises from the surface free energy variation related to size modification accordingly to Gibbs-Thomson equation.

$$\Delta\mu = \mu(r) - \mu^0 = \frac{2\gamma V_M}{r} \qquad 3.15$$

Thus, being $\Delta\mu$ inversely proportional to the particles radius, equations 3.13 and 3.14 reveal that, the smaller are the particles, the slower is the growth process, while the dissolution becomes easier. The combination of these two effects contributes in opposite direction with respect to what predicted by the Reiss model. Therefore, in order to properly describe the effective growth rate dependence on particle radius, Equation 3.11 has to be modified introducing the effect of kinetic processes on C_{surf}, which cannot be considered constant for all the nanoparticles. Indeed, both precipitation and dissolution generate a monomer flux at the particle surface, indicated as J_p and J_d, respectively:

$$J_p = 4\pi r^2 k_p^0 C_{surf}\, exp\left[-\alpha\frac{2\gamma V_M}{rRT}\right] \qquad 3.16$$

$$J_d = -\,4\pi r^2 k_d^0\, exp\left[(1-\alpha)\frac{2\gamma V_M}{rRT}\right] \qquad 3.17$$

The net flux is the sum of the two contributions and can be equated to the integrated form of Fick's law(Equation 3.10) to obtain the C_{surf} dependence with *r:* [6]

$$J = J_p + J_d = 4\pi r^2 k_p^0 C_{surf}\, exp\left[-\alpha\frac{2\gamma V_M}{rRT}\right] - 4\pi r^2 k_d^0\, exp\left[(1-\alpha)\frac{2\gamma V_M}{rRT}\right] \qquad 3.18$$

$$C_{surf} = \left[\frac{k_d^0\, r\, exp\left[(1-\alpha)\frac{2\gamma V_M}{rRT}\right] + DC_{bulk}}{k_p^0\, exp\left[-\alpha\frac{2\gamma V_M}{rRT}\right] + D}\right] \qquad 3.19$$

Therefore, substituting C_{surf} in the Equation 3.11, the growth rate to the monomer diffusion becomes:

$$\frac{dr}{dt} = V_M D C_{s,eq}^0\left[\frac{S - exp\left[\frac{2\gamma V_M}{rRT}\right]}{r + \frac{D}{k_p^0} exp\left[\alpha\frac{2\gamma V_M}{rRT}\right]}\right] \qquad 3.20$$

From Equation 3.20, it emerges the non-monotonic dependence of the growth rate with particle size, as reported in Figure 3.3. In particular, for small *r,* the crystal chemical potential is highly sensitive to changes in particle size and hence to precipitation and dissolution processes. Moreover, the exponential contribution makes the growth mechanism to be mainly determined by the kinetic process. Hence, as particles size decreases the precipitation rate decreases while the dissolution rate increases broadening the size distribution (*"defocusing" region*). On the other hand, for large *r,* size dependent variations in crystal chemical potential become relatively small and the growth rate mainly depends on the diffusion process. In this case, the growth rate decreases with particle size narrowing the size-distributions (*"focusing" region*). [13]

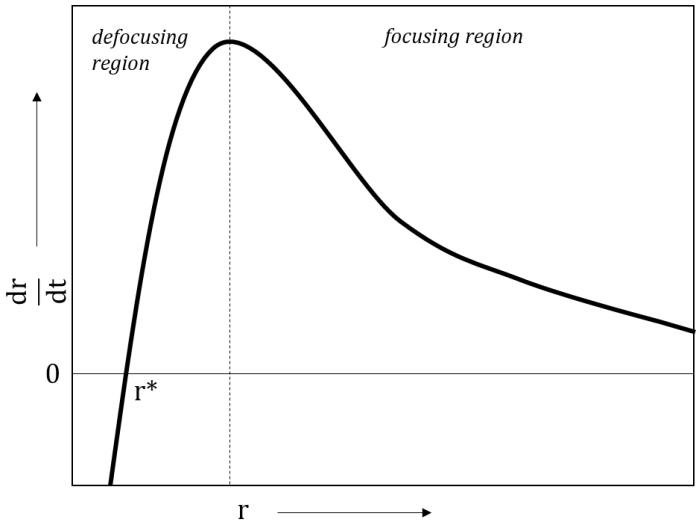

Figure 3.3: Evolution of the growth rate as a function of particle radius.

It has to be noted that in the defocusing region the growth rate changes sign indicating the minimum particle radius in equilibrium within the bulk solution (r^*) that is equal to the evaluated r_C from the nucleation model (see Equation 3.4).

$$r^* = r_C = \frac{2\gamma V_M}{RT ln S} \qquad 3.21$$

According to Equation 3.20 S and $D/k_P{}^0$, that represents the ratio between the diffusion and the precipitation rates, strongly affect the growth rate dependence on r. Particularly, if $D/k_P{}^0$ is very small, the overall growth reaction rate is controlled by the diffusion process (*diffusion-controlled growth*). Consequently, the smaller the value is, the more effective the narrowing of the size-distribution becomes. Conversely, if $D/k_P{}^0$ is very large, the growth rate is mainly determined by the kinetic process (*reaction-controlled growth*) and the "focusing" effect is weakened. On the other hand, an increase in the value of S always results in the enhancement of the growth rate, however, such an increment is more important for smaller particles. In conclusion, both the increase of S and the decrease of $D/k_P{}^0$ enhances the "focusing" mechanism.

3.1.3 Separating the Nucleation and Growth processes

As it has been described above, the route to synthesize monodisperse nanoparticles is to separate the nucleation and growth processes and to control the growth via diffusion of monomers as the limiting step. Heterogeneous nucleation is, probably, the most apparent way for the separation of nucleation and growth. In particular, the separation is achieved by avoiding the nucleation step by using pre-synthesized nanoparticles as seed nuclei and

controlling the precursor concentration far below the supersaturation regime. This method, known as the "*seeded-mediated growth*", allows to create a broad range of different nanocrystalline structures. For example, it has been extensively used in the synthesis of large particles composed of a single material [17,18] or hybrid nanostructures composed of different phases like core|shell, onion-like structures or heterodimers. [19–22] Nevertheless, there exist also techniques separating the nucleation and growth processes starting from a homogeneous nucleation and afterwards establishing the diffusion process as the limiting step: "*hot-injection*" and "*heating-up*" methods are two examples. *Hot-injection* consists of injecting the precursors into a hot surfactant solution to force a *burst nucleation* by the high degree of supersaturation occurring after the addition of the precursor. During the nucleation process, the monomers concentration sharply decreases and, thus, nucleation rate decays. [23–25] The *heating-up* approach consists in mixing the precursors, surfactants and solvent at room temperature and subsequently heating the mixture to the desired decomposition temperature at which the nucleation occurs and, at the same time, the supersaturation decreases. [17,18,26]

3.2 Synthetic techniques

The *bottom-up* approach comprises several different techniques, both occurring in liquid (e.g., co-precipitation, microemulsion, thermal decomposition, etc.), gas (chemical vapour deposition, arc discharge, laser pyrolysis) or solid phases (combustion, annealing). [27] Thanks to their versatility, control on size and size-distribution and purity of the obtained materials, liquid phase syntheses are the most popular strategies. [28,29] Here a brief description of the main liquid phase synthesis techniques for the production of magnetic metal oxides nanoparticle is provided.

3.2.1 Co-precipitation

Co-precipitation is a facile and scalable way to synthesize magnetic nanoparticles starting from aqueous solutions of inorganic salts by the addition of a base or a reducing agent. The reaction is carried out under inert atmosphere at room temperature or at elevate temperature. [30] The size, shape and composition of the nanoparticles can be tuned by varying the precursors (e.g. chlorides, nitrates, sulphates), [29] the precursors concentrations, [28] the type of base, [31] the reaction temperature, [32] the aqueous media (e.g. pH values and ionic strength) [33,34] and the presence of surfactants. However, nanoparticles synthesized by co-precipitation are characterized by high polidispersity and poor crystallinity. In fact, generally, subsequent annealing processes are necessary in order to achieve good magnetic properties.

3.2.2 Microemulsion

Water-in-oil (W/O) microemulsion are based on the same process of co-precipitation, although the reaction is carried out in a confined media, thus decreasing the polydispersity of nanoparticles. In fact, in W/O micelles the aqueous phase is dispersed as nanodroplets surrounded by a surfactant monolayer in a hydrocarbon media. Such dispersion can be used as a series of nanoreactors for the formation of nanoparticles, the precipitation occurring within the micelles. In particular, the nanoparticle synthesis is carried out by mixing two water-in-oil microemulsion containing the proper reagents and, as the droplets collide and coalesce, they reactants mix and the nanoparticles formation takes place. [35,36] Size, size-distributions and shape of the nanoparticles are determined by the micelles acting as cages and can be tuned varying surfactant, water-to-surfactant ratio, water-to-oil ratio and temperature. [37] However, the range of stability of the microemulsion has to be taken in account in the synthesis condition selection; the temperature working window for this synthesis is usually quite narrow often affecting the size-range and the crystallinity of the product. Moreover, the yield of nanoparticles is extremely low compared to other techniques and large amounts of solvent are necessary to synthesize appreciable quantities of material.

3.2.3 Hydrothermal synthesis

Hydrothermal synthesis exploits the increase of the reaction temperature to improve nanoparticles crystallinity. In fact, an aqueous solution of inorganic salts precursors is heated in reactors or autoclaves at high pressure increasing, hence, the mixture boiling point. During the heating process, metal hydroxides form as intermediate, which then evolves to metal oxide nanoparticles. [38] Moreover, hydrothermal synthesis can be carried out using other solvents (e.g., ethylene glycol) instead of water. Such modified route takes the name of solvothermal synthesis. [39] In both cases, precursor concentrations, reaction time and temperature can be properly adjusted to tune particle size and shape. [40] However, even if solvothermal technique is very versatile, this method is characterized by slow reaction kinetics at any temperature that dramatically increases the reaction time resulting in enhanced polydispersity of the system.

3.2.4 Polyol synthesis

Like hydrothermal synthesis, polyol one is a feasible alternative approach for the synthesis of nanoparticles with improved crystallinity and relatively low polydispersity. In this method, the use of polyols (e.g polyethyleneglycol) as a solvent offers the possibility of both dissolving inorganic salt and carrying out the reaction at high temperature, thanks to their relatively high boiling points. [19] Moreover, polyols act also as reducing agents as well as stabilizers to control particle growth and prevent interparticle aggregation. In this process,

the precursors are dissolved in a liquid polyol and the mixture is heated to the desired reaction temperature that can be as high as the boiling point of the polyol. During the heating process the metal precursors create an intermediate complex forming firstly the nuclei and, then, the final particles. Precursor concentration, reaction time and temperature can be proper adjusted to tune particle size and shape. [41]

3.2.5 Thermal decomposition

Highly monodispersed nanoparticles with a good control on their size and shape can be obtained by high-temperature decomposition of organometallic precursors as metal-acetylacetonate, metal-carbonyl, metal complex with fatty acids conjugate base, etc. in organic solvents. The synthesis takes place in the presence of surfactants (e.g., oleic acid, oleylamine, lauric acid, 1,2-hexadecanediol, etc.) that act both as stabilizing agents for the obtained nanoparticles and as reagent for the formation of reaction intermediates in the synthetic process. Thermal decomposition of organometallic precursors where the metal is in the zero-valent oxidation state (e.g., metal-carbonyl) initially leads to a formation of metal nanoparticles that, if followed by an oxidation step, can lead to high quality monodispersed metal oxides. [42] On the other hand, decomposition of precursors with cationic metal centres (e.g., metal-acetylacetonate) leads directly to metal oxides nanoparticles. [29] Principally, precursor concentration, metal-to-surfactant ratio, type of surfactant and solvent are the decisive parameters for controlling the size and morphology of the obtained nanoparticles. Moreover, the reaction temperature and time, the heating rate as well as the aging period may also be crucial for the precise control of size, morphology and crystal phase. [43,44]

In this thesis we have investigated different metal-doped iron oxide nanoparticles; thanks to the high control on size, size-distribution, shape, composition and crystallinity, thermal decomposition technique has been chosen for the synthesis of the entire series of the presented materials. As described above, the features of nanoparticle synthesized thorough thermal decomposition can be controlled by a large series of parameters. Based on the previously reported nucleation and growth theory and on the large number of experimental data reported in the literature, here a brief description on the role of the main synthetic parameters is provided.

As can be deduced from Equation 3.6, high temperature during nucleation process (T_1) will promote the formation of a high number of nuclei, while an increase in the temperature during the growth stage (T_2) results in an enhancement of dissolution of smaller nanoparticles (see Equations 3.17). Hence, the setting of high T_1 or T_2 in the heating procedure will produce smaller or larger nanoparticles, respectively. Thus, the choice of the

solvent, whose boiling point determines the highest exploitable T_2, affects strongly the final particle size. [45]

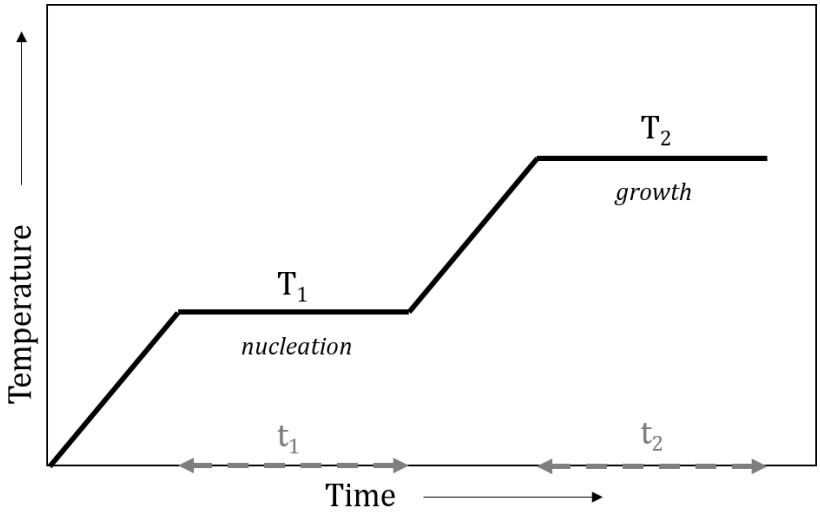

Figure 3.4: Schematic description of the heating procedure used in the thermal decomposition synthesis.

Besides temperature, also reaction time can be varied: with long growth time (t_2), larger nanoparticle size are obtained while the size-distribution decreases because the focusing region is extended. On the other hand, short nucleation time (t_1) limits heterogeneous nucleation. Hence, in order to have small size-distribution it is appropriate to set short t_1 and long t_2. [45]

Another crucial parameter is the type of surfactant used in the synthetic process. In fact the surfactant strongly affects both monomer reactivity and particle surface energy, controlling, thus, the entire crystal growth. [46,47] Indeed, during the synthesis the surfactant is involved both in the nucleation process, forming an intermediate complex with the precursor, and in the growth stage, where it acts as stabilizing agent preventing nanoparticles agglomeration. Therefore, as the interaction between surfactant and precursor becomes stronger, the lower will be the intermediate reactivity and higher T_1 and T_2 are necessary for nucleation and growth processes to occur, and *vice versa*. Similarly, as the strength of the interaction between surfactants and particles surface increases (lower surface energy), the growth stage slows down, accordingly with Equation 3.20. [47,48] Moreover, exploiting the different affinity of surfactants for different crystallographic faces, it is also possible to tune nanoparticle shape, as, for example, lower affinity faces will grow faster. [7] Particularly, the effect of surfactant depends both on its polar part, (oxygen or nitrogen determine stronger or weaker interaction with precursors or particle surface), and on the hydrophobic chain, (longer chains increase intermediate stability and decrease surface energy of the particles).

References

[1] K.J. Klabunde, Nanoscale Materials in Chemistry, Wiley-Interscience, New York, 2001.

[2] A.L. Rogach, D.V. Talapin, E.V. Shevchenko, A. Kornowski, M. Haase, H. Weller, Organization of Matter on Different Size Scales: Monodisperse Nanocrystals and Their Superstructures, Adv. Funct. Mater. 12 (2002) 653–664. doi:10.1002/1616-3028(20021016)12:10<653::AID-ADFM653>3.0.CO;2-V.

[3] T. Hyeon, Chemical synthesis of magnetic nanoparticles, Chem. Commun. (2003) 927–934. doi:10.1039/b207789b.

[4] G. Schmid, Nanoparticles: From Theory to Application, Wiley-VCH , Weinheim, 2004.

[5] Fendler, Nanoparticles and Nanostructured Films, Wiley-VCH, Weinheim, 1998.

[6] J. Park, J. Joo, S.G. Kwon, Y. Jang, T. Hyeon, Synthesis of monodisperse spherical nanocrystals., Angew. Chem. Int. Ed. Engl. 46 (2007) 4630–60. doi:10.1002/anie.200603148.

[7] P.D. Cozzoli, Advanced Wet-Chemical Synthetic Approaches to Inorganic Nanostructures, Transworld Research Network, 2008.

[8] T. Sugimoto, Monodispersed Particles, First Ed., Elsevier, 2001.

[9] V.K. LaMer, R.H. Dinegar, Theory, Production and Mechanism of Formation of Monodispersed Hydrosols, J. Am. Chem. Soc. 72 (1950) 4847–4854. doi:10.1021/ja01167a001.

[10] V.K. La Mer, Nucleation in Phase Transitions., Ind. Eng. Chem. 44 (1952) 1270–1277. doi:10.1021/ie50510a027.

[11] I.M. Lifshitz, V.V. Slyozov, The kinetics of precipitation from supersaturated solid solutions, J. Phys. Chem. Solids. 19 (1961) 35–50. doi:10.1016/0022-3697(61)90054-3.

[12] J.W. Mullin, Crystallization, Third Ed., Oxford University Press, Oxford, 1993.

[13] N.T.K. Thanh, N. Maclean, S. Mahiddine, Mechanisms of Nucleation and Growth of Nanoparticles in Solution, Chem. Rev. 114 (2014) 7610–7630. doi:10.1021/cr400544s.

[14] H. Reiss, The Growth of Uniform Colloidal Dispersions, J. Chem. Phys. 19 (1951) 482. doi:10.1063/1.1748251.

[15] X. Peng, J. Wickham, A.P. Alivisatos, Kinetics of II-VI and III-V Colloidal Semiconductor Nanocrystal Growth: "Focusing" of Size Distributions, J. Am. Chem. Soc. 120 (1998) 5343–5344. doi:10.1021/ja9805425.

[16] D. V. Talapin, A.L. Rogach, M. Haase, H. Weller, Evolution of an Ensemble of Nanoparticles in a Colloidal Solution: Theoretical Study, J. Phys. Chem. B. 105 (2001) 12278–12285. doi:10.1021/jp012229m.

[17] S. Sun, H. Zeng, Size-Controlled Synthesis of Magnetite Nanoparticles, J. Am. Chem. Soc. 124 (2002) 8204–8205. doi:10.1021/ja026501x.

[18] S. Sun, H. Zeng, D.B. Robinson, S. Raoux, P.M. Rice, S.X. Wang, et al., Monodisperse MFe 2 O 4 (M = Fe, Co, Mn) Nanoparticles, J. Am. Chem. Soc. 126 (2004) 273–279. doi:10.1021/ja0380852.

[19] D. Jézéquel, J. Guenot, N. Jouini, F. Fiévet, Submicrometer zinc oxide particles: Elaboration in polyol medium and morphological characteristics, J. Mater. Res. 10 (1995) 77–83. doi:10.1557/JMR.1995.0077.

[20] G. Salazar-Alvarez, H. Lidbaum, A. López-Ortega, M. Estrader, K. Leifer, J. Sort, et al., Two-, Three-, and Four-Component Magnetic Multilayer Onion Nanoparticles Based on Iron Oxides and Manganese Oxides, J. Am. Chem. Soc. 133 (2011) 16738–16741. doi:10.1021/ja205810t.

[21] A. López-Ortega, M. Estrader, G. Salazar-Alvarez, S. Estradé, I. V Golosovsky, R.K. Dumas, et al., Strongly exchange coupled inverse ferrimagnetic soft/hard, MnxFe3−xO4/FexMn3−xO4, core/shell

heterostructured nanoparticles, Nanoscale. 4 (2012) 5138. doi:10.1039/c2nr30986f.

[22] M.R. Buck, J.F. Bondi, R.E. Schaak, A total-synthesis framework for the construction of high-order colloidal hybrid nanoparticles, Nat. Chem. 4 (2011) 37–44. doi:10.1038/nchem.1195.

[23] V.F. Puntes, Colloidal Nanocrystal Shape and Size Control: The Case of Cobalt, Science (80-.). 291 (2001) 2115–2117. doi:10.1126/science.1057553.

[24] P. Bracconi, Molecular-field treatment of the high temperature susceptibility and Néel temperature of type II antiferromagnetic solid-solutions xNiO−(1−x)CoO, J. Magn. Magn. Mater. 40 (1983) 37–47. doi:10.1016/0304-8853(83)90008-2.

[25] T. Hyeon, S.S. Lee, J. Park, Y. Chung, H. Bin Na, Synthesis of Highly Crystalline and Monodisperse Maghemite Nanocrystallites without a Size-Selection Process, J. Am. Chem. Soc. 123 (2001) 12798–12801. doi:10.1021/ja016812s.

[26] J. Park, K. An, Y. Hwang, J.-G. Park, H.-J. Noh, J.-Y. Kim, et al., Ultra-large-scale syntheses of monodisperse nanocrystals, Nat. Mater. 3 (2004) 891–895. doi:10.1038/nmat1251.

[27] M. Faraji, Y. Yamini, M. Rezaee, Magnetic nanoparticles: Synthesis, stabilization, functionalization, characterization, and applications, J. Iran. Chem. Soc. 7 (2010) 1–37. doi:10.1007/BF03245856.

[28] S. Laurent, D. Forge, M. Port, A. Roch, C. Robic, L. Vander Elst, et al., Magnetic iron oxide nanoparticles: synthesis, stabilization, vectorization, physicochemical characterizations, and biological applications., Chem. Rev. 108 (2008) 2064–110. doi:10.1021/cr068445e.

[29] A.-H. Lu, E.L. Salabas, F. Schüth, Magnetic Nanoparticles: Synthesis, Protection, Functionalization, and Application, Angew. Chemie Int. Ed. 46 (2007) 1222–1244. doi:10.1002/anie.200602866.

[30] H. Iida, K. Takayanagi, T. Nakanishi, T. Osaka, Synthesis of Fe3O4 nanoparticles with various sizes and magnetic properties by controlled hydrolysis, J. Colloid Interface Sci. 314 (2007) 274–280. doi:10.1016/j.jcis.2007.05.047.

[31] C. Hu, Z. Gao, X. Yang, Fabrication and magnetic properties of Fe3O4 octahedra, Chem. Phys. Lett. 429 (2006) 513–517. doi:10.1016/j.cplett.2006.08.041.

[32] R.F. Ziolo, E.P. Giannelis, B.A. Weinstein, M.P. O'Horo, B.N. Ganguly, V. Mehrotra, et al., Matrix-Mediated Synthesis of Nanocrystalline gamma-Fe2O3: A New Optically Transparent Magnetic Material, Science (80-.). 257 (1992) 219–223. doi:10.1126/science.257.5067.219.

[33] L. Shen, P.E. Laibinis, T.A. Hatton, Bilayer Surfactant Stabilized Magnetic Fluids: Synthesis and Interactions at Interfaces, Langmuir. 15 (1999) 447–453. doi:10.1021/la9807661.

[34] X.-P. Qiu, Synthesis and characterization of magnetic nano particles, Chinese J. Chem. 18 (2010) 834–837. doi:10.1002/cjoc.20000180607.

[35] J.A. López Pérez, M.A. López Quintela, J. Mira, J. Rivas, S.W. Charles, Advances in the Preparation of Magnetic Nanoparticles by the Microemulsion Method, J. Phys. Chem. B. 101 (1997) 8045–8047. doi:10.1021/jp972046t.

[36] P.A. Dresco, V.S. Zaitsev, R.J. Gambino, B. Chu, Preparation and Properties of Magnetite and Polymer Magnetite Nanoparticles, Langmuir. 15 (1999) 1945–1951. doi:10.1021/la980971g.

[37] S. Santra, R. Tapec, N. Theodoropoulou, J. Dobson, A. Hebard, W. Tan, Synthesis and Characterization of Silica-Coated Iron Oxide Nanoparticles in Microemulsion: The Effect of Nonionic Surfactants, Langmuir. 17 (2001) 2900–2906. doi:10.1021/la0008636.

[38] J. Wang, J. Sun, Q. Sun, Q. Chen, One-step hydrothermal process to prepare highly crystalline Fe3O4 nanoparticles with improved magnetic properties, Mater. Res. Bull. 38 (2003) 1113–1118. doi:10.1016/S0025-5408(03)00129-6.

[39] F. Gözüak, Y. Köseoğlu, A. Baykal, H. Kavas, Synthesis and characterization of CoxZn1−xFe2O4 magnetic nanoparticles via a PEG-assisted route, J. Magn. Magn. Mater. 321 (2009) 2170–2177.

doi:10.1016/j.jmmm.2009.01.008.

[40] J. Wang, F. Ren, R. Yi, A. Yan, G. Qiu, X. Liu, Solvothermal synthesis and magnetic properties of size-controlled nickel ferrite nanoparticles, J. Alloys Compd. 479 (2009) 791–796. doi:10.1016/j.jallcom.2009.01.059.

[41] F. FIEVET, J. LAGIER, B. BLIN, B. BEAUDOIN, M. FIGLARZ, Homogeneous and heterogeneous nucleations in the polyol process for the preparation of micron and submicron size metal particles, Solid State Ionics. 32-33 (1989) 198–205. doi:10.1016/0167-2738(89)90222-1.

[42] S. Lefebure, E. Dubois, V. Cabuil, S. Neveu, R. Massart, Monodisperse magnetic nanoparticles: Preparation and dispersion in water and oils, J. Mater. Res. 13 (1998) 2975–2981. doi:10.1557/JMR.1998.0407.

[43] S. Basak, D.-R. Chen, P. Biswas, Electrospray of ionic precursor solutions to synthesize iron oxide nanoparticles: Modified scaling law, Chem. Eng. Sci. 62 (2007) 1263–1268. doi:10.1016/j.ces.2006.11.029.

[44] R. Massart, E. Dubois, V. Cabuil, E. Hasmonay, Preparation and properties of monodisperse magnetic fluids, J. Magn. Magn. Mater. 149 (1995) 1–5. doi:10.1016/0304-8853(95)00316-9.

[45] V.L. Calero-ddelc, A.M. Gonzalez, C. Rinaldi, A Statistical Analysis to Control the Growth of Cobalt Ferrite Nanoparticles Synthesized by the Thermodecomposition Method, J. Manuf. Sci. Eng. 132 (2010) 030914. doi:10.1115/1.4001717.

[46] M.F. Casula, Y.-W. Jun, D.J. Zaziski, E.M. Chan, A. Corrias, A.P. Alivisatos, The Concept of Delayed Nucleation in Nanocrystal Growth Demonstrated for the Case of Iron Oxide Nanodisks, J. Am. Chem. Soc. 128 (2006) 1675–1682. doi:10.1021/ja056139x.

[47] C.B. Murray, S. Sun, H. Doyle, T. Betley, Monodisperse 3d Transition-Metal (Co,Ni,Fe) Nanoparticles and Their Assembly intoNanoparticle Superlattices, MRS Bull. 26 (2001) 985–991. doi:10.1557/mrs2001.254.

[48] A.C.S. Samia, J.A. Schlueter, J.S. Jiang, S.D. Bader, C.-J. Qin, X.-M. Lin, Effect of Ligand–Metal Interactions on the Growth of Transition-Metal and Alloy Nanoparticles, Chem. Mater. 18 (2006) 5203–5212. doi:10.1021/cm0610579.

Chapter 4

Single-phase cobalt ferrite nanoparticles

Spinel ferrites are a class of ceramic compounds with general formula MFe_2O_4, where iron ions are in the trivalent oxidation state (Fe^{3+}) and M represents one or more divalent cation such as Fe^{2+}, Co^{2+}, Mn^{2+}, Zn^{2+}. These ferrites are typical spinel-type oxides with crystallographic structure, shown in Figure 4.1, belonging to the $Fd\overline{3}m$ space group. In particular, the unit cell contains 32 O^{2-} ions, which form a face-centred cubic (*fcc*) lattice, and divalent and trivalent cations occupy 16 of 32 octahedral (*Oh*) and 8 of 64 tetrahedral (*Td*) crystallographic cavities generated by the oxygen framework.

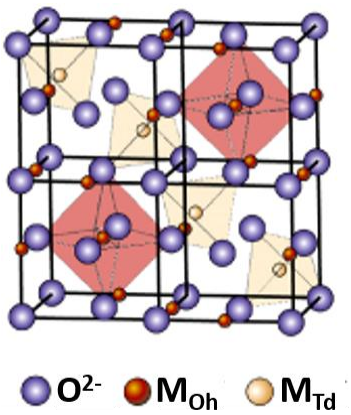

Figure 4.1: Schematic representation of the spinel crystallographic structure composed on *fcc* O^{2-} framework where metal ions occupy octahedral (M_{Oh}) an tetrahedral cavities (M_{Td}).

Depending on the ion distribution, ferrites are classified as:

- *normal spinel*. Trivalent ions occupy *Oh* sites while divalent ions are placed in the *Td* cavities;
- *inverse spinel*. Trivalent ions occupy both *Td* sites and half of the *Oh* ones while divalent ions are placed in the remaining *Oh* cavities;

- *partially inverted spinel*. Both trivalent and divalent ions occupy *Oh* and *Td* sites.

In order to take into account the different ion distribution, the general formula for ferrites can be expressed as $(M_{1-i}Fe_i)[M_iFe_{2-i}]O_4$, where parentheses, (), and brackets, [ ], are used to denote tetrahedral and octahedral sites, respectively; *i* is the inversion parameter that can vary from 0 (normal spinel) to 1 (inverse spinel). More in detail, in the case of transition metal cations the preferred site occupancy can be explained by the theory of Crystal Field Stabilisation Energy (*CFSE*), which predicts that a given geometry would be occupied by the cation with higher *stabilization energy*. Hence, if the trivalent cation has higher *CFSE* value in *Oh* site than the divalent cation, a normal spinel is expected. Conversely, an inverse spinel is formed when the divalent cation has higher *CFSE* value in *Oh* cavities than the trivalent one. Particularly, in the case of cobalt ferrites, being the oxide anion a weak ligand, a *high-spin* ground state is expected for Fe^{3+} ion (maximum spin multiplicity). Since high spin Fe^{3+} ions (d^5 electronic configuration) have lower *CFSE* in *Oh* than Co^{2+} (d^7 electronic configuration), Crystal Field Stabilisation Energy predicts $CoFe_2O_4$ would assume an inverse spinel structure. However, several experiments demonstrated that $CoFe_2O_4$ is a partially inverted spinel structure with cobalt atoms predominantly in the *Oh* sites (high degree of inversion). [1] In particular, inversion parameter ranging between i = 0.68 - 0.80 has been reported. [2,3]

From the magnetic point of view, ferrites are generally ferrimagnetic (FiM). In fact, the magnetic moment of the cations are parallel to those placed in sites with same geometry (e.g., *Oh-Oh and Td-Td*) and antiparallel to cations in cavities with different geometry (e.g., *Oh-Td*). Such orientation originates two sublattices of parallel magnetic moments (*Td* and *Oh* ones) which are antiferromagnetically coupled. However, in most of the cases, the magnetic moments of *Td* and *Oh* sublattices do not completely compensate, leading to a net magnetic moment of the material. Thus, even if sharing the same crystallographic and magnetic structures, the magnetic properties of spinel ferrites are strictly related to the nature of the divalent ions. Among various *light* transition metals, *high-spin* Co^{2+} ions in *Oh* sites exhibit both notable magnetocrystalline anisotropy (due to the high spin-orbit coupling arising from the partially unquenched orbital moment) and magnetization value (considerable spin and orbital moments). [4] Consequently, thanks to its high magnetic anisotropy cobalt ferrite is a suitable material for permanent magnet applications.

In this Chapter, the synthesis and the magnetic behaviour of cobalt ferrite nanoparticles are described. The primary goal of this investigation was that of identifying the optimal size and shape, which maximize the performance of this material as permanent magnet. In order to evaluate the magnetic properties evolution with particle size, narrow size distributed and highly crystalline systems with fixed stoichiometry ($Co_xFe_{3-x}O_4$, with x = 0.6-0.7) were been prepared. In particular, the x = 0.6-0.7 stoichiometry was chosen as it has been recently demonstrated it corresponds to the highest magnetic anisotropy among all non-stoichiometric cobalt ferrites. [5–7] This behaviour arises from a lower symmetry ground state because of the presence of both Fe^{2+} and Co^{2+} in the Oh cavities instead of only Co^{2+},

which causes a distortion of the ligand field. In addition, despite of the different Co^{2+} ions amount, non-stoichiometric cobalt ferrites maintain practically the same moderate magnetic moment typical of the stoichiometric compound $CoFe_2O_4$.

4.1 Synthesis and characterization of cobalt ferrite nanoparticles

Cobalt ferrite nanoparticles were synthesized through the thermal decomposition approach as it provides high control on particle size, size distribution, stoichiometry and crystallinity. However, despite of the large amount of scientific reports in the literature, thermal decomposition synthesis of cobalt ferrite nanoparticles has till now focused only on a narrow range of particle size, from 6 to 14 nm. [7–10] Therefore, since we were interested in investigating a much broader particle size range, maintaining under control their particle size distribution, stoichiometry and crystallinity, we could not rely on previous work. Therefore, we explored different modifications of the procedure by varying all the parameters involved, as nature of metal precursors, surfactants, heating rate and digestion time.

In particular, a family of cobalt ferrite nanoparticles with average size from 4 to 60 nm and with a narrow size distribution was synthesized by thermal decomposition of metal-organic precursors in high-boiling point solvents containing oleic acid (OA) and oleylamine (OAm) as stabilizing surfactants following a slightly modified procedure previously reported for the synthesis of iron-based cubic spinels, (MFe_2O_4). [9,11] In a typical synthesis 1 mmol of metal precursors (iron(III) acetylacetonate, $Fe(acac)_3$, and cobalt(II) acetylacetonate, $Co(acac)_2$, or cobalt(II) chloride, $CoCl_2$) in a Fe:Co molar ratio of 2:1 were dissolved in a solution containing 4 mmol of OA, 4 mmol of OAm and 50 mL of benzyl ether (Bz_2O) in a 100 mL three-neck round bottomed flask. Initially, the mixture was degassed by bubbling N_2 at 120°C for 30 min and then it was heated up to the desired decomposition temperature setting heating rate, nucleation step and digestion time in order to control the final particle size. During the heating and digestion processes the mixture was exposed to a N_2 flow. Finally, the flask was removed from the heating mantle and allowed cooling down under inert atmosphere. All nanoparticles were washed by several cycles of coagulation with ethanol, centrifugation at 5000 rpm, disposal of supernatant solution and re-dispersion in hexane. The obtainment of the target stoichiometry was verified through X-Ray Fluorescence (XRF) spectrometry which confirmed all the nanoparticles have the same composition, $Co_{0.6\text{-}0.7}Fe_{2.4\text{-}2.3}O_4$,.

Transmission Electron Microscopy (TEM) images were acquired in order to evaluate the correlation between synthetic parameters and the obtained nanoparticles. In particular, particle size was monitored through mean particle diameter ($\bar{d}$) and standard deviation (σ) obtained by calculating the number average by manually measuring the diameters length of >200 particles from TEM micrographs. Figure 4.2 shows some representative bright field,

low magnification TEM images of obtained cobalt ferrite nanoparticles and the corresponding particle size histograms. The different samples are labelled CFO#, where # represents the mean particles size.

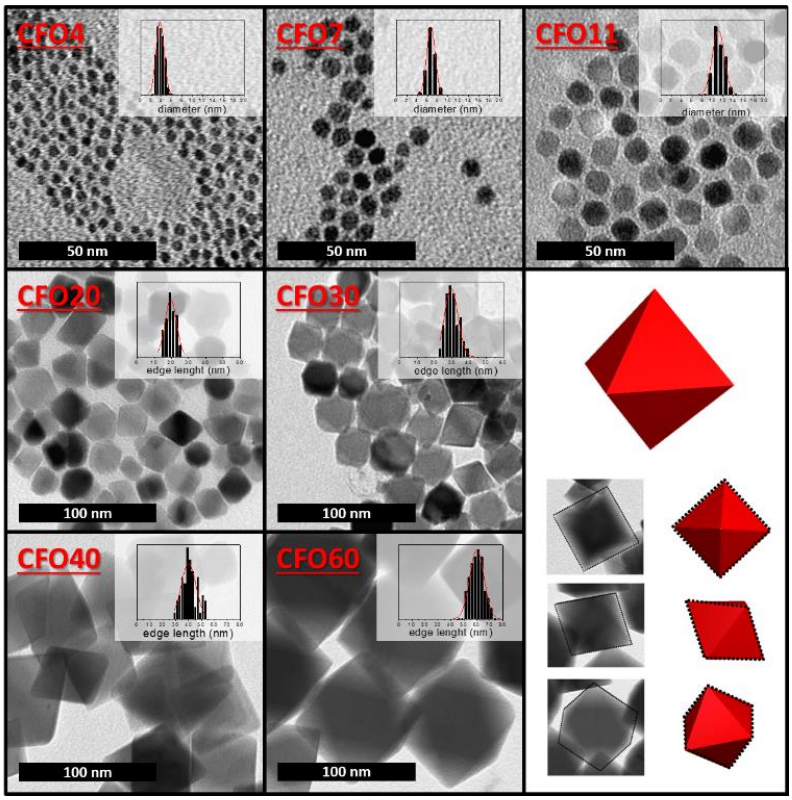

Figure 4.2: TEM images and particle size histograms for 4(1), 7(1), 11(1), 20(2), 30(4), 40(7) and 60(4) nm cobalt ferrite nanoparticle of. In the box, 2D TEM cubic, rombohedral and hexagonal projections for octahedral nanoparticles.

The control of the nanoparticles size was obtained by modifying the synthetic parameters related to the nucleation and growth processes (see Table 4.1). The smaller nanoparticles, with mean particle size from 4 to 11 nm, were synthesized by decomposition of $Fe(acac)_3$ and $Co(acac)_2$ using OA and OAm as surfactants, with the exception of 4 nm nanoparticles. Indeed, the latter were synthesized using only OAm as surfactant, following a slightly modified procedure already reported for the synthesis of MnO nanoparticles. [11] In fact, this choice reduces the probability of the $Fe^{2+} \rightarrow Fe^{3+}$ oxidation, which, as recently demonstrated by Fantechi *et al*., [7] is significantly large for small non-stoichiometric cobalt ferrite nanoparticles synthesized using OA and OAm surfactants, providing, as final product cobalt doped maghemite (γ-Fe_2O_3). The control of the mean particles size in this range was achieved by modifying the digestion time and the decomposition temperature. Low decomposition temperature (210 °C) leaded to small nanoparticles with an average diameter of 4(1) nm. It should be noted that, at this decomposition temperature, the

digestion time must be larger than 300 min in order to obtain crystalline nanoparticles. Conversely, increasing the decomposition temperature to 270 °C, adding a 2 hours nucleation step at 210 °C and shortening the digestion time from 300 min to 30 min or 60 min, nanoparticles with average diameter of 7(1) and 11(1) nm, respectively, were obtained. TEM images show that small nanoparticles exhibit a spherical shape. All the size histograms obtained from TEM micrographs by evaluating the particle diameter, *d*, can be well fitted by a Gaussian distribution, showing unique size population with a narrowly distributed diameter (deviation < 20%).

Larger nanoparticles with mean edge length from 20 to 60 nm were synthesized using anhydrous $CoCl_2$ as cobalt precursor. Different particle sizes were obtained controlling the digestion time and heating rate and keeping the decomposition temperature constant. A fast heating rate (3 °C/min) permitted the synthesis of 20 to 30 nm nanoparticles. On the other hand, a slow heating rate (1 °C/min) favoured the formation of larger nanoparticles in the 40 to 60 nm range. For a given heating rate, the particle size could be further tuned by varying the digestion time from 15 to 60 minutes.

Interestingly, TEM images demonstrated that on increasing the nanoparticles size the shape evolves from sphere to octahedron, passing through an intermediate size around 20 nm, where spheres and cubes coexist. In Figure 4.2 the cubic, rhombohedral and hexagonal 2D projections along [100], [110] and [111] directions of a regular octahedron/truncated octahedron placed over {111} or {100} faces is shown together with the corresponding TEM images. [12] The particle size histograms for non-spherical nanoparticles, also reported in Figure 4.2, are referred to the average edge length of cubes or octahedrons (*l*). In addition, the formation of octahedral nanoparticles at large size was confirmed by helium ion microscopy, (HIM), as shown in Figures 4.3, where images of 20 and 40 nm nanoparticles are shown.

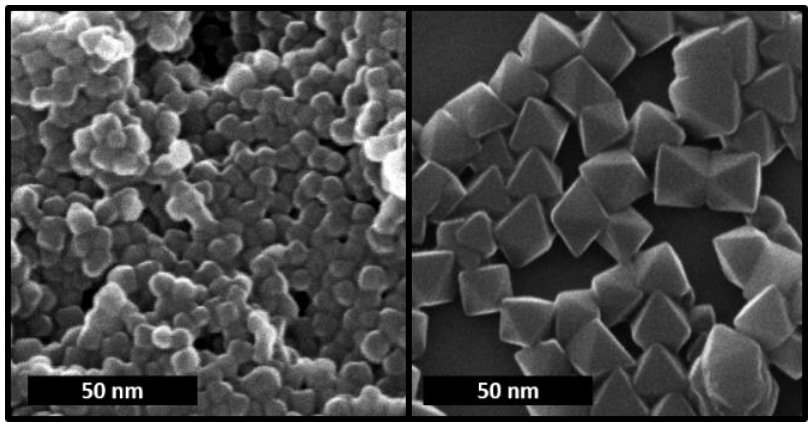

Figure 4.3: (*From the left)* HIM images of 20(2) and 40(7) nm cobalt ferrite nanoparticles showing cubic and octahedral shape, respectively.

Theoretically, cubic spinel structures should generate a cubic crystal habit, reflecting the growth along the preferential <100> axes, but our experimental result suggests that with our synthetic procedure, spherical and octahedral shapes are the most favoured, depending on the size. For small nanoparticles the dominant role of surface tension drives the nanocrystal growth towards a spherical shape, which corresponds to the smallest surface area. Conversely, when the particle size is increased, the change in the shape from spheres to octahedrons is due to the faster growth rate along the <100> directions with respect to <111>, being {111} lowest energy facets. [13] Interestingly, nanoparticles with size close to the threshold between the two morphologies (20 nm), where surface tension and preferential <100> directions growth are balanced, exhibit a cubic shape.

In order to verify the formation of crystalline cobalt ferrite nanoparticles, powder X-Ray Diffraction (XRD) patterns were recorded for the family of cobalt ferrite nanoparticles. As shown in Figure 4.4, all diffraction patterns show the formation of a single crystallographic phase, which can be indexed as the cubic structure of spinel oxides (JCPDS PDF #221086). The series of diffractograms reveals the expected gradual narrowing of the peaks associated with the increase of the particles size. The crystal size, evaluated from the diffraction patterns are consistent with those obtained from TEM images, indicating the growth of single crystal nanoparticles and their high crystallinity.

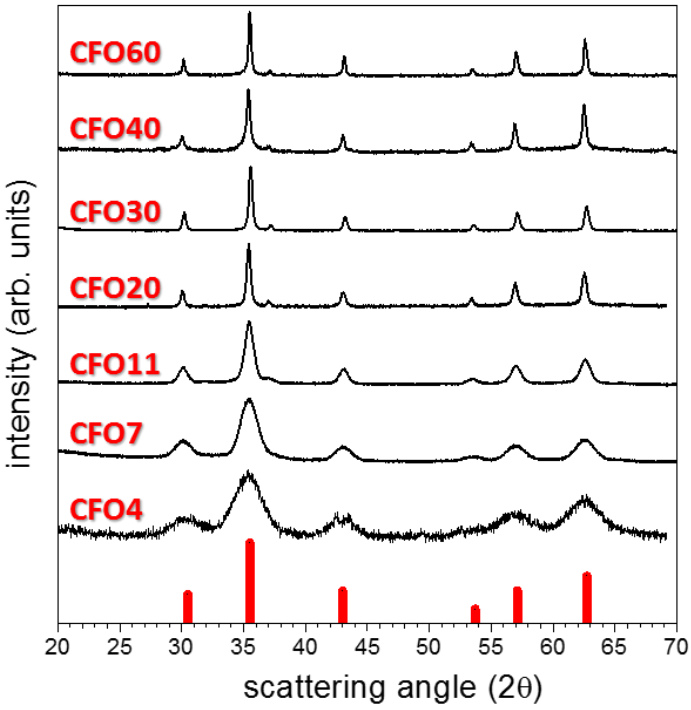

Figure 4.4: XRD patterns of the family of cobalt ferrite nanoparticles. In red is reported the reference pattern corresponding to the spinel *fcc* structure for $CoFe_2O_4$ *JCPDS PDF #221086*.

In addition, cell parameter and crystallographic strain were determined and are reported in Figure 4.5. The cell parameter for the whole series of cobalt ferrite nanoparticles is constant and close to 0.840 nm. This fact supports the similar stoichiometry of all the synthesized nanoparticles, as indeed indicated by XRF analysis. However, this value is slightly larger than that reported for Co-doped maghemite nanoparticles with similar stoichiometry [7] suggesting the stabilization, even at small size, of a pure cobalt doped magnetite phase (Fe_3O_4, Fe^{2+}/Fe^{3+} oxide) where oxidation of Fe^{2+} ions did not take place. The evaluated microstrain is highest at the smallest crystallite size and then it decreases on increasing particles size, vanishing, in the resolution limit of our experimental device, for size ≥ 20 nm. Interestingly, the structural distortions disappear at the same size at which the morphology of the nanoparticles changes, suggesting that finite-size and surface effects can induce surface strain and concomitant structural perturbations leading to preferential morphological structures. [14] These results demonstrate the intimate correlations between particle morphology, crystal structure and particle size existing at the nanoscale.

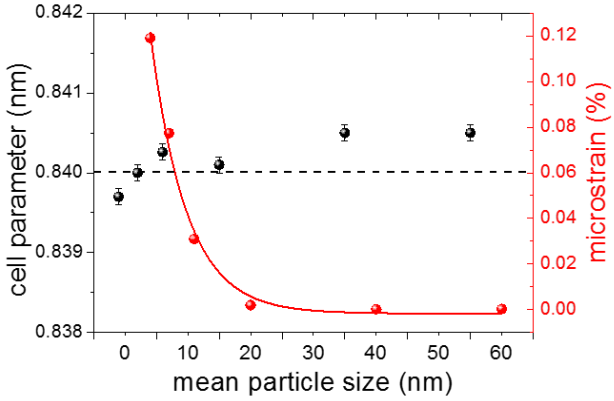

Figure 4.5: Cell parameter (black) and microstrain (red) dependence on particle size.

Table 4.1: Summary of the synthesis parameters and structural data obtained from TEM, XRD and XRF analysis for the family of samples.

	cobalt precursor	surfa-ctants	digestion tempera-ture (°C)	digesti on time (min)	heating rate (°Cmin^{-1})	TEM size (nm)	XRF (x)	XRD size (nm)	cell parameter (nm)
CFO4	$Co(acac)_2$	OAm	210	300	18	4(1)[d]	0.7	4	0.839(1)
CFO7	$Co(acac)_2$	OA/OAm	300	30	3	7(1) [d]	0.7	8.8	0.840(1)
CFO11	$Co(acac)_2$	OA/OAm	300	60	3	11(1) [d]	0.7	16	0.840(1)
CFO20	$CoCl_2$	OA/OAm	270	15	3	20(2) [l]	0.6	30	0.842(1)
CFO30	$CoCl_2$	OA/OAm	270	60	3	30(4) [l]	0.7	35	0.840(1)
CFO40	$CoCl_2$	OA/OAm	270	15	1	40(7) [l]	0.6	50	0.841(1)
CFO60	$CoCl_2$	OA/OAm	370	60	1	60(4) [l]	0.6	80	0.840(1)

4.2 Magnetic properties of cobalt ferrite nanoparticles

In order to evaluate the magnetic behaviour dependence on the mean particle size, a deep analysis of the static magnetic properties was performed by standard magnetometric techniques. In particular, magnetic properties of the nanoparticles were measured on tightly randomly packed powder samples using a vibrating sample magnetometer (VSM). In this section, both magnetization (*M*) dependence with temperature (*T*) and applied field (*H*) for the family of cobalt ferrite nanoparticle is reported.

At first, the temperature dependence of the magnetization was investigated after zero field cooling (*ZFC*) and field cooling (*FC*) procedures in the presence of a 50 Oe applied field (see Figure 4.6). For each particle size, ZFC-FC curves show the characteristic behaviour of an ensemble of single-domain nanoparticles.

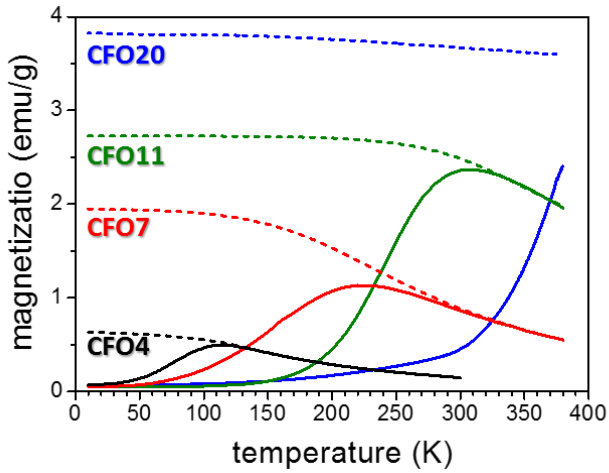

Figure 4.6: Temperature dependence of the ZFC (solid line) and FC (dotted line) magnetization curves recorded at 50 Oe for 4 (black), 7 (red), 11 (green) and 20 nm (blue) cobalt ferrite nanoparticles.

In particular, ZFC curves of nanoparticles smaller than 20 nm present a maximum at a given temperature, T_{max}, lower or close to room temperature. At higher temperatures the ZFC and FC curves merge and magnetization values decay as the temperature increases. These features are characteristic of the progressive thermally activated unblocking of an assembly of single domain nanoparticle. transition to the superparamagnetic state above which nanoparticles are *unblocked.* As a first approximation, T_{max} can be identified with the *blocking temperature*, T_B, of the system. Above T_{max} the particles are in the superparamagnetic state, while below they are blocked. Conversely, larger nanoparticles (as shown for 20 nm nanoparticles) are still in the *blocked* state at room temperature, as required for the realization of permanent magnets.

The T_B dependence on the mean particle size is reported in Figure 4.7. For nanoparticle ≥20 nm, whose thermal deblocking at the time scale of standard static magnetometric techniques, requires temperatures higher than that experimentally investigated, T_B was estimated from the hysteresis loops recorded at various temperatures, using the Stoner-Wohlfarth equation: [15–17]

$$H_C = H_C(0)\left[1 - \frac{T}{T_B}\right]^{\beta} \qquad 4.1$$

where $H_C(0)$ is the anisotropy field and β is an exponential factor which is 0.5 or 0.77 for oriented or randomly oriented assembly of particles, respectively. [18–20] Interestingly, extending this procedure to smaller nanoparticles provides T_B values that well match those extracted from ZFC magnetization curves, supporting the validity of this approach.

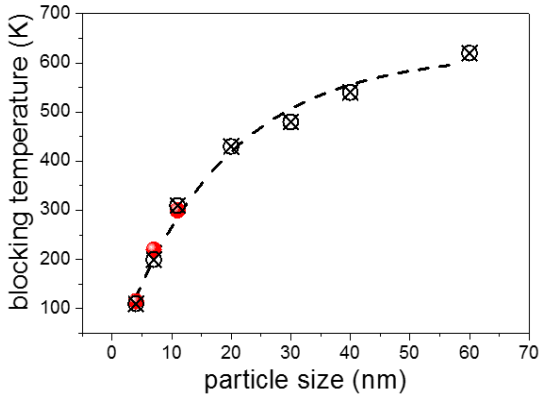

Figure 4.7: Size dependence of the blocking temperature. T_B values were obtained by ZFC curves (solid red spheres) or by fitting H_C dependence with T using the Stoner-Wohlfarth Equation 4.1 (empty black circles with crosses).

As expected, T_B increases with the mean particle size (see Table 4.5). However, it has to be pointed out that T_B is not directly proportional to the volume of the nanoparticles, as predicted from the classical description for superparamagnetism ($T_B \propto K_{eff}V$, where K_{eff} is the *effective magnetic anisotropy*). [21] Such deviation may be taken as an indication that K_{eff} itself has evolves with the size of the nanoparticles (see discussion in the following section for data and details).

Hysteresis loops for the family of cobalt ferrite nanoparticles were recorded at different temperatures in the range from 5 to 380 K. As reported in Figure 4.8-a, hysteresis loops recorded at low temperature (5 K), i.e. where thermal demagnetization processes are negligible for all particle size, exhibit the characteristic features expected for hard ferro- or ferri-magnetic materials (nonzero M_R and high H_C). Conversely, room temperature (300 K) hysteresis loops reported in Figure 4.8-b, show that only nanoparticles larger than 20 nm maintain the ferromagnetic behaviour, acting thus as permanent magnets, while smaller

nanoparticles exhibit the typical features of the superparamagnetic state (zero M_R and H_C and Langevin-like M vs. H dependence).

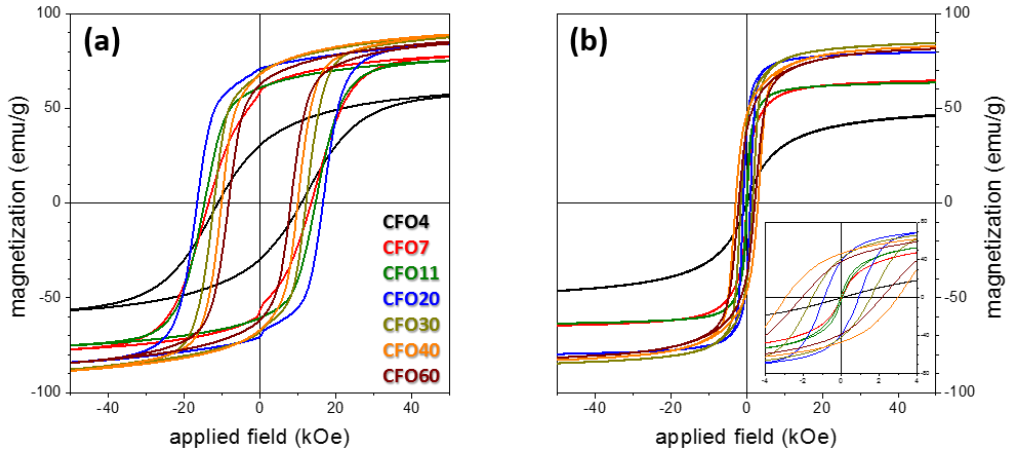

Figure 4.8: *(From the left)* Low temperature (5 K) and room temperature (300 K) hysteresis loops of the family of cobalt ferrite nanoparticles. In the inset the enlargement of the low field region is shown.

Coercive field, (H_C), saturation magnetization, (M_S) and reduced remanence, ($R = M_R/M_S$, where M_R is the remnant magnetization) for each particle size were extracted from recorded hysteresis loops (see Table 4.2 summarizing low temperature magnetic properties). In addition, H_C, M_S and R were analysed as a function of the mean particle size (see Figure 4.9).

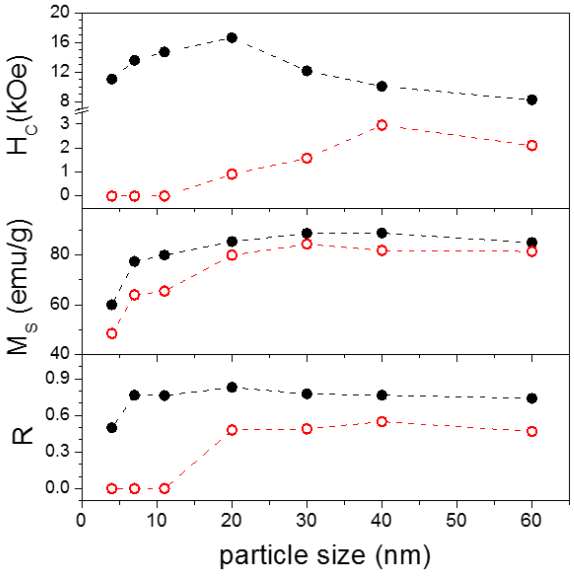

Figure 4.9: *(From the top)* Size dependence of H_C, M_S, and R measured at 5K (full black dots) and 300 K (empty red dots).

Interestingly, a non-monotonous dependence of H_C with particle size was observed: initially H_C increases until it reaches the maximum value of 16.7 kOe for 20 nm of particle size, which is followed by a fast abatement for larger particles sizes. A similar size-dependence of H_C is retained at room temperature although some differences are observed: indeed, due to the increased relevance of thermal demagnetization processes, the maximum H_C value is decreased to 3 kOe and shifted to larger particles size (40 nm). The non-monotonic H_C dependence at low temperature can result from a crossover in the magnetization switching mode and/or a shape-induced demagnetization effect. In other words, initially, H_C increases with the size as expected for single domain nanoparticles, where the magnetization reverses its orientation through a uniform coherent rotation of all the atomic spins. [22–25] However, according to micromagnetic theory, curling (non-coherent) rotation becomes favoured with respect to the coherent reversal mode when the radius of a particle surpasses a certain limit, called coherent radius (r_{coh}). For small spherical nanoparticles:

$$r_{coh} = \sqrt{24} l_{ex} \qquad 4.2$$

where l_{ex} is the *exchange length*, which reflects the competition of exchange and dipolar interactions and can be expressed as:

$$l_{ex} = \sqrt{\frac{A}{\mu_0 M_S^2}} \qquad 4.3$$

being A the *exchange stiffness constant* and μ_0 the *vacuum permeability*. [26–28] In particular, using the intrinsic magnetic properties of bulk cobalt ferrite, $l_{ex} \approx 5.35$ nm can be estimated from which $r_{coh} \approx 17$ nm. [29] According to this value, cobalt ferrite nanoparticles with size larger than 35 nm should show a crossover on the magnetization reversal process from coherent to incoherent mode (curling), decreasing H_C as the particle size is further increased. [29,30] Interestingly, this value matches the diagonal of 20 nm cubic nanoparticles. Moreover, a concomitant effect of the variation of the particle shape can also be envisaged. Indeed, nanoparticles with small and intermediate size mostly have regular spherical or mixed spherical/cubic shapes. However, in larger nanoparticles, where the octahedron emerges as the preferential crystal habit, the demagnetization fields are preferentially generated at the corners regions, where incoherent rotation modes can be generated more easily as the particle size becomes larger, leading to a decrease of H_C. [31] It should be noted that a change in the shape may also affect the total magnetic anisotropy of the nanoparticles through the surface contribution. [24,25] However, in our case, the high magnetocrystalline anisotropy of cobalt ferrite and the large particle size make this contribution negligible. It has to be noted that a non-monotonous behaviour at room temperature was previously observed in a similar range of particle sizes for cobalt-ferrite nanoparticles synthesized by various techniques and was ascribed to the magnetic single- to multi-domain transition. [32–34] Conversely, we do believe that this behaviour originates from the combination of a crossover on magnetic rotation and/or demagnetization shape-induced effect, which are responsible for the maximum at low temperature, and thermal

fluctuation of the blocked moment across the anisotropy barrier. The latter, being more important for lower sizes and at higher temperatures, produces a shift to large particle size of the H_C maximum. [35]

On the other hand, M_S and R show the same trend both at low and room temperature, increasing with the average particle size up to 20 nm and then remaining roughly constant as particle size is further increased, at M_S = 80–90 emu/g, R = 0.75–0.83 and M_S =80–85 emu/g, R = 0.5 for low and room temperature, respectively (see Table 4.2). Low temperature data are in good agreement with those theoretically expected for randomly oriented cobalt ferrite nanograins with cubic magnetic anisotropy, while the room temperature ones, due to thermal effects, show a more pronounced increase with size for both M_S and R. In addition, it has to be noted that larger nanoparticles (≥20 nm) presents notably large M_S value both at low and room temperature, similar to those of bulk cobalt ferrite. Such values, which are not obvious in nanostructured systems, are a direct evidence of the high crystallinity of the systems, previously observed. [36,37] On the other hand, 4 nm nanoparticles present peculiar magnetic properties with respect to the rest of the series. At low temperature, we observed a 25% reduction of M_S, while R is only 0.6. These results indicate that for particles size <20 nm (see Figure 4.12) the magnetic disorder induced by large structural strain deteriorates the magnetic properties. In addition, for very small nanoparticles a symmetry change of the magnetic anisotropy from cubic to uniaxial may concur to lower R. [37–39]

In order to further investigate the magnetic properties of the series of samples, the *effective magnetic anisotropy* (K_{eff}) was estimated from the temperature dependence of H_C. Assuming the magnetic anisotropy is temperature-independent and the magnetization reversal driven by a coherent rotation, the effective cubic magnetic anisotropy can be expressed as:

$$K_{eff} = \frac{H_C(0) M_S}{0.64} \qquad 4.4$$

where $H_C(0)$ values were obtained for each particles size from the analysis of the temperature-dependence of the coercive field following the Equation 4.1. In Figure 4.10, K_{eff} estimated from the hysteresis loops recorded at various temperature in the range from 5 to 380 K and neglecting the contribution from unblocked nanoparticles is shown.

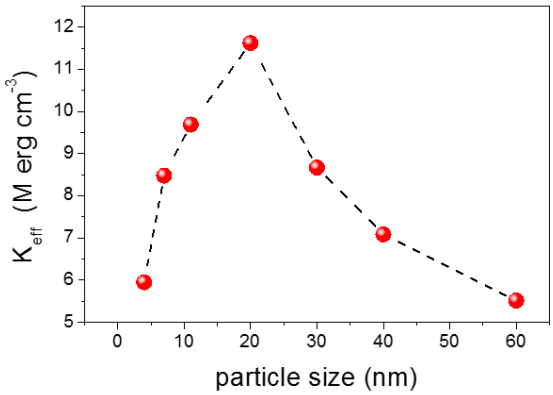

Figure 4.10: Evolution of K_{eff}, of cobalt ferrite nanoparticles with particle size. The data were obtained from hysteresis loops at variable temperature neglecting any temperature-dependent term and assuming only coherent rotation switching mode.

It emerges that K_{eff} follows the same non-monotonic dependence on particle size observed at low temperature for H_C. Moreover, it has to be noted that the whole series of cobalt-ferrite nanoparticles presents K_{eff} values in the same range of bulk stoichiometric cobalt ferrite, $CoFe_2O_4$, ($K_{eff} \approx 19 \cdot 10^6$ ergcm^{-3}), [40] the largest estimated value being $11.5 \cdot 10^6$ ergcm^{-3} for 20 nm nanoparticles (see Table 4.5). Notably, not exceeding the bulk value as often observed for very small nanoparticles, estimated K_{eff} values suggest in our case the surface contribution does not significantly modify the effective magnetic anisotropy.

Table 4.2: Magnetic properties of cobalt ferrite nanoparticles with different average size.

	TEM size (nm)	T_B^{exptl} (K)	T_B^{calcd} (K)	H_C^{5K} (kOe)	M_S^{5K} (emug^{-1})	R^{5K} (M_R/M_S)	$H_c(0)$ (kOe)	β	K_{eff} (Mergcm^{-3})
CFO4	4(1)[d]	115	110	11.0	59.4	0.51	12.7	3.3	6.0
CFO7	7(1)[d]	220	200	13.5	77.4	0.76	14.0	1.9	8.5
CFO11	11(1)[d]	300	310	14.7	80.4	0.76	15.5	1.8	9.7
CFO20	20(2)[l]	-	430	16.7	85.5	0.83	17.4	2.0	11.6
CFO30	30(4)[l]	-	480	12.1	89.1	0.77	12.5	2.0	8.7
CFO40	40(7)[l]	-	540	10.0	88.7	0.77	10.2	1.5	7.0
CFO60	60(4)[l]	-	620	8.0	84.7	0.74	8.3	1.4	5.0

In addition, the temperature evolution of the magnetic properties of the family of cobalt ferrite nanoparticles was investigated: by plotting H_C and R as a function of normalized temperature T/T_B a decrease in both H_C and R can be observed as temperature increases, vanishing for $T = T_B$.

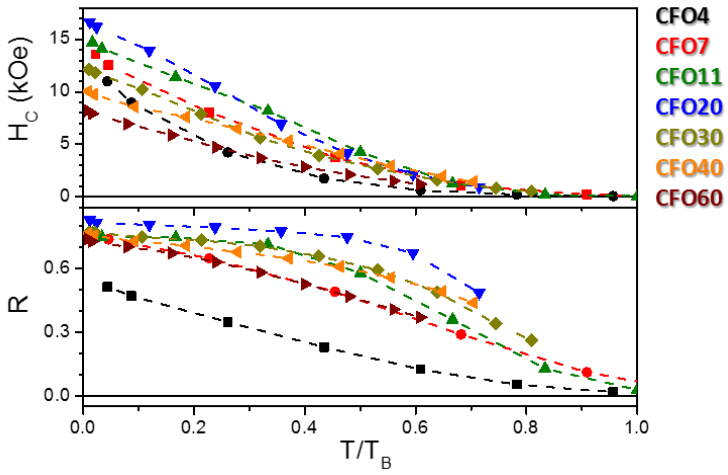

Figure 4.11: *(From the top)* Evolution of H_C and R for the series of cobalt ferrite nanoparticles as a function of T/T_B.

With respect to the R decay, different temperature dependencies are clearly observed: for small nanoparticles (4 and 7 nm), R decays almost linearly, while for the intermediate size (from 10 to 40 nm) a plateau can be observed at low temperatures, which shifts the linear decay to high T/T_B values. Then, for larger nanoparticles (60 nm) a linear decrease similar to that observed for small nanoparticles is restored. On the contrary, H_C shows a constant decay for all particle size as T/T_B increases, although a change in the curvature occurs within the series, being convex for smaller and larger nanoparticles and almost linear for intermediate particle sizes. In addition, the fit of the H_C vs T/T_B curves using the Stoner–Wohlfarth model provided β factors (reported in Table 4.5) much larger than that theoretically predicted (0.5 or 0.77), indicating a stronger variation of H_C as a function of the temperature. This discrepancy can be ascribed to the change of the intrinsic magnetic anisotropy upon varying temperature, which so far was not taken into account. Such evolution is expected to vary with the particle size and shapes. [41] Moreover, the effect of inter-particle interactions can contribute to the observed behaviour as well. [21] Besides, both effects are strongly correlated with the trend of K_{eff}: that is, nanoparticles with higher K_{eff} present lower thermal fluctuations as the temperature increases, and thus, different variation of the magnetic anisotropy occurs with the temperature.

In order to corroborate the obtained values, K_{eff} for small cobalt ferrite nanoparticles (<20 nm) was evaluated also from AC susceptibility measurements. In particular, AC susceptibility was measured at different temperatures, in the range between 10 and 350 K, and log-spaced frequencies in the range between 1 and 1000 Hz using a SQUID magnetometer (Quantum Design). Due to the limited range of accessible temperatures, only the three smallest samples (4, 7 and 11 nm) could be analysed by this technique. The temperature dependence of the in-phase (χ') and out-of-phase (χ'') components of the

magnetic susceptibility for the five investigated frequencies is shown in Figure 4.12 for CFO4, CFO7 and CFO11.

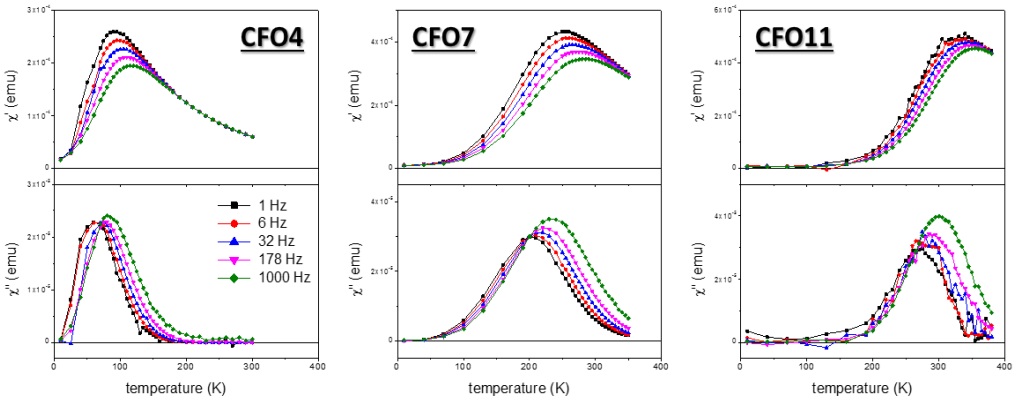

Figure 4.12: *(From the left)* Temperature dependence of the in-phase (χ') and out-of-phase (χ'') components of the AC susceptibility measured for 4, 7 and 11 nm cobalt ferrite nanoparticles.

For all samples the characteristic thermal dependence of slow relaxing single domain magnetic nanoparticles is observed, as clearly demonstrated by the presence of a peak in both the real and imaginary components, which shifts to higher temperature with increasing the measuring frequency (ν). Information about the relaxation dynamics were extracted by assuming that the maximum of χ'', corresponds to the T_B, i.e. the temperature at which the characteristic relaxation time equals the experimental observation time ($\tau_\omega = 1/2\pi\nu$). According to the Néel model, previously described in Chapter 2, in non-interacting superparamagnetic systems the curve of $ln\tau_\omega$ vs. $1/T_B^\omega$ must be a straight line, whose slope and intercept directly provide an estimate of the parameters determining the relaxation dynamics (Arrhenius law):

$$ln\tau_\omega = ln\tau_0 + \frac{K_{eff}V}{k_B T_B^\omega} \qquad 4.5$$

where τ_0 is the attempt time and k_B is the Boltzmann constant. In figure 4.13 the $ln\tau_\omega$ vs. $1/T_B^\omega$ data collected for the three samples are shown, together with the corresponding fits to the Arrhenius law, while the best fit parameters obtained are listed in Table 4.3.

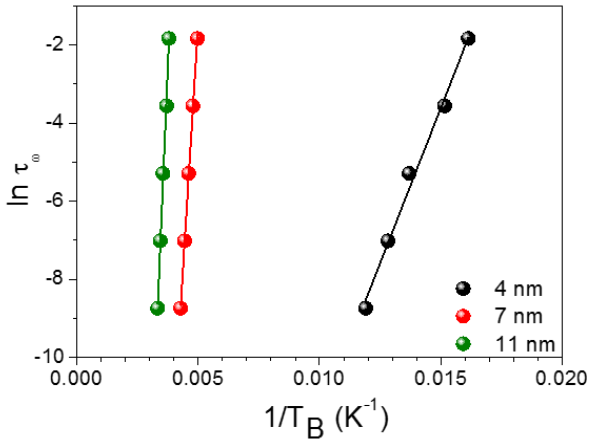

Figure 4.13: $ln\tau_\omega$ vs. $1/T_B{}^\omega$ curves for 4, 7 and 11 nm cobalt ferrite nanoparticles. The straight lines represent the best fit to the Arrhenius low (Equation 4.6)

The attempt time, τ_0 is found to decrease with increasing the size. However, while for the smallest sample it falls within the range commonly assumed for not-interacting magnetic nanoparticles (10^{-8}-10^{-13}), it is much smaller for larger nanoparticles, pointing out that, for these samples, the relaxation dynamics can be no more described by the simple Néel model due to the presence of not negligible dipole-dipole interactions. For these samples, a fit using one of the models typically used for interacting nano-clusters (Vogel-Fulcher or critical scaling law) would be more appropriate. However, in our case, due to the low number of experimental data (too low data/fitting parameters ratio) no attempts using these models could be made.

The K_{eff} values can be extracted from the average energy barriers considering the samples as made up of spherical particles of average diameter equal to those estimated by TEM analysis. The as obtained values are reported in Table 5.6. A very good match with the values obtained from the analysis of the hysteresis loops at low temperature is observed for 4 and 7 nm samples. Conversely, for the 11 nm sample dipolar interactions are too strong to get a reliable anisotropy energy density value.

Table 4.3: Best fit parameters (τ_0, $E_a/k_B = K_{eff}V/k_B$), and effective magnetic anisotropy obtained from AC and hysteresis loops measurements ($K_{eff}{}^{AC}$ and $K_{eff}{}^{HL}$) for smaller nanoparticles.

	τ_0 (s)	$K_{eff}V/k_B$ (K)	$K_{eff}{}^{AC}$ (Mergcm^{-3})	$K_{eff}{}^{HL}$ (Mergcm^{-3})
CFO4	$1.3\cdot10^{-12}$	1590	6.5	6.0
CFO7	$3.5\cdot10^{-23}$	10000	8.0	8.5
CFO11	$7.9\cdot10^{-26}$	14700	3.7	9.7

In order to quantify the performance as permanent magnets of the family of cobalt ferrite nanoparticles, we evaluated the maximum energy product, $(BH)_{max}$, at low (5 K) and room temperature. As reported in Figure 4.14, $(BH)_{max}$ shows a non-monotonous dependence with particle size. In particular, the maximum values we found were 5.4 and 2.1 MGOe (43 and 18 kJm^{-3}) at low and room temperature, respectively.

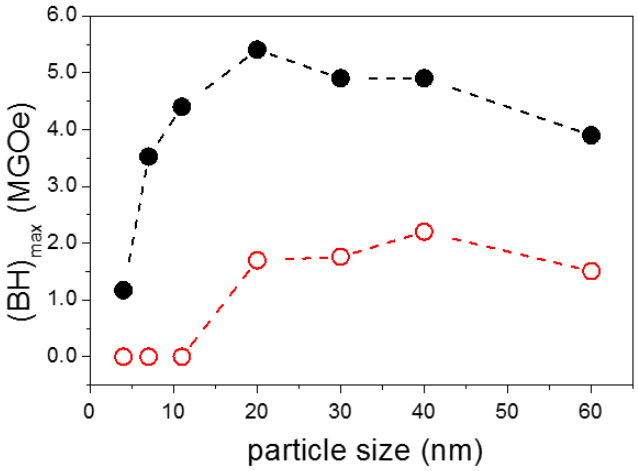

Figure 4.14: $(BH)_{max}$ at 5 (black solid circles) and 300 K (red empty circles) as a function of the particle size.

Interestingly, $(BH)_{max}$ shows the same size dependence of H_C, with maxima at 20 and 40 nm for low and RT, respectively, confirming the strong relationship existing between the two parameters. It has to be noted that, to our knowledge, the $(BH)_{max}$ product found at room temperature largely exceeds the values previously reported for cobalt ferrite fine particles (from 0.5 up to 1.1 MGOe), [34,42] although larger H_C were obtained. [34,43] This result can be ascribed to the large magnetic moment of our samples. For highly anisotropic material fulfilling the condition $H_C \geq 2\pi M_S$, it is theoretically predicted that $(BH)_{max}$ depends only on M_S and R, being the limiting condition: [22,44]

$$(BH)_{max} \leq (2\pi M_S)^2 \qquad 4.6$$

In our case, as it is shown in Figure 4.15, for 40 nm cobalt-ferrite nanoparticles $\mu_0 H_C$ is 3000 G, larger than $2\pi M_S$ (2500 G).

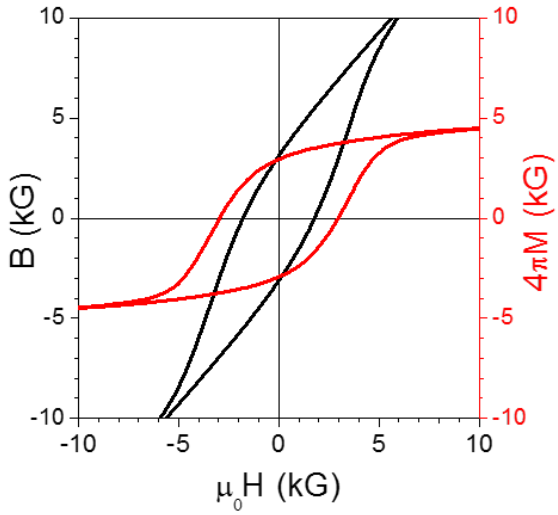

Figure 4.15: $4\pi M$ (red) and $B = H + 4\pi M$ (black) vs H loops for CFO40 at room temperature.

Therefore, we can conclude that for coercivities as those commonly observed for cobalt ferrite particles with size in the range of tens of nanometres, only large M_S, as is the case of the samples here presented, can efficiently further increase the $(BH)_{max}$ product. On the other hand, if we assume a complete orientation of the nanoparticles easy axes (i.e., a square hysteresis loops) and bulk density, a magnet obtained by compacting our 40 nm cobalt ferrite nanoparticles, could theoretically reach a $(BH)_{max}$ product of 8 MGOe (60 kJm^{-3}). This value largely surpasses the $(BH)_{max}$ of hard magnetic ferrites nowadays commercially available (4 MGOe, 30 kJm^{-3}). [45] Therefore, cobalt ferrite nanoparticles, such as those here presented, can be realistically considered as a promising material to replace rare-earth based compounds, at least for all those applications which do not require extraordinarily high magnetic performances.

4.3 Conclusion

In conclusion, in order to investigate the size-dependence of magnetic properties of nano-sized cobalt ferrite, a family of nanoparticles covering a range of mean particle size from 4 to 60 nm, with narrow size distribution, high crystallinity and controlled stoichiometry, were synthesized through OA and OAm assisted thermal decomposition. Different particles size were achieved varying synthetic parameters (metal precursor, heating rate and digestion time). From the magnetic point of view, we found cobalt ferrite nanoparticles present almost constant values of M_S and M_R with the exception of smaller nanoparticles because of the structural strain affecting the final magnetic properties. In addition, for particle size ≥20 nm large magnetic moments (similar to bulk cobalt ferrite) were observed thanks to the high crystallinity of the systems. On the other hand, H_C and K_{eff} depict a non-monotonic

behaviour with two different maxima at low and room temperature. We explained the observed behaviour as originating from a combination of crossover on magnetic coherent/non-coherent rotation and/or shape induced demagnetization effect, which are responsible for the maximum at low temperature, and thermal fluctuations of the blocked moment across the anisotropy energy barrier. Because the latter are more important at lower sizes and higher temperatures, the H_C maximum shifts to larger particle size at room temperature. In order to assess the suitability of these cobalt ferrite nanoparticles as permanent magnet, the $(BH)_{max}$ energy product was evaluated. Interestingly, we found the maximum value ever reported in the literature for cobalt ferrite nanoparticles at room temperature, i.e. 2.1 MGOe (18 kJm^{-3}) for 40 nm average size. Moreover, this investigation allowed us to establish, at least on the basis of $(BH)_{max}$, the potentiality of cobalt-ferrite nanoparticles for the realization of rare-earth free permanent magnet. Indeed, if the possibility of orienting the magnetic anisotropy axes of the nanograins is taken into account, $(BH)_{max}$ as large as 8 MGOe (60 kJm^{-3}) can be in principle obtained, which is close to double the values nowadays achievable from transition metal based ferrites (35 kJm^{-3}). Furthermore, by playing with the many parameters that define the physical properties of matter at the nanoscale, a further improvement of $(BH)_{max}$ can be envisaged. To this aim several strategies can be considered, such as increasing the particle magnetic moment through the control of the inversion degree of Co^{2+} ions in the spinel lattice, or by doping the spinel structure with diamagnetic divalent ions, such as Zn^{2+}. In addition, in order to retain the condition $H_C \geq 2\pi M_S$, the magnetic anisotropy must also be increased, a task which can be realized by modifying the shape and the surface or inducing stresses. On the other hand, the presented nanoparticles can also be considered as an excellent building block to design exchange coupled systems with enhanced energy product, [46] an approach which will be more extensively discussed in the next chapter. To conclude, all the above considerations suggest that cobalt-ferrite nanoparticles may be a viable alternative to replace rare-earth based permanent magnet, at least in the intermediate region of the energy product map, where the latter are currently employed simply because standard ferrites do not have large enough $(BH)_{max}$.

References

[1] A.S. Vaingankar, B. V Khasbardar, R.N. Patil, X-ray spectroscopic study of cobalt ferrite, J. Phys. F Met. Phys. 10 (1980) 1615–1619. doi:10.1088/0305-4608/10/7/027.

[2] D. Carta, M.F. Casula, A. Falqui, D. Loche, G. Mountjoy, C. Sangregorio, et al., A Structural and Magnetic Investigation of the Inversion Degree in Ferrite Nanocrystals MFe2O4 (M = Mn, Co, Ni), J. Phys. Chem. C. 113 (2009) 8606–8615. doi:10.1021/jp901077c.

[3] D. Carta, G. Mountjoy, G. Navarra, M.F. Casula, D. Loche, S. Marras, et al., X-ray Absorption Investigation of the Formation of Cobalt Ferrite Nanoparticles in an Aerogel Silica Matrix, J. Phys. Chem. C. 111 (2007) 6308–6317. doi:10.1021/jp0708805.

[4] R.L. Carlin, Magnetochemistry, First Ed., Springer Berlin Heidelberg, Berlin, Heidelberg, 1986. doi:10.1007/978-3-642-70733-9.

[5] J.C. Slonczewski, Origin of Magnetic Anisotropy in Cobalt-Substituted Magnetite, Phys. Rev. 110 (1958) 1341–1348. doi:10.1103/PhysRev.110.1341.

[6] M. Tachiki, Origin of the Magnetic Anisotropy Energy of Cobalt Ferrite, Prog. Theor. Phys. 23 (1960) 1055–1072. doi:10.1143/PTP.23.1055.

[7] E. Fantechi, G. Campo, D. Carta, A. Corrias, C. de Julián Fernández, D. Gatteschi, et al., Exploring the Effect of Co Doping in Fine Maghemite Nanoparticles, J. Phys. Chem. C. 116 (2012) 8261–8270. doi:10.1021/jp300806j.

[8] C. a. Crouse, A.R. Barron, Reagent control over the size, uniformity, and composition of Co–Fe–O nanoparticles, J. Mater. Chem. 18 (2008) 4146. doi:10.1039/b806686h.

[9] S. Sun, H. Zeng, D.B. Robinson, S. Raoux, P.M. Rice, S.X. Wang, et al., Monodisperse MFe2O4 (M = Fe, Co, Mn) nanoparticles., J. Am. Chem. Soc. 126 (2004) 273–9. doi:10.1021/ja0380852.

[10] V.L. Calero-ddelc, A.M. Gonzalez, C. Rinaldi, A Statistical Analysis to Control the Growth of Cobalt Ferrite Nanoparticles Synthesized by the Thermodecomposition Method, J. Manuf. Sci. Eng. 132 (2010) 030914. doi:10.1115/1.4001717.

[11] W.S. Seo, H.H. Jo, K. Lee, B. Kim, S.J. Oh, J.T. Park, Size-dependent magnetic properties of colloidal Mn3O4 and MnO nanoparticles., Angew. Chem. Int. Ed. Engl. 43 (2004) 1115–7. doi:10.1002/anie.200352400.

[12] A.L. Lopes-Moriyama, V. Madigou, C.P. de Souza, C. Leroux, Controlled synthesis of CoFe2O4 nano-octahedra, Powder Technol. 256 (2014) 482–489. doi:10.1016/j.powtec.2014.01.080.

[13] Z.L. Wang, X. Feng, Polyhedral Shapes of CeO2 Nanoparticles, J. Phys. Chem. B. 107 (2003) 13563–13566. doi:10.1021/jp036815m.

[14] R.C. Cammarata, K. Sieradzki, Effects of surface stress on the elastic moduli of thin films and superlattices, Phys. Rev. Lett. 62 (1989) 2005–2008. doi:10.1103/PhysRevLett.62.2005.

[15] C.P. Bean, J.D. Livingston, Superparamagnetism, J. Appl. Phys. 30 (1959) S120. doi:10.1063/1.2185850.

[16] E.F. Kneller, F.E. Luborsky, Particle Size Dependence of Coercivity and Remanence of Single-Domain Particles, J. Appl. Phys. 34 (1963) 656. doi:10.1063/1.1729324.

[17] J. García-Otero, A.. García-Bastida, J. Rivas, Influence of temperature on the coercive field of non-interacting fine magnetic particles, J. Magn. Magn. Mater. 189 (1998) 377–383. doi:10.1016/S0304-8853(98)00243-1.

[18] J. Dormann, F. D'Orazio, F. Lucari, E. Tronc, P. Prené, J. Jolivet, et al., Thermal variation of the relaxation time of the magnetic moment of γ-Fe2O3 nanoparticles with interparticle interactions of various strengths, Phys. Rev. B. 53 (1996) 14291–14297. doi:10.1103/PhysRevB.53.14291.

[19] N.A. Usov, S.E. Peschany, Theoretical hysteresis loops for single-domain particles with cubic anisotropy, J. Magn. Magn. Mater. 174 (1997) 247–260. doi:10.1016/S0304-8853(97)00180-7.

[20] J. García-Otero, M. Porto, J. Rivas, A. Bunde, Influence of the cubic anisotropy constants on the hysteresis loops of single-domain particles: A Monte Carlo study, J. Appl. Phys. 85 (1999) 2287. doi:10.1063/1.369539.

[21] M. Knobel, W.C. Nunes, L.M. Socolovsky, E. De Biasi, J.M. Vargas, J.C. Denardin, Superparamagnetism and Other Magnetic Features in Granular Materials: A Review on Ideal and Real Systems, J. Nanosci. Nanotechnol. 8 (2008) 2836–2857.

[22] B.D. Cullity, C.D. Graham, Introduction to Magnetic Materials, Second Ed., Wiley-IEEE Press, 2011.

[23] F.C. Fonseca, G.F. Goya, R.F. Jardim, R. Muccillo, N.L. V. Carreño, E. Longo, et al., Superparamagnetism and magnetic properties of Ni nanoparticles embedded in SiO2, Phys. Rev. B. 66 (2002) 104406. doi:10.1103/PhysRevB.66.104406.

[24] Q. Song, Z.J. Zhang, Shape Control and Associated Magnetic Properties of Spinel Cobalt Ferrite Nanocrystals, J. Am. Chem. Soc. 126 (2004) 6164–6168. doi:10.1021/ja049931r.

[25] G. Salazar-Alvarez, J. Qin, V. Šepelák, I. Bergmann, M. Vasilakaki, K.N. Trohidou, et al., Cubic versus Spherical Magnetic Nanoparticles: The Role of Surface Anisotropy, J. Am. Chem. Soc. 130 (2008) 13234–13239. doi:10.1021/ja0768744.

[26] W.F. Brown, THE FUNDAMENTAL THEOREM OF THE THEORY OF FINE FERROMAGNETIC PARTICLES, Ann. N. Y. Acad. Sci. 147 (1969) 463–488. doi:10.1111/j.1749-6632.1969.tb41269.x.

[27] A.P. Guimarães, Principles of Nanomagnetism, Springer Berlin Heidelberg, Berlin, Heidelberg, 2009. doi:10.1007/978-3-642-01482-6.

[28] J.M.D. Coey, Magnetism and Magnetic Materials, Cambridge University Press, New York, 2010. www.cambridge.org/9780521816144.

[29] M.Y. Rafique, L. Pan, Q. Javed, M.Z. Iqbal, L. Yang, Influence of NaBH4 on the size, composition, and magnetic properties of CoFe2O4 nanoparticles synthesized by hydrothermal method, J. Nanoparticle Res. 14 (2012) 1189. doi:10.1007/s11051-012-1189-6.

[30] S. Okamoto, O. Kitakami, N. Kikuchi, T. Miyazaki, Y. Shimada, Y.K. Takahashi, Size dependences of magnetic properties and switching behavior in FePt L10 nanoparticles, Phys. Rev. B. 67 (2003) 094422. doi:10.1103/PhysRevB.67.094422.

[31] R. Skomski, Nanomagnetics, J. Phys. Condens. Matter. 15 (2003) R841–R896. doi:10.1088/0953-8984/15/20/202.

[32] C.N. Chinnasamy, B. Jeyadevan, K. Shinoda, K. Tohji, D.J. Djayaprawira, M. Takahashi, et al., Unusually high coercivity and critical single-domain size of nearly monodispersed CoFe2O4 nanoparticles, Appl. Phys. Lett. 83 (2003) 2862. doi:10.1063/1.1616655.

[33] J. Wang, F. Zhao, W. Wu, S.-H. Cao, G. Zhao, Magnetic properties in silica-coated CoFe2O4 nanoparticles: Quantitative test for a theory of single-domain particles with cubic anisotropy, Phys. Lett. A. 376 (2012) 547–549. doi:10.1016/j.physleta.2011.12.003.

[34] A.S. Ponce, E.F. Chagas, R.J. Prado, C.H.M. Fernandes, A.J. Terezo, E. Baggio-Saitovitch, High coercivity induced by mechanical milling in cobalt ferrite powders, J. Magn. Magn. Mater. 344 (2013) 182–187. doi:10.1016/j.jmmm.2013.05.056.

[35] K. Maaz, A. Mumtaz, S.K. Hasanain, M.F. Bertino, Temperature dependent coercivity and magnetization of nickel ferrite nanoparticles, J. Magn. Magn. Mater. 322 (2010) 2199–2202. doi:10.1016/j.jmmm.2010.02.010.

[36] S. Chikazumi, Physics of Ferromagnetism, Oxford University Press, 2009.

[37] E.C. Stoner, E.P. Wohlfarth, A Mechanism of Magnetic Hysteresis in Heterogeneous Alloys, Philos. Trans. R. Soc. A Math. Phys. Eng. Sci. 240 (1948) 599–642. doi:10.1098/rsta.1948.0007.

[38] N. Moumen, P. Bonville, M.P. Pileni, Control of the Size of Cobalt Ferrite Magnetic Fluids: Mössbauer Spectroscopy, J. Phys. Chem. 100 (1996) 14410–14416. doi:10.1021/jp953324w.

[39] R. Kodama, Magnetic nanoparticles, J. Magn. Magn. Mater. 200 (1999) 359–372. doi:10.1016/S0304-8853(99)00347-9.

[40] H. Shenker, Magnetic Anisotropy of Cobalt Ferrite (Co1.01Fe2.00O3.62) and Nickel Cobalt Ferrite (Ni0.72Fe0.20Co0.08Fe2O4), Phys. Rev. 107 (1957) 1246–1249. doi:10.1103/PhysRev.107.1246.

[41] C. de Julián Fernández, Influence of the temperature dependence of anisotropy on the magnetic behavior of nanoparticles, Phys. Rev. B. 72 (2005) 054438. doi:10.1103/PhysRevB.72.054438.

[42] F. de Assis Olimpio Cabral, F.L. de Araujo Machado, J.H. de Araujo, J.M. Soares, A.R. Rodrigues, A. Araujo, Preparation and magnetic study of the CoFe2O4-CoFe2 nanocomposite powders, IEEE Trans. Magn. 44 (2008) 4235–4238. doi:10.1109/TMAG.2008.2001545.

[43] B.H. Liu, J. Ding, Strain-induced high coercivity in CoFe2O4 powders, Appl. Phys. Lett. 88 (2006) 042506. doi:10.1063/1.2161808.

[44] E.E. Fullerton, J.. Jiang, S.. Bader, Hard/soft magnetic heterostructures: model exchange-spring magnets, J. Magn. Magn. Mater. 200 (1999) 392–404. doi:10.1016/S0304-8853(99)00376-5.

[45] O. Gutfleisch, M. a Willard, E. Brück, C.H. Chen, S.G. Sankar, J.P. Liu, Magnetic Materials and Devices for the 21st Century: Stronger, Lighter, and More Energy Efficient, Adv. Mater. 23 (2011) 821–842. doi:10.1002/adma.201002180.

[46] A. López-Ortega, M. Estrader, G. Salazar-Alvarez, A.G. Roca, J. Nogués, Applications of exchange coupled bi-magnetic hard/soft and soft/hard magnetic core/shell nanoparticles, Phys. Rep. 553 (2015) 1–32. doi:10.1016/j.physrep.2014.09.007.

Chapter 5

Hard|soft ferrimagnetic core|shell nanoparticles

The study of the magnetic behaviour of cobalt ferrite nanoparticles presented in Chapter 4 has enlighten how, in order to improve the magnetic performance of materials to be used as permanent magnet, an increase in saturation magnetization (M_S) and remanence magnetization (M_R) is required, while maintaining large coercive field (H_C) values. A suitable strategy for obtaining such magnetic properties is the preparation of bi-magnetic nanoparticles, where a hard (large H_C) and a soft (large M_S) magnetic phases are magnetically coupled. Indeed, such combination can lead to the formation of *spring magnet*, systems where the combination of the properties of the hard and soft magnetic phases results in the improvement of the material maximum energy product.

From the practical point of view, the preparation of exchange-coupled bi-magnetic materials requires a good control not only on the crystallinity of each of the two phases, which affects their magnetic properties, but also on the quality of the structural matching at the interface between the two magnetic phases, which dramatically affects the exchange-coupling interaction. [1] Therefore, we decided to investigate the exchange interaction between hard and soft magnetic nanocrystals sharing the same crystallographic structure, facilitating thus the formation of coherent interfaces. Spinel ferrite nanoparticles are particularly suitable to this scope since their magnetic properties can be varied in a wide range depending not only on their size or shape, but also on the nature of the metal ions and on the inversion degree, while the crystal structure is always the same. Starting from the results shown in the previous Chapter, we decided to use for the preparation of core|shell nanoparticles non-stoichiometric cobalt ferrite ($Co_{0.6\text{-}0.7}Fe_{2.4\text{-}2.3}O_4$) as hard phase. As soft phase, manganese-zinc ferrite ($Mn_{0.6}Zn_{0.4}Fe_2O_4$) is a suitable candidate as, in bulk, among spinel ferrites is the one that has the highest saturation magnetization at 0 K, i.e. without taking into account thermal demagnetizing effects. [2] In fact, from the structural point of view, manganese-zinc ferrite is a partially inverted spinel composed of trivalent iron ions and divalent manganese and zinc ones. In this case the theory of Crystal Field Stabilisation Energy (*CFSE*) cannot be used to predict the ions occupancy since $Mn_xZn_{1-x}Fe_2O_4$ is composed by two ions with high-

spin d^5 electronic configuration (Fe^{3+}, Mn^{2+}) and one with d^{10} (Zn^{2+}) and, thus, presenting the same *CFSE* values in both octahedral (*Oh*) and tetrahedral (*Td*) sites. However, it has been demonstrated that Zn^{2+} ions preferentially occupy *Td* cavities because of its size, while Mn^{2+} lies both in *Oh* and *Td* sites with a larger amount in the latter. Thus Mn,Zn-ferrite can be described by the following formula: $(Zn_xMn_yFe_{1-x-y})[Mn_{1-x-y}Fe_{1+x+y}]O_4$, Moreover, as the zinc amount increase above $x = 0.4$, the compound is reported to became a normal spinel with all manganese ions in the *Td* cavities. [3–5]

From the magnetic point of view, spinel ferrites are characterized by an antiparallel alignment of the *Oh* and *Td* sub-lattices (see Chapter 4). Therefore, depending on the relative values of the magnetic moments of the two sub-lattices, spinel ferrites can be classified as antiferromagnetic (AFM) material or ferrimagnetic (FiM). Manganese-zinc ferrite belongs to FiM spinel ferrites, particularly its magnetic order can be represented as follows:

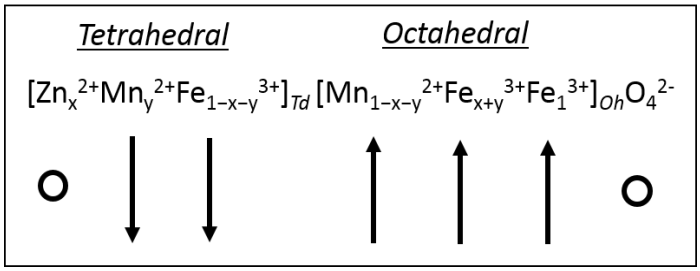

Figure 5.1: Cation distribution in spinel manganese-zinc ferrite.

In particular, the presence of diamagnetic Zn^{2+} ions decreases the magnetic moment of the *Td* sites and, in turn, increases the final moment of the material. In addition, the presence of diamagnetic ions decreases the magnetic interaction between the paramagnetic ions in the *Oh* and *Td* cavities. For higher zinc concentrations ($x > 0.4–0.5$) the ferrite becomes a normal spinel, i.e. with all Mn^{2+} in *Td* sites and Fe^{3+} in *Oh* ones. In such structure, the *Td–Oh* exchange interaction weakens resulting in the presence of spin canting. Accordingly, the zinc doping induces a drop of the coupling between the magnetic ions, which facilitates their magnetization reversal decreasing the material coercivity. [3]

Starting from these remarks, in order to improve the magnetic performances of cobalt ferrite nanoparticles for permanent magnet applications, the synthesis of $Co_{0.6\text{-}0.7}Fe_{2.4\text{-}2.3}O_4|Mn_{0.6}Zn_{0.4}Fe_2O_4$ core|shell nanoparticles was attempted. In particular, *seed-mediated* thermal decomposition was chosen as synthetic procedures as it has been shown it allows the preparation of core-shell hetero-nanostructures with a fine control on the size, crystallinity and morphology. [6] However, all the preparation reported in the literature starts from small seeds (< 15 nm). [6–11] In our case, in order to prepare hard|soft ferrimagnet core|shell nanoparticles for permanent magnets application, large cobalt ferrite core (≥20 nm) must be used as seeds. Indeed, the hard phase core has to be large enough to be in the blocked state at room temperature. Nevertheless, the use of blocked nanoparticle

can strongly affect the stability of the seeds dispersion because of particles dipolar interaction, thus limiting the particle's surface availability for shell growth.

On the other hand, the preparation of nano-sized soft phase presenting large magnetic moment is a challenging aspects. Indeed, the synthesis of $Mn_{0.6}Zn_{0.4}Fe_2O_4$ nanocrystal, despite of the large amount of strategies reported in the literature, usually gives rise to systems presenting considerably low magnetization values with respect to the bulk counterpart. [12–16] Such problem has been commonly ascribed to cations rearrangement occurring at the nanoscale, which leads to deviations from the expected $(Zn_xMn_yFe_{1-x-y})[Mn_{1-x-y}Fe_{1+x+y}]O_4$ site occupancy. [17] Therefore, in order to prepare high crystalline exchange-coupled $Co_{0.6\text{-}0.7}Fe_{2.4\text{-}2.3}O_4|Mn_{0.6}Zn_{0.4}Fe_2O_4$ core|shell nanoparticles, these two critical aspects (low stability of large seeds, and low magnetization of the soft phase) were first investigated separately. Therefore, first the synthetic procedure was optimized in order to obtain core|shell nanoparticles with a large cobalt ferrite core. In this case magnetite or manganese ferrite were used as soft shell. Indeed, even if not presenting high saturation magnetization as the manganese-zinc counterpart, magnetite and manganese ferrite are easily achievable and, thanks to their magnetically soft behaviour, allow assessing the establishment of exchange-coupling interaction with the cobalt ferrite core. In addition, as it will be shown, it has been observed a modification in magnetic behaviour of cobalt ferrite nanoparticles following the heating procedure required for the shell growth. Such evolution of the magnetic properties will be described as a function of the heating temperature.

In the second step, the synthesis of pure $Mn_{0.6}Zn_{0.4}Fe_2O_4$ nanoparticles was investigated to optimize the synthetic parameters to prepare nanoparticles with the desired stoichiometry and magnetic behaviour.

Finally, the magnetic properties of a series of hard-soft exchange-coupled nanocomposites, formed by hard cobalt ferrite and soft iron-cobalt alloy were also investigated, allowing to get precious information about the dependence of material magnetic performances on the exchange-coupling degree.

5.1 Synthesis of ferrites core|shell nanoparticles

As previously mentioned, the synthesis of core|shell nanoparticles based on ferrites was carried out through *seed-mediated* thermal decomposition. [6] However, because of the requirement of using large cobalt ferrite seeds (>20 nm), which strongly affects the stability of the seeds dispersion, different attempts were performed in order to detect, firstly, the proper conditions of growth of the shell and, then, to get coherent core and shell structures allowing the formation of a good quality interface. To this aim we operated as follows:

(I) First, small size cobalt ferrite nanoparticles (13 nm) were used as seeds for the growth of a magnetite shell in order to evaluate the possibility to form a good quality interface and thus high exchange-coupling.
(II) Then, the *seed-mediated* approach was optimized for the use of large size cobalt ferrite seeds (32 nm) for the growth of a manganese ferrite shell.

5.1.1 Small core|shell nanoparticles

Cobalt ferrite nanoparticles with average size of 13 nm were synthesized through lauric acid (LA) assisted thermal decomposition by solving 1 mmol of metal precursors (0.33 mmol of $Co(acac)_2$ and 0.67 mmol of $Fe(acac)_3$) and 4 mmol of LA in 50 mL of Bz_2O. The reaction mixture was degassed bubbling N_2 at 120 °C for 60 min, then it was heated following the usual two stages temperature ramp (first step at 210 °C for 120 min, second at 300 °C for 60 min). Finally, cobalt ferrite seeds were washed and re-dispersed in hexane; in order to avoid particles precipitation a diluted suspension has been achieved using 60 mL of hexane as solvent and 6 drops of OA as stabilizing agent. Afterwards, the magnetite shell growth was carried out following a slightly modified procedure already reported for preparing magnetite nanoparticles through *seed-mediated* thermal decomposition. [7] In particular, 15 mL of seeds dispersion was added to 50 mL of a Bz_2O mixture containing 1 or 0.5 mmol of $Fe(acac)_3$, 2 mmol of OA, 2 mmol of OAm, 2 mmol of 1,2-hexadecanediol (HDD). It has to be noted that, conversely to cobalt ferrite synthesis, in this case we used the presence of HDD to grant for iron reduction ($Fe^{3+} \rightarrow Fe^{2+}$) which is required for magnetite formation. [18] Then, hexane was evaporated and the reaction mixture degassed bubbling N_2 at 120°C for 60 min; the nanoparticles formation was carried out heating at 300 °C for 60 min. Two samples were prepared (CS2 and CS5) by varying the metal precursor amount in order to assess its effects on the shell thickness and, more importantly, to ensure the possibility of promoting heterogeneous nucleation leading to the shell grown on pre-synthesized seeds instead of the formation of single-phase nanoparticles (homogeneous nucleation).

In Figure 5.2, TEM analysis shows LA-assisted thermal decomposition provided narrowly distributed nanoparticles with mean particles size of 13(2) nm. In addition, in both cases the *seed-mediated* synthetic procedure led to a double-distribution of particle size; indeed, both larger and smaller nanoparticles with respect to the starting cobalt ferrite seeds can be observed in the images. In particular, the larger nanoparticles, of average size of 17(2) and 23(2) nm for CS2 and CS5, respectively, could arise from heterogeneous nucleation of magnetite over pre-formed cobalt ferrite seeds (Co-ferrite|magnetite core|shell nanoparticles). Furthermore, even if the core|shell structure could not be recognized by TEM analysis as magnetite and cobalt ferrite have too similar electron density to give an appreciable contrast, the absence in grown samples of a population superimposable to the seeds one, corroborated the growth of a magnetite shell over the pre-synthesized cobalt-ferrite seeds. Accordingly, the shell thickness (t^s) was estimated as half the difference

between the mean particles size of CS nanoparticles and seeds, and was found t^s = 2 and 5 nm for CS2 and CS5 samples. The different shell thickness was achieved by varying the iron precursor concentration: particularly, t^s = 2 and 5 nm were obtained starting from 1 or 0.5 mmol of $Fe(acac)_3$, respectively. The observed trend could be explained in terms of competition between heterogeneous and homogeneous nucleation, the latter becoming disadvantaged as the precursors concentration decreases. On the other hand, the presence of small nanoparticles, of 8(1) and 9(2) nm, for sample CS2 and CS5, respectively, hints the homogeneous nucleation occurred during the shell growth process of both samples, suggesting lower precursors amount could be investigated in order to avoid it.

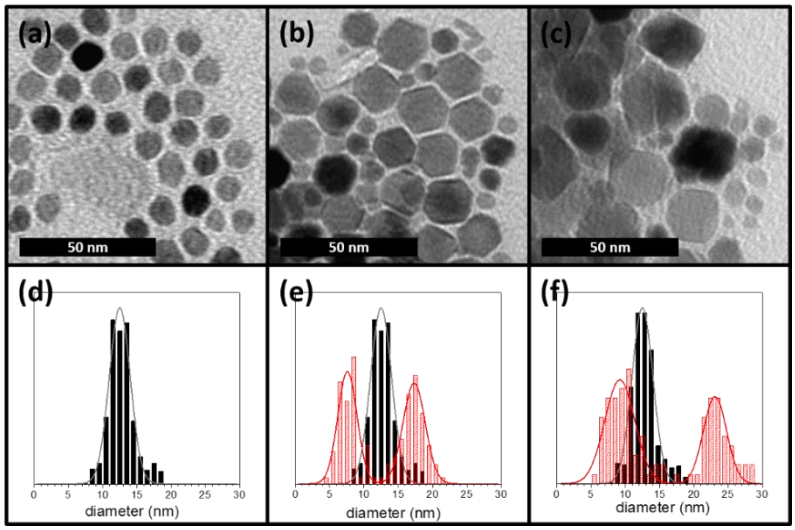

Figure 5.2: (*From the left)* TEM images of pristine 13(2) nm cobalt ferrite seeds (a) and 17(2) and 23(2) nm cobalt ferrite|magnetite core|shell nanoparticles, (b) and (c) respectively. Size histograms of seeds (black) and core|shell nanoparticles (red); in the histogram of CS nanoparticles the size distribution of seeds is also reported for the purpose of better comparison.

In order to evaluate the magnetic properties evolution following the shell growth, core|shell nanoparticles static magnetic properties were analysed by standard magnetometric techniques. In particular, magnetic properties of nanoparticles were measured on tightly randomly packed powder samples using a vibrating sample magnetometer (VSM). The temperature dependence of the magnetization was investigated after zero field cooling (ZFC) and field cooling (FC) procedures in the presence of a 50 Oe applied field and the obtained data are shown in Figure 5.3. The ZFC curve of cobalt ferrite seeds presents a maximum at 320 °C, which, as discussed above, can be taken as the *blocking temperature*, T_B, of the system. Conversely, core|shell nanoparticles are still in the *blocked* state at least until 380 K, being the ZFC and FC curves not superimposed in all the investigated temperature range. Such increase of the T_B of the material could be ascribed to the increase in particles volume, being:

$$T_B = \frac{K_{eff} V}{25 k_B} \qquad 5.1$$

where K_{eff} is the total effective anisotropy constant, which is intermediate between those of the hard and soft phase, and V is the particle volume.

In addition, the ZFC curve of CS2 sample shows the presence of a kink at low temperature (~120 K). The possibility that such feature could be attributed to the Verwey transition typical of magnetite can be discarded as it is not observed in the corresponding FC curves; [19] conversely, it can be attributed to the blocking of the small nanoparticles of the soft phase, an hypotheis supported by literature data reporting a T_B close to 120 k for 8 nm magnetite nanocrystals [20] Curiously, such feature was not visible in the ZFC curve of CS5, even if also in this case, the presence of a population of small nanoparticles, was established by TEM analysis. This discrepancy could be ascribed to the lower volume ratio between the small and large nanoparticles of CS5. In addition, the decrease in small-to-large nanoparticles volume ratio corroborated that the decrease of iron precursors concentration limited the homogeneous nucleation of soft phase (formation of single phase nanoparticles) in favour of heterogeneous nucleation (shell growth).

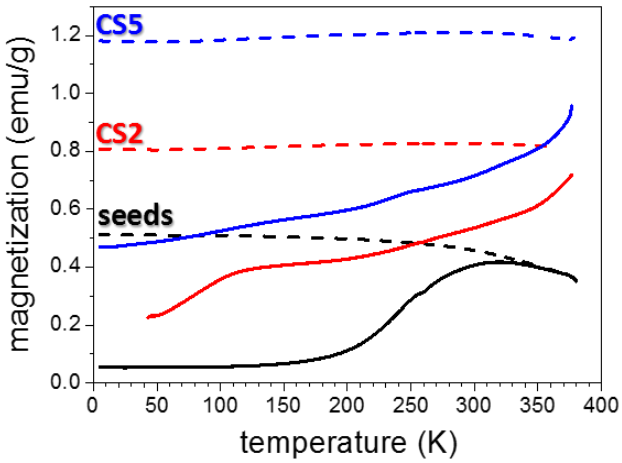

Figure 5.3: Temperature dependence of the ZFC (solid line) and FC (dashed line) magnetization curves recorded at 50 Oe for 13 nm cobalt ferrite seeds (black), CS2 (red) and CS5 (blue).

In addition, hysteresis loops were measured to evaluate the effect the core|shell structure on the magnetic behaviour. Because of the small size of cobalt ferrite seeds, which are almost unblocked at 300 K, magnetic measurement were performed at both room and low temperature. Hysteresis loops recoded at 10 K (Figure 5.4-a) show a large decrease on H_C when moving from cobalt ferrite seeds to Co-ferrite|magnetite core|shell nanoparticles. In particular, the H_C of core|shell are comprised between the values expected for pure cobalt ferrite (see Chapter 4) or for magnetite nanoparticles with the same total volume (17 or 23

nm for CS2 or CS5, respectively), [21] suggesting the presence of exchange coupling between the two phases. In addition, H_C increases with the shell thickness (t_{shell}) suggesting exchange coupling extends to the entire soft phase of core|shell nanoparticles, i.e. $t_{shell} < 2\delta_H$, where δ_H is the width of a domain wall in the hard phase (see Chapter 2). Hysteresis loops of the grown sample show the presence of an additional nucleation field at around 2 kOe. Such nucleation field, even being larger than that commonly observed in magnetite nanocrystals, could be due to the presence of pure magnetite nanoparticles. Indeed, it is more pronounced in sample CS2 in good agreement with the presence of a higher relative amount of pure magnetite nanoparticle.

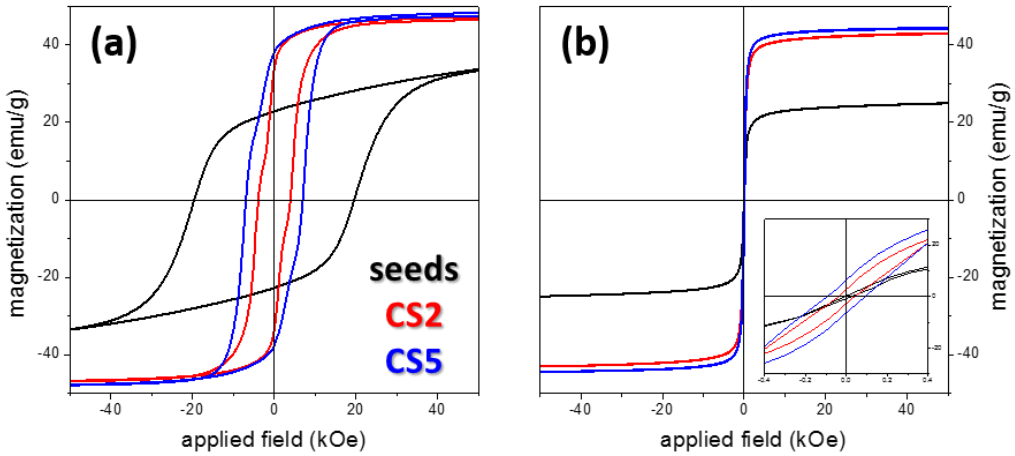

Figure 5.4: *(From the left)* Low temperature (10 K) and room temperature (300 K) hysteresis loops of cobalt ferrite seeds and Co-ferrite|magnetite core|shell nanoparticles. The inset shows the region near H = 0 to better visualize the behaviour of R and H_C. Low temperature measurements were performed following a field cooling process with 50 kOe applied field. In the figure magnetization value are reported for the weight of the as prepared samples, being the amount of sample not enough for the determination of the organic fraction.

Besides, as reported in Table 5.1, the shell formation induced an enhancement in reduced remanence ($R = M_R/M_S$, where M_R is the remnant magnetization) becoming larger as the shell thickness increases, which corroborated the formation of exchange-coupled core|shell nanoparticles. In addition, while hysteresis loops confirmed the cobalt ferrite seeds are in the superparamagnetic regime (zero H_C and R) at room temperature, the increase in particle volume following the shell formation resulted in opened loops with higher H_C as shell thickness increases. Such increase in H_C values could be explained as a concomitant effect of induced anisotropy in the soft phase through exchange interactions with the hard one and of a decrease in thermal demagnetizing effects because of the nanoparticles enlargement. [21]

Finally, the maximum energy product $(BH)_{max}$ was evaluated at low temperature in order to evaluate the potential increase in magnetic performances after the formation of an exchange-coupled Co-ferrite|magnetite core|shell system. As reported in Table 5.1, the

magnetite shell growth resulted in a $(BH)_{max}$ enhancement ,which is more pronounced as the shell thickness increases, being as large as 150 % for t_{shell} = 5 nm. This result confirms *seed-mediated* thermal decomposition as a suitable approach to produce hard|soft core|shell nanoparticles composed on ferrite with improved magnetic properties for permanent magnet applications.

Table 5.1: Magnetic properties of cobalt ferrite seeds and Co-ferrite|magnetite core|shell nanoparticles.

	$\bar{d}(\sigma)$ (nm)	t_{shell} (nm)	H_C^{10K} (kOe)	M_S^{10K} (emug^{-1})	R^{10K} (M_R/M_S)	$(BH)_{max}^{10K}$ (MGOe)	$(BH)_{max}^{10K}$ enhancement
Seeds	13(2)	-	19.6	35.4	0.65	0.6	-
CS2	17(2) + 8(1)	2	4.0	47.3	0.72	1.2	+ 100%
CS5	23(2) + 9(2)	5	7.0	48.2	0.79	1.5	+ 150%

5.1.2 Large core|shell nanoparticles

Starting from the promising results obtained for small core|shell nanoparticles, we decided to aim at the preparation of core|shell nanoparticles starting from larger cobalt ferrite nanoparticles as seeds. In this case for the shell we selected manganese ferrite which in bulk is a FiM spinel ferrites presenting one of the largest magnetic moment (110 emug^{-1}). [22] Larger (30 nm) cobalt ferrite nanoparticles were synthesized through oleic acid (OA) and oleylamine (OAm) assisted thermal decomposition using $CoCl_2$ as cobalt precursor. In particular, the synthesis of 30 nm nanoparticles was carried out dissolving 1 mmol of metal precursors (0.33 mmol of $CoCl_2$ and 0.67 mmol of $Fe(acac)_3$), 4 mmol of OA and 4 mmol of OAm in 50 mL of Bz_2O. The reaction mixture was degassed bubbling N_2 at 120 °C for 60 min, then it was heated following a two stages program with nucleation at 210 °C for 120 min and growth at 270 °C for 60 min. Finally, cobalt ferrite seeds were washed and re-dispersed in hexane; in order to avoid particles precipitation a diluted suspension was prepared using 60 mL of hexane as solvent and 6 drops of OA as stabilizing agent. Afterwards, the manganese ferrite shell growth was carried out using the same procedure reported for small core|shell nanoparticles. In particular, 15 mL of seeds dispersion was added to 40 mL of a Bz_2O mixture containing 0.075 or 0.15 mmol of metal precursors ($Mn(acac)_2$ and $Fe(acac)_3$,), 0.3 mmol of OA and 0.3 mmol of OAm. Then, hexane was evaporated and the reaction mixture degassed bubbling N_2 at 120°C for 60 min, followed by heating at 300 °C for 60 min. It has to be noted that, compared to previous shell growth, the precursors amount were notably reduced in order to avoid homogeneous nucleation of the soft phase. In addition, the formation of a thicker shell thickness was obtained through an additional shell growth process, which was performed by repeating the procedure used for its preparation (see

Table 5.2). Three different samples were prepared, which in the following will be labelled as CS1, CS3 and CS7.

In Figure 5.5, TEM images and relative histograms show the presence of octahedral nanoparticles with unique size-distribution, whit the exception of sample CS7 (the one obtained through two thermal decomposition of the soft phase precursors stages). In fact, histogram of the latter reveals the presence of both larger and smaller nanoparticles with respect to starting cobalt ferrite seeds, (centred at 44 and 18 nm, respectively) the smaller nanoparticles being probably composed of pure manganese ferrite. Conversely for CS1 and CS3 a monomodal distribution centred at 32 and 36 nm, respectively, were observed.

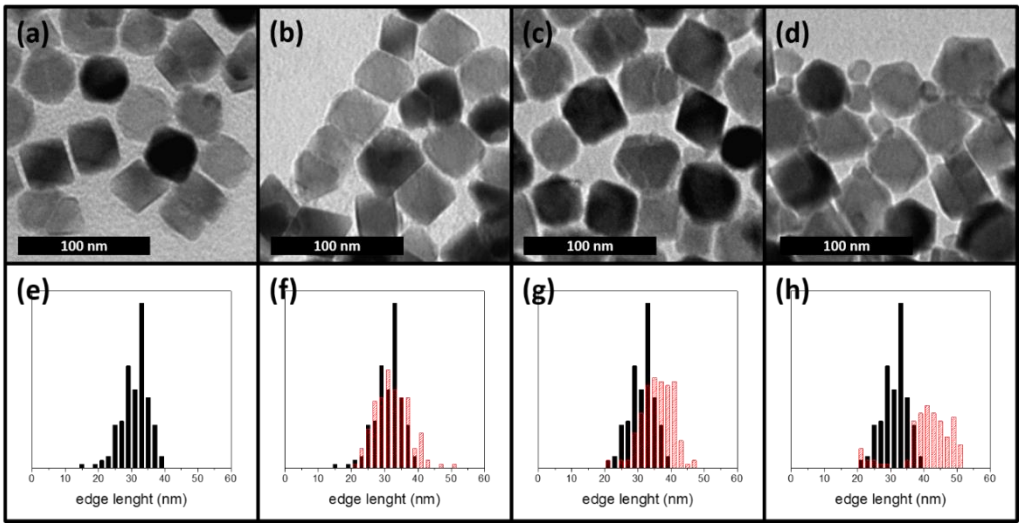

Figure 5.5: (*From the left)* TEM images of 30(5) nm cobalt ferrite seeds (a) and 32(5), 36(5) and 44(6) nm cobalt ferrite|manganese ferrite core|shell nanoparticles, (b), (c) and (d) respectively. Representation of seeds (black) and core|shell nanoparticles (red) particles size histograms. In (f), (g) and (h) the histogram of the seeds is also reported for better comparison.

As in the previous case, the formation of a core|shell architecture could not be ascertained from a difference in contrast since manganese ferrite and cobalt ferrite have similar electron density. The estimation of the shell thickness was obtained from the variation in the average size detected by the size distribution analysis. As expected the variation in precursors concentration resulted in a different shell thickness (t_{shell}): particularly t_{shel} = 1 and 3 nm were obtained starting from 0.075 or 0.15 mmol of precursors, respectively, and t_{shell} = 7 nm for the two steps procedure starting from 0.15 mmol of metal precursors in each one.

Table 5.2: Synthetic parameters used for Mn-ferrite shell formation on 13 nm cobalt ferrite seeds.

	reaction mixture							
	seeds	Bz_2O (mL)	$Mn(acac)_2$ (mmol)	$Fe(acac)_3$ (mmol)	OA (mmol)	OAm (mmol)	$\bar{d}(\sigma)$ (nm)	t_{shell} (nm)

CS1	Co-ferrite	40	0.025	0.05	0.3	0.3	32(5)	1
CS3	Co-ferrite	40	0.05	1	0.3	0.3	36(5)	3
CS7	CS3	40	0.05	1	0.3	0.3	44(6)+18(4)	7

However, concerning CS1, it has to be noted that the observed increase of 2 nm in particle size lies within the standard deviation of the cobalt ferrite seeds population. Moreover, as shown in Figure 5.5-f, the corresponding particle size histograms is practically superimposed to that of cobalt ferrite seeds. Therefore, from the evaluation of the thickness is difficult to surely determine if a manganese ferrite shell has fully formed or not. On the other hand, XRF analysis confirmed the presence of manganese in all grown samples, suggesting the manganese ferrite shell growth occurred, although so thin to not be definitely determined by TEM analysis.

Hysteresis loop at different temperature in the 10 to 300 K range were measured for the series of samples in order to evaluate the shell effect on the magnetic properties. In Figure 5.6, low (10 K) and room temperature (300 K) hysteresis loops are reported.

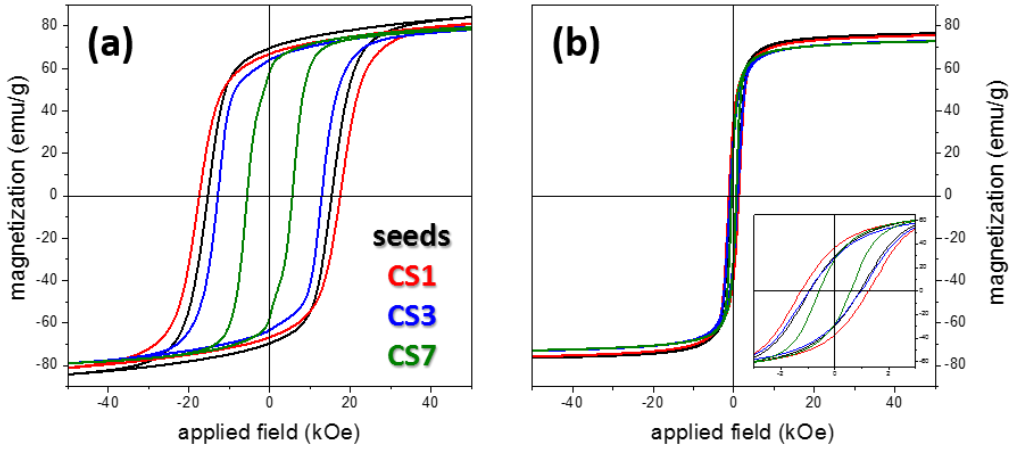

Figure 5.6: *(From the left)* Low temperature (10 K) and room temperature (300 K) hysteresis loops of cobalt ferrite seeds and cobalt ferrite|magnetite core|shell nanoparticles. The inset shows the region near H = 0 to better visualize the behaviour of R and H_C. Low temperature measurements were performed following a field cooling process with 50 kOe applied field. In the figure magnetization value are reported for the total weight of the samples, being the amount of organic fraction unknown (too low amount of material available for analysis).

Coercive field, (H_C), saturation magnetization, (M_S) and reduced remanence, ($R = M_R/M_S$), extracted from both low and room temperature hysteresis loops, are listed in table 5.3 and reported in Figure 5.7 as a function of the shell thickness to better evidence such dependence. M_S remains almost constant for the entire set of samples around 80 and 75 emu/g at low and room temperature, respectively. On the contrary, the coercive field presents a non-monotonous trend with shell thickness at both low and room temperature.

In fact, low temperature H_C first slightly increases (from 15.4 to 17.5 kOe) passing from cobalt ferrite seeds to CS1 and then gradually decreases below the initial value of the seeds as shell thickness increases (12.9 and 5.6 kOe for CS3 and CS7, respectively). Curiously, hysteresis loops of core|shell samples do not show the presence of an additional nucleation field, i.e. no kink is observed during the demagnetizing curves, suggesting the presence of a single phase for each samples, a result that supports the formation of exchange-coupled core|shell nanoparticles. In addition, even CS7 presented a single phase behaviour suggesting the small nanoparticles population to be a small fraction of the sample volume (their magnetic contribution is too low to be observed). At room temperature, H_C values present the similar trend observed at 10 K with the only difference that, instead of being lower, CS3 sample presents the same values recorded for cobalt ferrite seeds. This discrepancy can be ascribed to a decrease in the system anisotropy as the soft phase increases, which is counterbalanced by thermal demagnetizing effects becoming less prominent as particles volume increases. In addition, at low temperature, R shows a similar dependence on the shell thickness observed for H_C with a maximum value of 0.87 for CS1. Conversely, room temperature reduced remanence is constant around 0.4 for each sample, with the only exception of CS1 presenting R = 0.5. The trend of R at room temperature reflects the decreasing of the thermal demagnetization effects because of the increase of particles size.

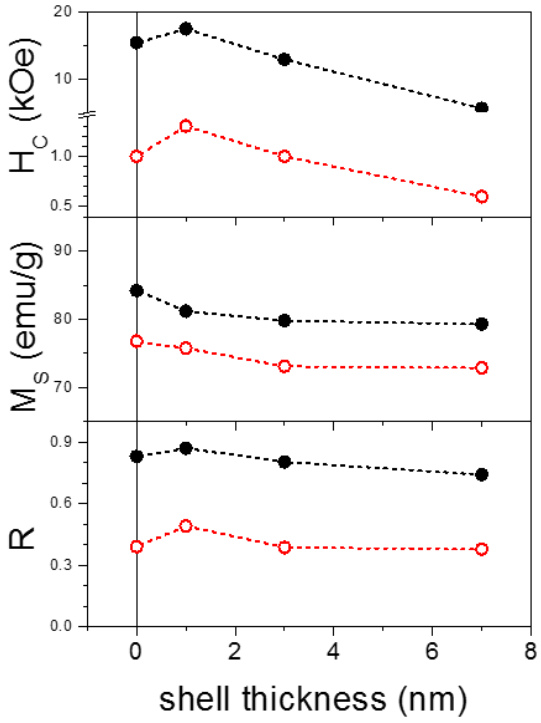

Figure 5.7: *(From the top)* Shell thickness dependence of H_C, M_S, and R measured at 10 K (full black dots) and 300 K (empty red dots).

Taken together, all these data, and particularly the presence of a single switching field and the hysteresis loops evolution with the manganese ferrite shell thickness, agree with the presence of a single magnetic phase arising from exchange-coupling between the hard cobalt ferrite and the soft manganese ferrite. On the other hand, such coercivity loss is not accompanied by the M_S and R enhancement expected for hard|soft exchange coupled systems. Such feature could be ascribed to the formation of a manganese ferrite phase with low M_S as often observed in very small or disordered nanostructure. In addition, it has to be noted that CS1 deviates from the trend observed for the other samples, showing both at low and room temperature a larger H_C and R with respect to the cobalt ferrite seeds. Curiously, such hardening of the material, which is not expected for hard|soft exchange-coupled systems, is observed for the sample whose morphological characterization did not completely granted for the formation of a complete shell of manganese ferrite. A possible explanation for the observed behaviour involve modification induced in the cobalt ferrite seeds by the heating process. Indeed, in order to better understand the effects on the magnetic properties of cobalt ferrite nanoparticles, we performed a series of heating procedures at different temperature on the cobalt seeds by applying the same conditions adopted for the shell growth but without adding the Mn precursor. We observed the hardening of the material (increase of H_C ad R) occurs when cobalt ferrite nanoparticles were heated in a temperature range between 150 and 300 °C. In particular, in accordance with CS1 behaviour, we found H_C increased by 15-25% depending on heating temperature. Interestingly, we observed such evolution of magnetic properties to not be accompanied by modification in particles size, size-distribution, shape, composition or crystallographic structure. Moreover, Mossbauer measurement did not show any modification in the cobalt ferrite inversion degree, which could have been responsible of the modification of the final magnetic properties. Accordingly, further investigation such as the role of dipolar interactions, which is currently in progress, are required to figure out the origin of this unexpected behaviour. .

Further information about the hardening/softening effect induced by the shell growth could be obtained from the estimation of the *effective magnetic anisotropy* (K_{eff}) which was evaluated from the temperature dependence of H_C (see Table 5.3). Assuming the magnetic anisotropy is temperature-independent and the magnetization reversal occurs through a coherent rotation, the effective cubic magnetic anisotropy can be expressed as:

$$K_{eff} = \frac{H_C(0) M_S}{0.64} \qquad 5.2$$

where $H_C(0)$ is the anisotropy field [23,24] and can be experimentally obtained from the analysis of the temperature dependence of the coercive field, which must follows the expression:

$$H_C = H_C(0)\left[1 - \frac{T}{T_B}\right]^{\beta} \qquad 5.3$$

where β is an exponential factor which is 0.5 or 0.77 for oriented or randomly oriented assembly of particles, respectively. [25–27]

In Figure 5.8-b, K_{eff} estimated from the hysteresis loops recorded at various temperature in the range from 5 to 380 K is shown. K_{eff} follows the same trend observed at low temperature for H_C, slightly increasing for CS1 and then markedly decreasing. It has to be noted that pure cobalt ferrite nanoparticles present K_{eff} value in agreement with those previously observed for cobalt ferrite nanoparticles of similar size (Chapter 4). CS1 presents a higher K_{eff} value with respect to pristine cobalt ferrite nanoparticles corroborating the hypothesis that the heating procedure required for shell formation has a hardening effects on the cobalt ferrite seeds. Conversely, as shell thickness is increased the drop in K_{eff} is in agreement with the formation of new exchange-coupled phases and thus the formation of a coherent interface between core and shell regions. In addition, the progressive softening with the shell thickness observed for Co-ferrite|manganese ferrite core|shell nanoparticles confirms the coherency between hard and soft phases is achieved both after one shell grown stage (CS3) and after a two stages process (CS7), validating thus the used synthetic procedures.

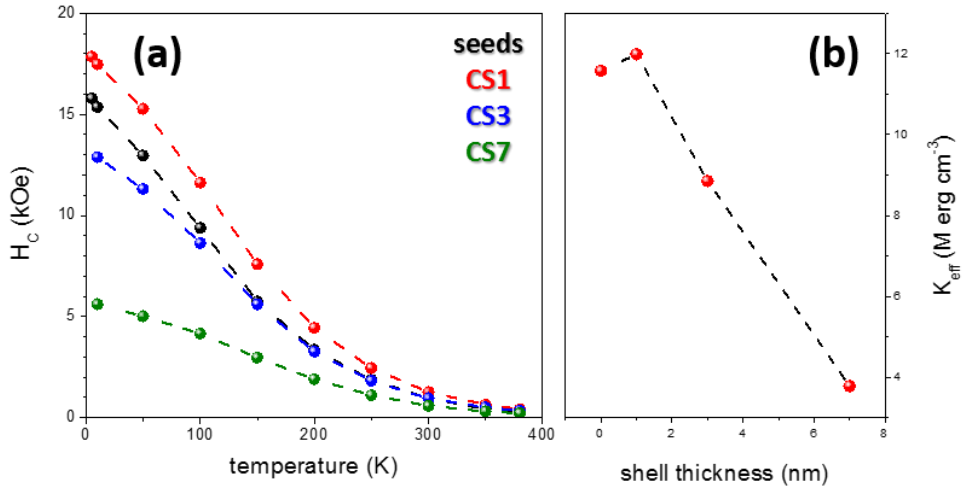

Figure 5.8: (a) Evolution of H_C for the series of nanoparticles as a function of the temperature; (b) Effective magnetic anisotropy, K_{eff}, evolution with the shell thickness.

Table 5.3: Magnetic properties of cobalt ferrite seeds and cobalt ferrite|magnetite core|shell nanoparticles.

	t_{shell} (nm)	H_C^{10K} (kOe)	M_S^{10K} (emug^{-1})	R^{10K} (M_R/M_S)	H_C^{300K} (kOe)	M_S^{300K} (emug^{-1})	R^{300K} (M_R/M_S)	K_{eff} (Mergcm^{-3})
seeds	-	15.4	84.2	0.83	1.0	76.8	0.39	11.6
CS1	1	17.5	81.2	0.87	1.3	75.8	0.49	12.0
CS3	3	12.9	79.8	0.80	1.0	73.1	0.39	8.9
CS7	7	5.6	79.3	0.74	0.6	72.9	0.38	3.8

Finally, low and room temperature maximum energy product $(BH)_{max}$ values were calculated for the series of sample in order to verify if the formation of the exchange-coupled Co-ferrite|manganese ferrite core|shell systems improves the magnetic character of the material, in view of a possible application as permanent magnet. As reported in Figure 5.9, the manganese ferrite shell growth results in a $(BH)_{max}$ monotonous decrease at low temperature. On the other hand, at room temperature $(BH)_{max}$ shows a similar trend to that observed for the reduced remanence, maintaining a constant values around 1 MGOe for all samples, a part for CS1. Such behaviour could be explained by the balance between the anisotropy decrease due to the soft shell formation and the reduction of thermal demagnetizing effect due to the increase in particles mean volume. Conversely, the higher value observed at room temperature for CS1 with respect to that of cobalt ferrite seeds reflects the larger effective anisotropy (larger H_C and R values) of this sample, the magnetization saturation being comparable to that of the seeds.

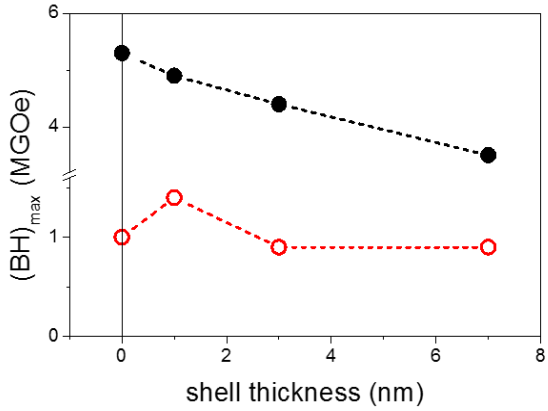

Figure 5.9: $(BH)_{max}$ at 10 (black solid circles) and 300 K (red empty circles) as a function of the shell thickness.

5.2 Synthesis of manganese zinc ferrite nanoparticles

Zinc manganese ferrite nanoparticles were synthesized through thermal decomposition approach as this technique provides high control on the stoichiometry, crystallinity and shell thickness. As previously reported, despite of the many preparations reported in the literature for the synthesis of $Mn_{0.6}Zn_{0.4}Fe_2O_4$ nanocrystals, none of these allowed to obtain systems with the expected high magnetization of the corresponding bulk counterpart. [12–16] However, recently, Jang *et al.* reported the synthesis by thermal decomposition of metal-organic precursors in high-boiling solvents of manganese-zinc ferrite nanoparticles with outstanding high saturation magnetization. [28] Therefore, before attempting to grow a shell of this material on cobalt ferrite, we investigated the optimization of the synthesis of

$Mn_{0.6}Zn_{0.4}Fe_2O_4$ nanocrystals using as a starting point the procedure described by Jang and co-workers. In a typical synthesis 2 mmol of metal precursors and 10 mmol of surfactants (5 mmol of oleic acid, OA, and 5 mmol of oleylamine, OAm) were dissolved in benzyl ether (Bz_2O) in a three-neck round bottomed flask. Initially, the mixture was degassed bubbling N_2 at 120 °C for 60 min and then it was heated at 300 °C for 60 min under a N_2 flow. Finally, the flask was removed from the heating mantle and allowed to cool down under inert atmosphere until the temperature decreased below 50 °C. Then, the as obtained nanoparticles were washed through several cycles of coagulation with ethanol, centrifugation at 5000 rpm, disposal of supernatant solution and re-dispersion in hexane. In particular, the relative amount of metal precursors were varied in order to achieve the desired stoichiometry of manganese-zinc ferrite, i.e., $Mn_{0.6}Zn_{0.4}Fe_2O_4$, corresponding to the highest saturation magnetization among ferrites (6.4 M_B). [2]

In the first attempt (sample MZFO1), following the indication of Jang *et al*. [28] the nanoparticles were synthesized starting from 20% of anhydrous manganese chloride ($MnCl_2$), 13% of anhydrous zinc chloride ($ZnCl_2$) and 67% of iron acetylacetonate ($Fe(acac)_3$) as metal precursors, which correspond to the moles percentage of the target stoichiometry ($Mn_{0.6}Zn_{0.4}Fe_2O_4$). However, XRF analysis showed the formed nanoparticles contain a remarkable low percentage of Mn and Zn, (0.09 and 0.04, respectively) than the nominal content. In addition, although XRD revealed the nanoparticles have the expected spinel *fcc* structure (Figure 5.10), a low saturation magnetization of 65.3 $emug^{-1}$ was obtained from magnetometric measurements, probably due to the presence of structural disorder and/or spin canting. Therefore, larger amount of $MnCl_2$ and $ZnCl_2$ were used in the following synthesis (Mn 30% and Zn 20% in sample MZFO2 and Mn 40% and Zn 30% in MZFO3) to obtain the target stoichiometry. However, as it is shown in Figure 5.10 and reported in Table 5.4, although operating in this way a stoichiometry close to the desired one was obtained, as the relative concentration of Mn and Zn precursors was increased, first, satellite phases were formed, (MZF02) and then the crystallinity of the system was partially lost with a consequent decay in the saturation magnetization of the material (MZF03).

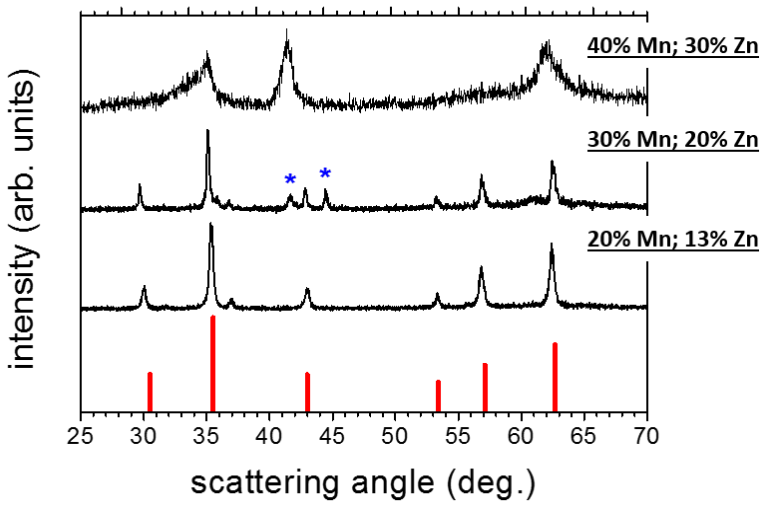

Figure 5.10: XRD pattern of manganese-zinc ferrite synthesized starting with $MnCl_2$, $ZnCl_2$ and $Fe(acac)_3$ and corresponding metal precursors percentage. In red is reported the reference pattern of the spinel *fcc* structure for $Zn_{0.4}Mn_{0.6}Fe_2O_4$ *JCPDS PDF #742401* and in blue are indicated reflections belonging to unidentified satellite phases.

Table 5.4: Elements mole-percentages of reaction mixtures and synthesized nanoparticles (obtained from XRF analysis), samples formula (calculated considering from XRF percentages 100% spinel phase) and saturation magnetization.

	reaction mixture			*XRF analysis*			formula	crystal size (nm)	M_S ($emug^{-1}$)
	Mn (%)	Zn (%)	Fe (%)	Mn (%)	Zn (%)	Fe (%)			
MZFO1	20	13	67	3	65.3	96	$Zn_{0.04}Mn_{0.09}Fe_{2.87}O_4$	62	65.3
MZFO2	30	20	50	14	65.6	76	$Zn_{0.3}Mn_{0.4}Fe_{2.3}O_4$	40	65.6
MZFO3	40	30	30	15	12.9	70	$Zn_{0.5}Mn_{0.5}Fe_2O_4$	-	12.9

As previously discussed in Chapter 4, varying the nature of the metal precursors leads to modifications in its reactivity and/or diffusion, thus affecting the properties of the final nanoparticles. Starting from this consideration, we decided to replace manganese and zinc precursors during the synthetic process in order to possibly avoid the formation of satellite phases. Therefore, the thermal decomposition procedure was performed starting from manganese acetylacetonate ($Mn(acac)_2$) and zinc acetylacetonate ($Zn(acac)_2$), instead of $MnCl_2$ and $ZnCl_2$, together with $Fe(acac)_3$. In this case, as reported in Table 5.5, XRF analysis indicated the formation of nanoparticles with stoichiometry close to the target one ($Zn_{0.4}Mn_{0.6}Fe_2O_4$). In addition, only the formation of spinel *fcc* phases was detected from XRD analysis (see Figure 5.11), even if the presence of broad peaks revealed the formation of smaller crystallites size which could be ascribed to a lower degree of crystallinity of the

systems. Accordingly M_S is very low, which, in turn, could be explained in terms of small crystallite size, usually accompanied by high crystallite strain and structural disorder which strongly decreases the magnetic performances of the magnetic materials. It has to be noted that the substitution of manganese and zinc precursors avoided the formation of satellite phases. However, even if the decrease in material crystallinity appears as the most convincing cause of the low M_S values, the presence of amorphous phase, which could not be detected by XRD, acting as magnetic diluent cannot be discarded.

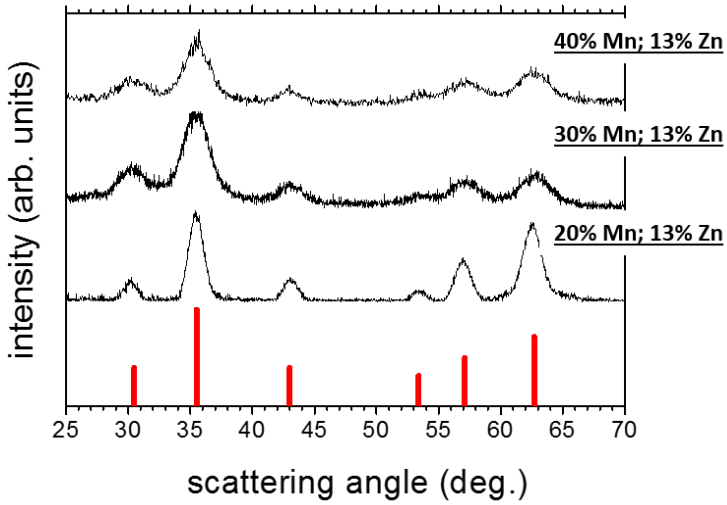

Figure 5.11: XRD pattern of manganese zinc ferrite synthesized starting from $Mn(acac)_2$, $Zn(acac)_2$ and $Fe(acac)_3$ and corresponding metal precursors percentage. In red is reported the reference pattern of the spinel *fcc* structure for $Zn_{0.4}Mn_{0.6}Fe_2O_4$ *JCPDS PDF #742401*.

Table 5.5: Elements mole-percentages of reaction mixtures and synthesized nanoparticles (obtained from XRF analysis), samples formula (calculated considering from XRF percentages 100% spinel phase) and saturation magnetization.

	reaction mixture			*XRF analysis*			formula	crystal size (nm)	M_S ($emug^{-1}$)
	Mn (%)	Zn (%)	Fe (%)	Mn (%)	Zn (%)	Fe (%)			
MZFO4	20	13	67	10	12	78	$Zn_{0.4}Mn_{0.3}Fe_{2.3}O_4$	14	54.2
MZFO5	30	13	57	14	16	71	$Zn_{0.5}Mn_{0.4}Fe_{2.1}O_4$	9	36.9
MZFO6	40	13	47	21	17	62	$Zn_{0.5}Mn_{0.6}Fe_{1.9}O_4$	5	35.4

Finally, a third series of samples was prepared by thermal decomposition synthesis using a further combination of metal precursors i.e $Mn(acac)_2$, $ZnCl_2$ and $Fe(acac)_3$ (sample MZFO7). Also in this case using precursors amount corresponding to the target stoichiometry, XRF analysis showed the formation of Mn,Zn-doped magnetite with a lower

amount of Mn and Zn ($Zn_{0.2}Mn_{0.1}Fe_{2.7}O_4$) than the nominal composition. On increasing the manganese and zinc amount (see Table 5.6 for detail on the various samples prepared) we still observed that when the target metal ratio is approached, the crystalline degree is lowered and, in one case, (MFO12), the formation of satellite phases occurs (see Figure 5.12). In addition, magnetic characterization showed a decrease in saturation magnetization of the material as manganese and zinc precursor amount was increased.

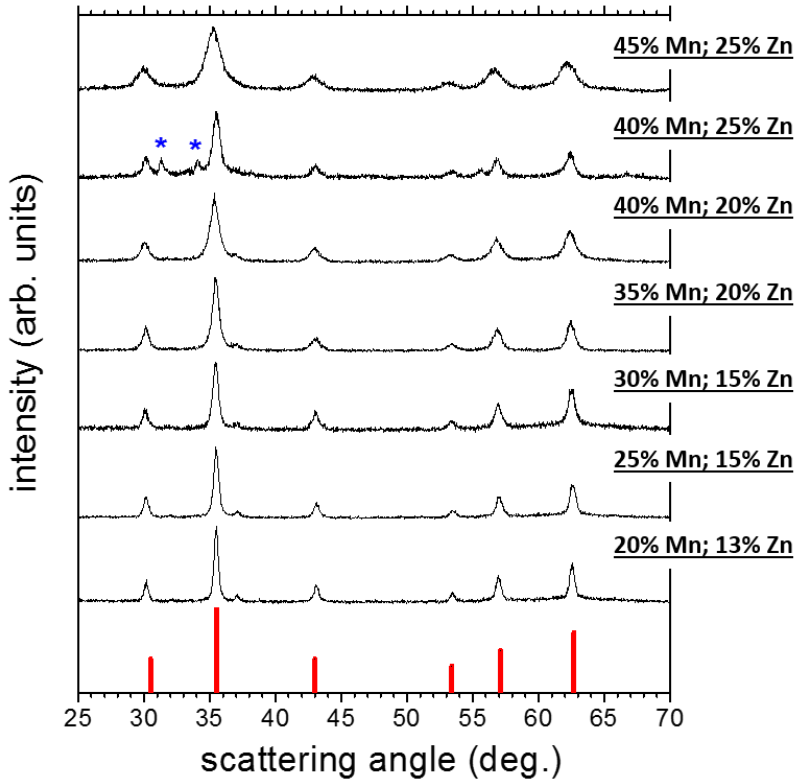

Figure 5.12: XRD pattern of manganese zinc ferrite synthesized starting with $Mn(acac)_2$, $Zn(acac)_2$ and $Fe(acac)_3$ and corresponding metal precursors percentage. In red is reported the reference pattern corresponding to the spinel *fcc* structure for $Zn_{0.4}Mn_{0.6}Fe_2O_4$ *JCPDS PDF #742401* and in blue reflections corresponding to satellite phase.

Table 5.6: Elements mole-percentages of reaction mixtures and synthesized nanoparticles (obtained from XRF analysis), samples formula (calculated considering from XRF percentages 100% spinel phase) and saturation magnetization.

	reaction mixture			*XRF analysis*			formula	crystal size (nm)	M_S ($emug^{-1}$)
	Mn (%)	Zn (%)	Fe (%)	Mn (%)	Zn (%)	Fe (%)			
MZFO7	20	13	67	3	7	90	$Zn_{0.2}Mn_{0.1}Fe_{2.7}O_4$	40	91.5
MZFO8	25	15	60	2	6	92	$Zn_{0.15}Mn_{0.05}Fe_{2.8}O_4$	31	81.1

MZFO9	30	15	55	8	4	88	$Zn_{0.1}Mn_{0.2}Fe_{2.7}O_4$	19	80.9
MZFO10	35	20	45	9	10	81	$Zn_{0.3}Mn_{0.3}Fe_{2.4}O_4$	21	70.9
MZFO11	40	20	40	12	8	80	$Zn_{0.3}Mn_{0.4}Fe_{2.3}O_4$	16	65.8
MZFO12	40	25	35	27	13	60	$Zn_{0.4}Mn_{0.8}Fe_{1.8}O_4$	17	39.4
MZFO13	45	25	30	30	13	57	$Zn_{0.4}Mn_{0.9}Fe_{1.7}O_4$	11	39.2

The low degree of crystallinity which characterized the obtained nanoparticles could be either due to the reaction kinetics, not allowing for the formation of pure manganese-zinc ferrite nanocrystals or to the formation of small nanocrystals, which, because of the confined dimensionality, presents small crystallite sizes. However, TEM analysis was performed on a series of nanoparticles representative of each of used synthetic procedure (see Figure 5.13) and showed that particles sizes are always larger than crystallites size obtained by Rietveld analysis of XRD patterns, hinting the formation of polycrystalline or core/shell ordered /disordered nanoparticles.

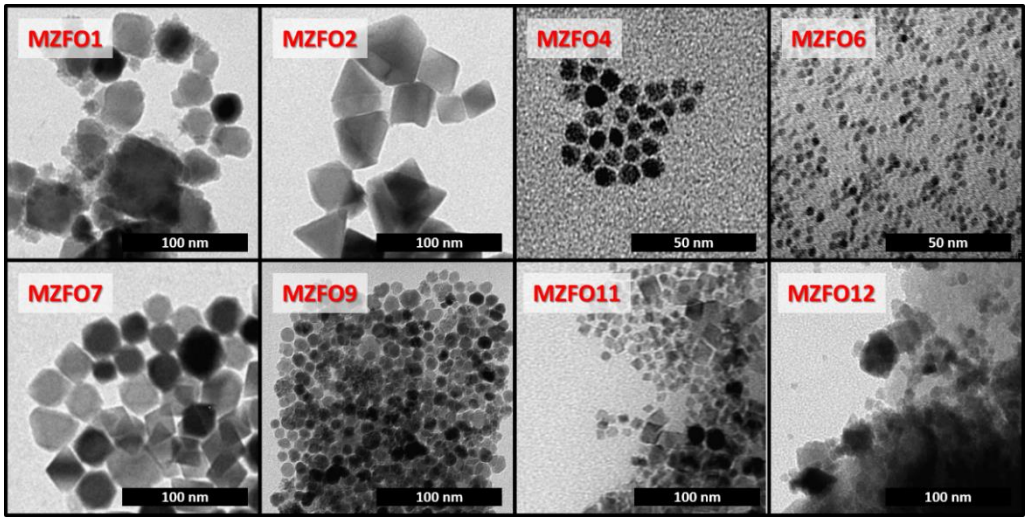

Figure 5.13: TEM images for some representative samples of manganese-zinc ferrite nanoparticles synthesized through thermal decomposition approach.

In conclusion, although many attempts were performed by exploring different metal precursors ($MnCl_2$, $Mn(acac)_2$, $ZnCl_2$, $Zn(acac)_2$ and $Fe(acac)_3$) and different starting concentration, none of them proved to be effective to prepare manganese-zinc ferrite nanoparticles with the proper stoichiometry and good magnetic properties to be used for the preparation of hard|soft ferrites core|shell nanoparticles. Indeed, high saturation magnetizations values were never obtained for the desired composition as the presence of manganese and zinc ions seems to decrease the degree of crystallinity of the final nanoparticles and/or results in the formation of impurities either crystalline or amorphous. Since, to our knowledge, no other ferrite compositions have adequate soft magnetic

behaviour, this result represent a serious drawback towards the synthesis of hard|soft ferrites core|shell nanoparticles, and this strategy can be hardly further considered as a suitable route to improve ferrite magnetic properties for permanent magnet applications.

5.3 Exchange-coupling in $CoFe_2O_4$-FeCo nanocomposites

Among hard-soft exchange-coupled materials, $CoFe_2O_4$-FeCo nanostructures are one the most promising to develop rare-earth free permanent magnets. Indeed, they join the hard magnetic behaviour of cobalt ferrite nanostructures, extensively discussed in previous Chapters, with the notably high magnetization of FeCo alloys (M_S^{bulk} = 235 emug^{-1}). [29] More importantly, exchange-coupled $CoFe_2O_4$-FeCo nanosystems are easily accessible as the partial reduction of cobalt ferrite nanoparticles can directly lead to the formation of a $CoFe_2O_4$-FeCo nanocomposite, where crystallographic coherence, which is mandatory for the establishment of a good exchange-coupling interaction, is more readily achieved than in systems fabricated using two dissimilar materials. [30]

In this paragraph we present the investigation of the magnetic properties of a series of exchange coupled ferrite/metal nanocomposites and we will demonstrates that these class of material is a promising building block towards the realization of high efficiency RE-free permanent magnets.

This investigation is the result of collaboration involving many partners. In fact the nanoparticles synthesis and XRD analysis were carried out at Center of Material Crystallography of Aarhus (Denmark) mainly by Miss Cecilia Granados and Dr. Mogens Christensen; the partial reduction of the nanoparticles and TEM measurements were performed at Istituto de Cerámica y Vidrio of Madrid (Spain) by Dr. Adrian Quesada and Miss Cecilia Granados, while micromagnetic simulations were contrived at General Numerics Research Lab of Jena (Germany) by Dr. Dimitry Berkov and Dr. Sergey Erohkin.

In order to elucidate the magnetic interaction between the two composing phases and its effect on the magnetic properties of the final nanocomposites, a series of samples with a different relative amount of the two phases was investigated. The nanocomposites were obtained by partially reduction of stoichiometric cobalt ferrite nanoparticles prepared by hydrothermal synthesis (CFO). The reduction was carried out through H_2 exposure at high temperature, where the strength of reducing processes was adjusted by varying the H_2 pressure and/or the temperature.

Some selected TEM images of the samples and their composition and crystallite size, evaluated by Rietveld analysis of powder XRD patterns, are reported in Figure 5.14.

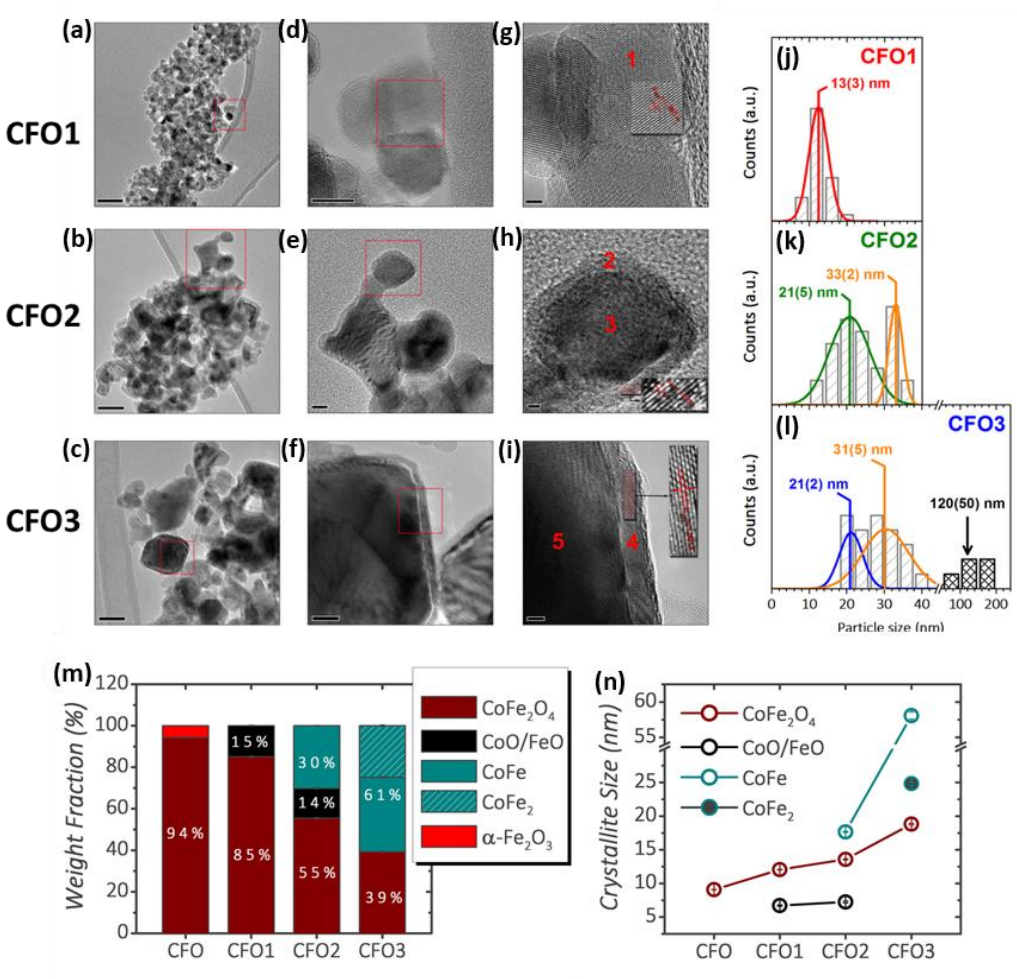

Figure 5.14: (*from the top*) HR-TEM images of CFO1, CFO2 and CFO3 samples. Magnification increases from left to right so that scale bars in (a-c) correspond to 50 nm, in (d-f) to 10 nm and in (g-i) to 5 nm. On the right, particle size histograms for samples (j) CFO1, (k) CFO2 and (l) CFO3. (m) Histogram showing the phase composition in weight percentage for each sample and (n) crystallite size for each of the three phases present in the samples. In both figures, the x-axis corresponds to the reduction stage.

The main features of the samples in terms of composition, morphology and structure are listed below:

CFO. $CoFe_2O_4$ nanoparticles with mean crystallite size of 9 nm presenting 5% of α-Fe_2O_3 (hematite).

CFO1. After the first reduction step (1 mbar of H_2 at 300 °C), hybrid antiferromagnetic(AFM)-ferrimagnetic(FiM) $Fe_{0.67}Co_{0.33}O$-$CoFe_2O_4$ nanoparticles with mean size of 13(3) nm were formed. In particular, the nanocomposite was found to be composed by 15% of AFM $Fe_{0.7}Co_{0.3}O$ and 85% of FiM $CoFe_2O_4$.

CFO2: Increasing the H_2 pressure (20 mbar of H_2 at 300 °C) a nanocomposites presenting three different phases was obtained: 30(2) nm ferromagnetic(FM)|FiM FeCo|$CoFe_2O_4$ core|shell nanoparticles coexisting with 21(5) nm single phase-nanoparticles composed by FiM $CoFe_2O_4$ or AFM $Fe_{0.9}Co_{0.1}O$ phase. The amount of each phase corresponds to 55, 30 or 15% for $CoFe_2O_4$, FeCo and $Fe_{0.9}Co_{0.1}O$, respectively.

CFO3: Finally, increasing the temperature (20 mbar of H_2 at 400 °C) 31(5) and 120(50) nm FM|FiM core|shell nanoparticles with FeCo|$CoFe_2O_4$ and Fe_2Co|$CoFe_2O_4$ stoichiometry, respectively, were obtained, together with 21(2) nm single-phase FiM $CoFe_2O_4$ nanoparticles. In particular, the nanocomposite was found to be composed by 61% of FM FeCo and Fe_2Co phases and 39% of FiM $CoFe_2O_4$. In addition, in contrast to the other samples, which presented a similar particles (TEM) and crystallite (XRD) size, thus hinting the formation of single-crystal nanoparticles, CFO3 presented polycrystalline Fe_2Co phase with ~25 nm crystallites and 120(5) Fe_2Co|$CoFe_2O_4$ nanoparticles.

In order to investigate the magnetic properties of these samples, first, as shown in Figure 5.15, hysteresis loops were recorded at room temperature.

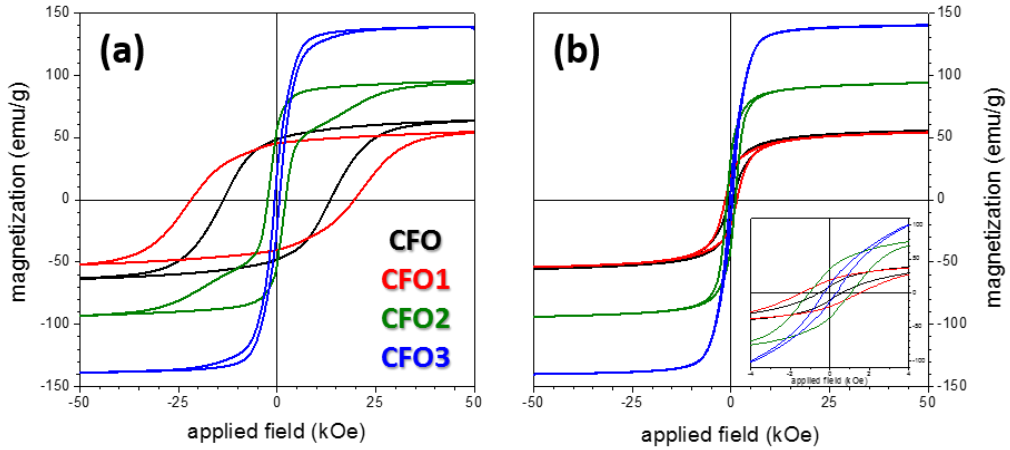

Figure 5.15: (*from the left*) Hysteresis loops recorded at 10 (a) and 300 K (b). Inset shows the region near $H = 0$ to better visualize the behaviour of R and H_C. Low temperature measurements were performed following a field cooling process with 50 kOe applied field.

The $CoFe_2O_4$ nanoparticles (CFO) showed a large hysteresis with a coercive field (H_C) of 0.6 kOe and saturation magnetization (M_S) and reduced remanent magnetization, ($R = M_R/M_S$) of 55.6 $emug^{-1}$ and 0.18, respectively. After the first stage of reduction (CFO1) we observed that M_S is not affected by the treatment, while H_C and R increase with respect to CFO. Such hardening of the material could be ascribed to the increase of the crystallite size, observed in XRD analysis (see Figure 5.14-(n)) and/or to a crystal rearrangement (e.g., variation in the inversion degree of the ferrite). [31] Moreover, the presence of the $Fe_{0.67}Co_{0.33}O$ phase, which is paramagnetic at room temperature could also play a role acting as a magnetic

diluent decreasing inter-particles interaction. [32,33] As expected, as the reduction process advances (the soft phase amount increases), M_S increases reaching 93.9 and 140.2 emug^{-1}, for CFO2 and CFO3 samples, respectively. The large M_S enhancement in CFO3 is nonetheless accompanied by a prominent decay in R and H_C. [1] In fact, the highest R and M_R values are observed for CFO2 (see Table 5.7).

Table 5.7: Low and room temperature magnetic properties of the series of nanocomposites.

	H_C^{10K} (kOe)	M_S^{10K} (emug^{-1})	M_R^{10K} (emug^{-1})	R^{10K}	H_C^{300K} (kOe)	M_S^{300K} (emug^{-1})	M_R^{300K} (emug^{-1})	R^{300K}	$(BH)_{max}$ (MGOe)
CFO	13.6	65.4	48.7	0.74	0.6	55.6	9.9	0.18	0.06
CFO1	20.0	53.9	43.8	0.81	1.5	54.1	19.3	0.36	0.31
CFO2	2.3	95.5	57.7	0.60	1.1	93.9	36.3	0.39	0.57
CFO3	0.6	137.7	22.4	0.16	0.3	140.2	12.5	0.09	0.06

In order to better understand the magnetic properties modifications following the reduction processes, hysteresis loops at low temperature (10 K) were recorded after a field cooling process at 50 kOe. CFO1 presents a remarkable increase in H_C, reaching 20.0 kOe, and a horizontal shift of the loop of 1.1 kOe, evaluated as half the difference between coercive field recorded at negative and positive fields. The shift of the loop is a typical signature of exchange bias H_{ex} and, therefore, it suggests the presence of exchange coupling between ferrimagnetic $CoFe_2O_4$ and antiferromagnetic $Fe_{0.67}Co_{0.33}O$ phases. [1] Moreover, hysteresis loops measured at increasing temperatures show H_{ex} decreases monotonously with temperature vanishing at roughly 200 K (see Figure 5.16-(a)), in good agreement with the expected Néel temperature (T_N) of a Fe-rich antiferromagnetic $Fe_xCo_{1-x}O$ phase. [33] On the other hand, in the hysteresis loop of CFO2 the presence of two different switching fields at 2.3 and 19.4 kOe can be recognized, which could be attributed to two weakly coupled magnetic phases. As can be observed from the dM/dH curve (see Figure 5.16-(b)), the maxima of the largest switching field are found at slightly different fields, i.e., -19.8 and 18.7 kOe. The difference between the two is 1.1 kOe, suggesting also for this sample the presence of exchange bias originating from the formation of $CoFe_2O_4$-$Fe_{0.67}Co_{0.33}O$ exchange coupled interfaces, analogously to the CFO1 sample. Conversely, the switching field at 2.3 kOe lies between the values expected for pure $CoFe_2O_4$ and FeCo phases, which, together to the enhanced M_S, suggests the formation of a $CoFe_2O_4$-FeCo exchange-coupled phase. [1]

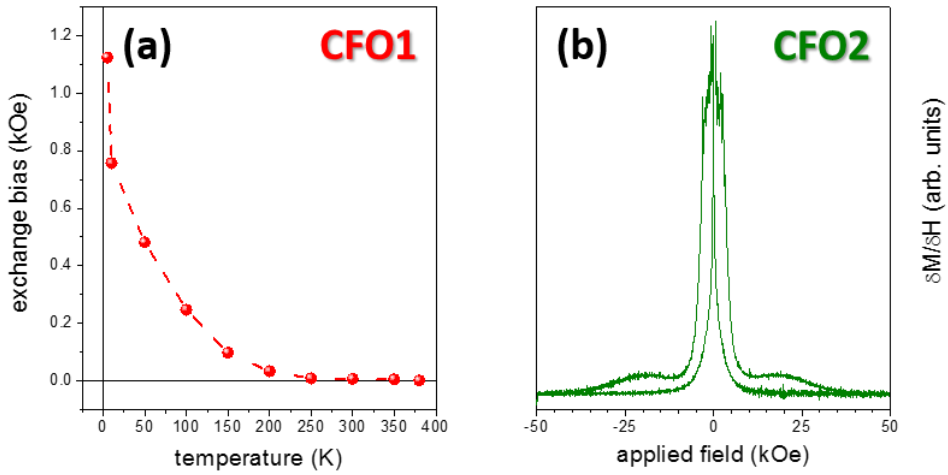

Figure 5.16: (*from the left*) Dependence of H_E with temperature for CFO1. Data are obtained from hysteresis loops recorded after a 50 kOe field cooling process from room temperature. b) CFO2 first derivative of magnetization *vs* applied field curve at low temperature (10 K). Data are obtained from hysteresis loop recorded after a 50 kOe field cooling process from room temperature.

Finally, in the low temperature loop of CFO3 a single switching, large M_s and reduced H_C were observed, indicating the presence of a single exchange-coupled $CoFe_2O_4$-FeCo phase. However, in this case, a pronounced softening of the composite is observed. Indeed, the coercive field is reduced to 0.6 kOe close to the value expected for a pure FeCo phase. [29] It has to be noted that, the single step reversal of CFO3 at 10 K is a strong indication of the large interphase coupling within the nanocomposite, whereas the two-step reversal of the CFO2 sample suggests the hard and soft phases are only weakly coupled. The fact that the presence of two switching fields is revealed only at low temperatures in predominantly uncoupled composites has been reported before. [30]

In addition, we evaluated the maximum energy product at room temperature for the different samples and found the maximum value is observed for the CFO2 nanocomposites, which shows an improvement of an order of magnitude with respect to the initial ferrite (see Table 4.7). Conversely, the perfectly coupled composite (CFO3) presents the lowest energy product.

This results suggest that the conditions to optimize the properties for application as permanent magnet corresponds to a weakly coupled soft-hard composite while full coupling leads to a drop in H_C and, then, in the energy product. Interestingly, the observed drop in H_C as the exchange-coupling degree is increased, has been also confirmed by micromagnetic calculation performed by Dimitry Berkov. In this calculation, CFO2 and CFO3 samples were modelled as a mesh of sphere composed by $CoFe_2O_4$, Fe_xCo or $Fe_{0.9}Co_{0.1}O$ phases with crystallite size end relative amount equal to that evaluated from XRD analysis. The magnetic behaviour was calculated considering standard micromagnetic contributions to the total

energy, namely the energy in the external field, magnetic anisotropy, and exchange and dipolar interaction energies. Minimizing the total energy it has been obtained the magnetization vector field of the sample at a given applied field, which straightforwardly allows the calculation of the magnetization reversal. [34–36]. In particular, the coercive fields were calculated varying the strength of the exchange-coupling interactions, which in turns was simulated by the multiplication of the exchange energy between two mesh elements by a factor κ ($0 < \kappa < 1$). This means that crystallites are perfectly exchange-coupled when $\kappa = 1$ and completely decoupled when $\kappa = 0$. In Figure 5.17 the room temperature H_C evolution with κ is reported for the models representing CFO2 and CFO3. In both cases, a maximum in coercivity is observed for $\kappa \approx 0.1$, which corresponds to weakly coupled phases.

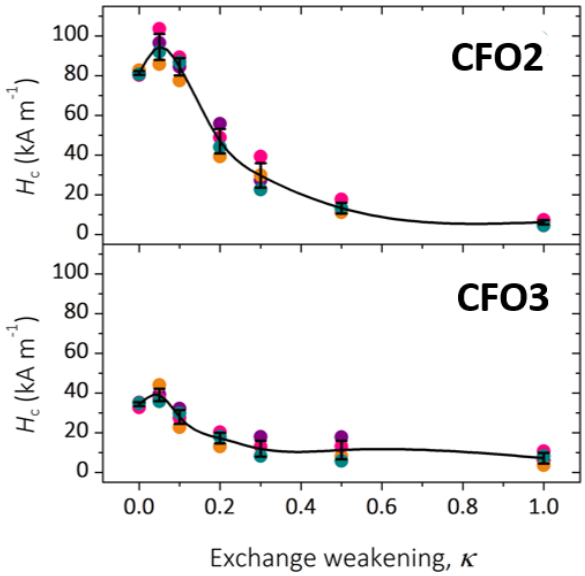

Figure 5.17: Simulated H_C values as a function of the degree of exchange-coupling (κ) for CFO2 and CFO3 models.

Moreover, the experimental decay of coercive field with the reduction strength that we observed, can be descripted phenomenologically by the relation derived by Kronmüller *et al.* using the Brown-Aharoni model: [37–40]

$$H_C = \alpha H_A - N_{eff} M_S \qquad 5.4$$

where H_A is the anisotropy field, α is a microstructural parameter defined mainly by grain sizes, particle arrangements or defects and N_{eff} is the effective demagnetization factor. From Equation 5.2 it appears that a larger amount of soft phase, and thus an increase in M_S, would result in a decrease of H_c. In addition, the increase of the grain size, which occurred as the reduction progressed (Figure 5.14-(n)), can further decrease the coercivity as uncoherent reversal mechanisms start to be effective. [1,31] Moreover, the degree of intergrain coupling

can also affects the coercivity. Indeed, perfect exchange-coupling between randomly oriented particles can decrease the effective anisotropy of the system(the value of H_A). [41] Finally, perfect exchange coupling favours the domain wall propagation, which facilitates magnetization reversal process. [42] Therefore, even if the dimension of the soft component is below the critical size for domain wall formation, the grain boundaries between exchange-coupled particles with randomly oriented easy axis may promote their formation with the following propagation into the hard phase. [43,44] Conversely, the decoupling of grains prevents the decrease of the effective anisotropy and increases the pinning of domain walls at grain boundaries, hindering the domain wall propagation and, thus the coercivity decrease. [45]

On passing from CFO2 to CFO3, a notably decrease in R was also observed. This effect can be ascribed to the different size of the nanoparticles and crystallites. In fact, having smaller crystallites (~25 nm) than the particle size (~120 nm), CFO3 is expected to have multi-domain magnetic structure which result in decreased R and H_C values.

In addition, the exchange-coupling degree also affects the remanence of the composites; indeed uncoupled hard-soft interfaces act as pinning centres, which are known to enhance M_R as they hinder the domain wall motion that demagnetizes the system. [45–47] Conversely, domain wall motion is favoured between perfectly coupled magnetic particles, thus decreasing the remnant magnetization in CFO3 sample. Therefore, the combination of crystal size below the single-domain threshold and the low degree of exchange-coupling between hard and soft phases results in a larger remanence of CFO2 with respect to CFO3.

Finally, it has to be noted that, even if the obtained $(BH)_{max}$ is low with respect to best magnetic materials currently used for permanent magnet application, our results demonstrate that the partial reduction of RE-free metal oxide nanoparticles can be a suitable strategy for significantly increasing their magnetic performances. Indeed, there is plenty of room to increase the absolute value of $(BH)_{max}$ For example, if we would have started from the optimized cobalt ferrite nanoparticles described in Chapter 4 which display a maximum energy product of 2.1 MGOe (18 kJm^{-3}), in principle a $(BH)_{max}$ as large as 20 MGOe can be forecast. On the other hand, the present strategy has the additional advantage that the enhancement of magnetic performances is realized through a reduction process which can be easily scaled up to industrial production. This is a fundamental aspect to be taken into consideration when the potential impact of a technology fro development of permanent magnets is evaluated.

5.4 Conclusions

In conclusion, we have investigated different approaches to prepare hard|soft exchange coupled magnetic nanoparticles to be exploited for realizing RE-free permanent magnets. First, hard|soft ferrites core|shell nanoparticles were synthesized through *seed-mediated*

thermal decomposition both starting from small and large cobalt ferrite seeds. In particular, varying the metal precursor concentration of the shell we found the proper conditions to avoid homogenous nucleation (the formation of pure soft magnetic phase nanoparticles) in favour of heteregenous growth of the soft ferrite shell onto pre-synthesised cobalt ferrite seeds. In addition, the establishment of a coherent interface between core and shell regions were achieved, resulting in the formation of high exchange-coupled systems. The evidences of the preparation of exchange-coupled core|shell nanoparticles were obtained from the softening of the nanocomposites (decrease of H_C, R and K_{eff}) as the shell thickness was increased. These results demonstrates that thermal decomposition is a viable technique to grow hard|soft core|shell nanoparticles starting from large seeds and with a high degree of exchange coupling. On the other hand, it was observed a hardening of pre-synthesized cobalt ferrite nanoparticles following the heating procedure required for the shell growth. The origin of this phenomenon is currently under investigation, however we can anticipate it could be used as a strategy to further improve the coercivity of cobalt ferrite nanoparticles.

Starting from these promising results, we investigated the thermal decomposition synthesis of manganese-zinc ferrite in order to be able to prepare nanocrystals with larger M_S values to be used as soft phase together with cobalt ferrite for the preparation of exchange-coupled core|shell nanoparticles. Unfortunately, synthetic attempts demonstrated a decrease in crystallinity and purity of the soft phase as the manganese and zinc amount is increased to achieve the $Mn_{0.6}Zn_{0.4}Fe_2O_4$ stoichiometry, corresponding to the largest magnetization values Indeed, the highest M_S values we obtained, which is close to that of pure magnetite, was provided by poorly doped ferrite nanoparticles ($Mn_{0.2}Zn_{0.1}Fe_{2.7}O_4$). Although, we do not have any conclusive explanation about this unexpected behaviour we can argue that the slower nucleation kinetics of manganese and zinc precursors or of their reaction intermediates, is the responsible for the poor crystallinity and the formation of satellite phases. However, since both the presence of Mn^{2+} and Zn^{2+} ions and high crystallinity are required in order to obtain ferrites with large magnetic moment, further investigations would be necessary in order to prepare ferrite-based hard|soft exchange coupled systems for high performance RE-free permanent magnets. To this purpose, a possible strategy could the separation of the Zn^{2+} and Mn^{2+} doping process in order to assess the optimal condition to achieve high crystalline nanoparticles. Indeed, the obtainment of $Mn_{0.6}Zn_{0.4}Fe_2O_4$ nanocrystal could be carried out through a first optimization of the synthesis of crystalline Zn-doped cobalt ferrite nanoparticles and a subsequent substitution of Co^{2+} ions with Mn^{2+} ones.

Among the possible alternative strategies for hard|soft nanocomposite production, we explored the reduction of hard magnetic oxides to their metallic form. This appears as a promising approach being also suitable for the production of large amount of material. In particular, a series of exchange-coupled hard-soft $CoFe_2O_4$-FeCo nanocomposites, prepared by Adrian Quesada and Cecilia Granados through H_2 reduction of pre-synthesized cobalt

ferrite nanoparticles, were investigated. The series of samples revealed improved magnetic performances with respect to the single-phase hard magnetic material. In particular, we observed a material softening as the amount of soft phase and the coupling degree between the two phases increase. In this case, because of the remarkably large magnetic moment of the FeCo phase, we observed a large enhancement of the $(BH)_{max}$ (up to ten times with respect to the pre-synthesized cobalt ferrite nanoparticles) despite of the reduction of H_C. Nevertheless, we observed the largest $(BH)_{max}$ value for the weakly coupled nanocomposites. This experimental observation was explained in terms of the presence of a well-defined hard-soft interfaces assuring strong exchange coupling and facilitating the magnetization reversal though wall motion. Accordingly, a collapse in H_C and M_R occurred decreasing the nanocomposites $(BH)_{max}$. This interpretation was corroborated by MonteCarlo simulations performed by Dimitry Berkov. From this investigation we can then conclude that the optimization of the coupling degree is an important parameter to optimize the material performances for developing RE-free permanent magnets.

References

[1] A. López-Ortega, M. Estrader, G. Salazar-Alvarez, A.G. Roca, J. Nogués, Applications of exchange coupled bi-magnetic hard/soft and soft/hard magnetic core/shell nanoparticles, Phys. Rep. 553 (2015) 1–32. doi:10.1016/j.physrep.2014.09.007.

[2] S. Chikazumi, Physics of Ferromagnetism, Oxford University Press, 2009.

[3] D.S. Mathew, R.-S. Juang, An overview of the structure and magnetism of spinel ferrite nanoparticles and their synthesis in microemulsions, Chem. Eng. J. 129 (2007) 51–65. doi:10.1016/j.cej.2006.11.001.

[4] D. Makovec, A. Kodre, I. Arčon, M. Drofenik, Structure of manganese zinc ferrite spinel nanoparticles prepared with co-precipitation in reversed microemulsions, J. Nanoparticle Res. 11 (2009) 1145–1158. doi:10.1007/s11051-008-9510-0.

[5] J.K. Burdett, G.D. Price, S.L. Price, Role of the crystal-field theory in determining the structures of spinels, J. Am. Chem. Soc. 104 (1982) 92–95. doi:10.1021/ja00365a019.

[6] S. Sun, H. Zeng, Size-Controlled Synthesis of Magnetite Nanoparticles, J. Am. Chem. Soc. 124 (2002) 8204–8205. doi:10.1021/ja026501x.

[7] S. Sun, H. Zeng, D.B. Robinson, S. Raoux, P.M. Rice, S.X. Wang, et al., Monodisperse MFe 2 O 4 (M = Fe, Co, Mn) Nanoparticles, J. Am. Chem. Soc. 126 (2004) 273–279. doi:10.1021/ja0380852.

[8] Q. Song, Z.J. Zhang, Controlled Synthesis and Magnetic Properties of Bimagnetic Spinel, (2012).

[9] Q. Song, Z.J. Zhang, Shape Control and Associated Magnetic Properties of Spinel Cobalt Ferrite Nanocrystals, J. Am. Chem. Soc. 126 (2004) 6164–6168. doi:10.1021/ja049931r.

[10] N. Bao, L. Shen, W. An, P. Padhan, C. Heath Turner, A. Gupta, Formation Mechanism and Shape Control of Monodisperse Magnetic CoFe 2 O 4 Nanocrystals, Chem. Mater. 21 (2009) 3458–3468. doi:10.1021/cm901033m.

[11] J.-G.J.-H. Park, E. Lee, N.-M. Hwang, M. Kang, S.C. Kim, Y. Hwang, et al., One-Nanometer-Scale Size-Controlled Synthesis of Monodisperse Magnetic Iron Oxide Nanoparticles, Angew. Chemie Int. Ed. 44 (2005) 2872–2877. doi:10.1002/anie.200461665.

[12] M. Goodarz Naseri, E. Bin Saion, H.A. Ahangar, M. Hashim, A.H. Shaari, Synthesis and characterization of manganese ferrite nanoparticles by thermal treatment method, J. Magn. Magn. Mater. 323 (2011) 1745–1749. doi:10.1016/j.jmmm.2011.01.016.

[13] C. Rath, K.. Sahu, S. Anand, S.. Date, N.. Mishra, R.. Das, Preparation and characterization of nanosize Mn–Zn ferrite, J. Magn. Magn. Mater. 202 (1999) 77–84. doi:10.1016/S0304-8853(99)00217-6.

[14] R. Arulmurugan, B. Jeyadevan, G. Vaidyanathan, S. Sendhilnathan, Effect of zinc substitution on Co–Zn and Mn–Zn ferrite nanoparticles prepared by co-precipitation, J. Magn. Magn. Mater. 288 (2005) 470–477. doi:10.1016/j.jmmm.2004.09.138.

[15] P. Poddar, H. Srikanth, S.A. Morrison, E.E. Carpenter, Inter-particle interactions and magnetism in manganese–zinc ferrite nanoparticles, J. Magn. Magn. Mater. 288 (2005) 443–451. doi:10.1016/j.jmmm.2004.09.135.

[16] S. Calvin, E.E. Carpenter, B. Ravel, V.G. Harris, S.A. Morrison, Multiedge refinement of extended x-ray-absorption fine structure of manganese zinc ferrite nanoparticles, Phys. Rev. B. 66 (2002) 224405. doi:10.1103/PhysRevB.66.224405.

[17] E. Veena Gopalan, I.A. Al-Omari, K.A. Malini, P.A. Joy, D. Sakthi Kumar, Y. Yoshida, et al., Impact of zinc substitution on the structural and magnetic properties of chemically derived nanosized manganese zinc mixed ferrites, J. Magn. Magn. Mater. 321 (2009) 1092–1099. doi:10.1016/j.jmmm.2008.10.031.

[18] J. Lee, S. Zhang, S. Sun, High-Temperature Solution-Phase Syntheses of Metal-Oxide Nanocrystals, Chem. Mater. 25 (2013) 1293–1304. doi:10.1021/cm3040517.

[19] G.F. Goya, T.S. Berquó, F.C. Fonseca, M.P. Morales, Static and dynamic magnetic properties of spherical magnetite nanoparticles, J. Appl. Phys. 94 (2003) 3520. doi:10.1063/1.1599959.

[20] E. Fantechi, G. Campo, D. Carta, A. Corrias, C. de Julián Fernández, D. Gatteschi, et al., Exploring the Effect of Co Doping in Fine Maghemite Nanoparticles, J. Phys. Chem. C. 116 (2012) 8261–8270. doi:10.1021/jp300806j.

[21] P. Guardia, J. Pérez-Juste, A. Labarta, X. Batlle, L.M. Liz-Marzán, Heating rate influence on the synthesis of iron oxide nanoparticles: the case of decanoic acid, Chem. Commun. 46 (2010) 6108. doi:10.1039/c0cc01179g.

[22] D. Carta, M.F. Casula, A. Falqui, D. Loche, G. Mountjoy, C. Sangregorio, et al., A Structural and Magnetic Investigation of the Inversion Degree in Ferrite Nanocrystals MFe 2 O 4 (M = Mn, Co, Ni), J. Phys. Chem. C. 113 (2009) 8606–8615. doi:10.1021/jp901077c.

[23] N.A. Usov, S.E. Peschany, Theoretical hysteresis loops for single-domain particles with cubic anisotropy, J. Magn. Magn. Mater. 174 (1997) 247–260. doi:10.1016/S0304-8853(97)00180-7.

[24] J. García-Otero, M. Porto, J. Rivas, A. Bunde, Influence of the cubic anisotropy constants on the hysteresis loops of single-domain particles: A Monte Carlo study, J. Appl. Phys. 85 (1999) 2287. doi:10.1063/1.369539.

[25] C.P. Bean, J.D. Livingston, Superparamagnetism, J. Appl. Phys. 30 (1959) S120. doi:10.1063/1.2185850.

[26] J. García-Otero, A.. García-Bastida, J. Rivas, Influence of temperature on the coercive field of non-interacting fine magnetic particles, J. Magn. Magn. Mater. 189 (1998) 377–383. doi:10.1016/S0304-8853(98)00243-1.

[27] J.L. Dormann, F. D'Orazio, F. Lucari, E. Tronc, P. Prené, J.P. Jolivet, et al., Thermal variation of the relaxation time of the magnetic moment of γ-Fe2O3 nanoparticles with interparticle interactions of various strengths, Phys. Rev. B. 53 (1996) 14291–14297. doi:10.1103/PhysRevB.53.14291.

[28] J. Jang, H. Nah, J.-H. Lee, S.H. Moon, M.G. Kim, J. Cheon, Critical Enhancements of MRI Contrast and Hyperthermic Effects by Dopant-Controlled Magnetic Nanoparticles, Angew. Chemie Int. Ed. 48 (2009) 1234–1238. doi:10.1002/anie.200805149.

[29] P. Sirvent, E. Berganza, a. M. Aragón, A. Bollero, A. Moure, M. García-Hernández, et al., Effective high-energy ball milling in air of Fe65Co35 alloys, J. Appl. Phys. 115 (2014) 17B505. doi:10.1063/1.4862220.

[30] A. Quesada, F. Rubio-Marcos, J.F. Marco, F.J. Mompean, M. García-Hernández, J.F. Fernández, On the origin of remanence enhancement in exchange-uncoupled CoFe2O4-based composites, Appl. Phys. Lett. 105 (2014) 202405. doi:10.1063/1.4902351.

[31] A. López-Ortega, E. Lottini, C.D.J. Fernández, C. Sangregorio, Exploring the Magnetic Properties of Cobalt-Ferrite Nanoparticles for the Development of a Rare-Earth-Free Permanent Magnet, Chem. Mater. 27 (2015) 4048–4056. doi:10.1021/acs.chemmater.5b01034.

[32] W.F. Li, T. Ohkubo, K. Hono, Effect of post-sinter annealing on the coercivity and microstructure of Nd–Fe–B permanent magnets, Acta Mater. 57 (2009) 1337–1346. doi:10.1016/j.actamat.2008.11.019.

[33] R.M. Cornell, U. Schwertmann, The Iron Oxides, Wiley-VCH Verlag GmbH & Co. KGaA, Weinheim, FRG, 2003. doi:10.1002/3527602097.

[34] A. Michels, S. Erokhin, D. Berkov, N. Gorn, Micromagnetic simulation of magnetic small-angle neutron scattering from two-phase nanocomposites, J. Magn. Magn. Mater. 350 (2014) 55–68. doi:10.1016/j.jmmm.2013.09.031.

[35] S. Erokhin, D. Berkov, N. Gorn, A. Michels, Micromagnetic modeling and small-angle neutron scattering characterization of magnetic nanocomposites, Phys. Rev. B. 85 (2012) 024410. doi:10.1103/PhysRevB.85.024410.

[36] S. Erokhin, D. Berkov, N. Gorn, A. Michels, Magnetic neutron scattering on nanocomposites: Decrypting cross-section images using micromagnetic simulations, Phys. Rev. B. 85 (2012) 134418. doi:10.1103/PhysRevB.85.134418.

[37] A. Aharoni, Theoretical Search for Domain Nucleation, Rev. Mod. Phys. 34 (1962) 227–238. doi:10.1103/RevModPhys.34.227.

[38] W.F. Brown, Virtues and Weaknesses of the Domain Concept, Rev. Mod. Phys. 17 (1945) 15–19. doi:10.1103/RevModPhys.17.15.

[39] H. Kronmüller, Theory of Nucleation Fields in Inhomogeneous Ferromagnets, Phys. Status Solidi. 144 (1987) 385–396. doi:10.1002/pssb.2221440134.

[40] H. Kronmüller, Micromagnetism in hard magnetic materials, J. Magn. Magn. Mater. 7 (1978) 341–350. doi:10.1016/0304-8853(78)90217-2.

[41] G. Herzer, Grain size dependence of coercivity and permeability in nanocrystalline ferromagnets, IEEE Trans. Magn. 26 (1990) 1397–1402. doi:10.1109/20.104389.

[42] Z.B. Li, B.G. Shen, E. Niu, J.R. Sun, Nucleation of reversed domain and pinning effect on domain wall motion in nanocomposite magnets, Appl. Phys. Lett. 103 (2013) 062405. doi:10.1063/1.4817968.

[43] A. Hernando, Exchange interactions and coercitivity in multi-phase magnets, J. Magn. Magn. Mater. 117 (1992) 154–162. doi:10.1016/0304-8853(92)90305-8.

[44] A. Hernando, I. Navarro, J.M. González, On the Role of Intergranular Exchange Coupling in the Magnetization Process of Permanent-Magnet Materials, Europhys. Lett. 20 (1992) 175–180. doi:10.1209/0295-5075/20/2/014.

[45] H. Kronmüller, D. Goll, Micromagnetic theory of the pinning of domain walls at phase boundaries, Phys. B Condens. Matter. 319 (2002) 122–126. doi:10.1016/S0921-4526(02)01113-4.

[46] R. Fischer, H. Kronmüller, Static computational micromagnetism of demagnetization processes in nanoscaled permanent magnets, Phys. Rev. B. 54 (1996) 7284–7294. doi:10.1103/PhysRevB.54.7284.

[47] M.I. Montero, F. Cebollada, M.P. Morales, J.M. González, A. Hernando, Magnetic interactions in Fe–Ba hexaferrite nanocomposite materials, J. Appl. Phys. 83 (1998) 6277. doi:10.1063/1.367774.

Chapter 6

Antiferromagnetic(AFM)|ferromagnetic(FiM) core|shell nanoparticles

As it has been previously discussed, exchange coupled structures are perfect candidates to develop novel materials for permanent magnetic applications. Among exchange-coupled bi-magnetic nanostructures, exchange biased magnets has recently emerged as an alternative strategy to realize hard magnetic nanocomposites. [1–3] In fact, as shown in Chapter 2, exchange interaction at the interface between ferro- (FM) or ferrimagnetic (FiM) and antiferromagnetic (AFM) phases gives rise to a new type of magnetic uniaxial anisotropy. Indeed, the magnetic composite presents exchange bias (H_E), that is an increase of both coercive field (H_C) and remnant magnetization (M_R) and, therefore, enhanced maximum energy product ($(BH)_{max}$). However, the use of AFM material present a critical drawback, the reduction of the magnetic flux of the composite due to the reduced magnetic moment of AFM at the nanoscale. [4] Therefore, an imperative task consists in the optimization of the FM(FiM)|AFM volume ratios. [5] This requirement could be partially fulfilled using nanostructures with large surface-to-volume ratio such as core|shell nanoparticles However, in the case of FM(FiM)|AFM core|shell nanoparticles some crucial issues are still unsolved. Indeed, the magnetic properties dependence as a function of the AFM size is a crucial aspect in order to tune their performances for permanent magnetic applications which needs to be further investigated. [6] On the other hand, being an interfacial effect (see Chapter 2), the interface quality and the relative crystallographic alignment dramatically affect the final magnetic properties of exchange-biased systems. [7,8] Accordingly, several transition metal oxides have been exploited to realize exchange-coupled core|shell nanoparticles, being the inverted rock-salt|spinel $Fe_xO|Fe_3O_4$ AFM| FiM core|shell system the most investigated. [9–12] Interestingly, both structures present similar packing of oxygen ions as shown in Figure 6.1, and thus are useful building blocks to produce high-quality epitaxial superlattices. [13]

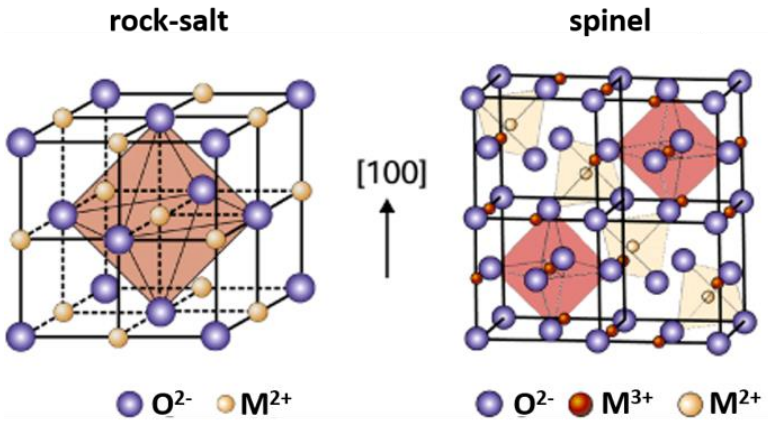

Figure 6.1: Schematic representation of rock-salt and spinel crystallographic structures showing the similarity of oxygen ions lattice.

Amongst the various synthetic strategies recently developed to access to this complex architecture, one-pot thermal decomposition of metal-oleate precursors [14,15] is particularly promising, as it can lead to the formation of core|shell nanoparticles with remarkable epitaxial relationships between the two constituent phases. In fact, the Fe_xO phase forms during the decomposition of the iron oleate precursor due to the generation of large amount of reducing species, (mostly, carbon monoxide). The Fe_3O_4 shell can be generated afterwards by surface oxidation in air, preserving the oxygen sub-lattice of the pristine phase. [16] On the other hand, a major issue of the $Fe_xO|Fe_3O_4$ exchange coupled nanosystem is the low T_N of Fe_xO (198 K). This limitation can be partially overcome by doping the $Fe_xO|Fe_3O_4$ core|shell system with Co^{2+} ions, the ordering temperature of CoO being close to room temperature. In addition, doping the spinel ferrite with cobalt, offers the additional advantage of significantly increasing the magnetic anisotropy of the system. [17]

Therefore, starting from these remarks, in the present Chapter we will report on the investigation of the magnetic properties of a a family of $Co_xFe_{1-x}O|Co_xFe_{3-x}O_4$ core|shell nanoparticles obtained through one-pot thermal decomposition of mixed cobalt and iron oleate complexes. We will show how the high crystalline quality of the boundary and the lack of cation intermixing lead to exceedingly high H_E, even in systems where both components exhibit high magnetic anisotropy. [18] On the other hand, the possibility of engineering core|shell nanoparticles where the size of the AFM core could be systematically varied, while all the others structural parameters remained unchanged, allowed us to address its effect on the exchange coupling.

6.1 Synthesis of $Co_{0.3}Fe_{0.7}O$–(AFM)|$Co_{0.6}Fe_{2.4}O_4$–(FiM) core|shell nanoparticles

Monodisperse spherical nanoparticles were synthesized through thermal decomposition of metal-oleate complex in high-boiling solvents containing oleic acid as stabilizing surfactant, following a procedure slightly modified from that developed by Park *et al*. [14] First, the metal-oleate complexes (i.e., ($Co^{2+}Fe^{3+}$)-oleate) were prepared dissolving 4 mmol of iron chloride hexahydrate ($FeCl_3{\cdot}6H_2O$), 2 mmol of cobalt chloride hexahydrate ($CoCl_2{\cdot}6H_2O$) and 16 mmol of sodium oleate (NaOl) in 10 mL of H_2O, 10 mL of ethanol and 20 mL of hexane and heating the mixture to reflux for 4 h. Then, nanoparticles were synthesized dissolving 1.5 g of ($Co^{2+}Fe^{3+}$)-oleate and 0.15 g of OA in 10 g of 1-octadecene (ODE) or docosane (DCE) in a 50 mL three-neck round bottom flask. The mixture was heated to the desired decomposition temperature at 3 °C min^{-1} for 2 h. In particular, four different decomposition temperatures were selected, 300, 315, 335 and 350 °C, leading to the formation of nanoparticles with different mean size. Finally, the flask was removed from the heating mantle and allowed cooling down. During heating, digestion and cooling processes the mixture was exposed to an N_2 flow. All nanoparticles were washed by several cycles of coagulation with ethanol, centrifugation at 5000 rpm, disposal of supernatant solution and re-dispersion in hexane.

Transmission Electron Microscopy (TEM) images were acquired in order to evaluate the correlation between variation in the decomposition temperature and obtained nanoparticles. In particular, particle size were monitored through mean particle diameter ($\bar{d}$) and standard deviation (σ) obtained by calculating the number average by manually measuring the diameters length of >200 particles from TEM micrographs. The formation of crystalline nanoparticles was investigated through powder X-Ray Diffraction (XRD) and quantitative analysis of obtained data was performed with a full pattern fitting procedure based on the fundamental parameter approach (Rietveld method). [19] The formation of core|shell structures with segregation of crystalline phases in the inner and outer nanoparticles region was investigated with high-resolution transmission electron microscopy (HRTEM). Nanoparticles stoichiometry was monitored through electron energy loss spectroscopy (EELS) in order to highlight accurately core and shell regions compositions. HRTEM and EELS characterization were made by Giovanni Bertoni from CNR-IMEN of Parma (Italy) and Stuart Turner, M. Meledina and G. Van Tendeloo from the University of Antwerp (Belgium).

Transmission Electron Microscopy (TEM) images, reported in Figure 6.2, show a spherical shape and unique size population for all nanoparticles. The corresponding particle size histograms, displayed in the insets, are consistent with a Gaussian distribution with a narrow particle size distribution (≤ 15%) and mean diameter of 6(1), 9(1), 15(2) and 18(1) nm.

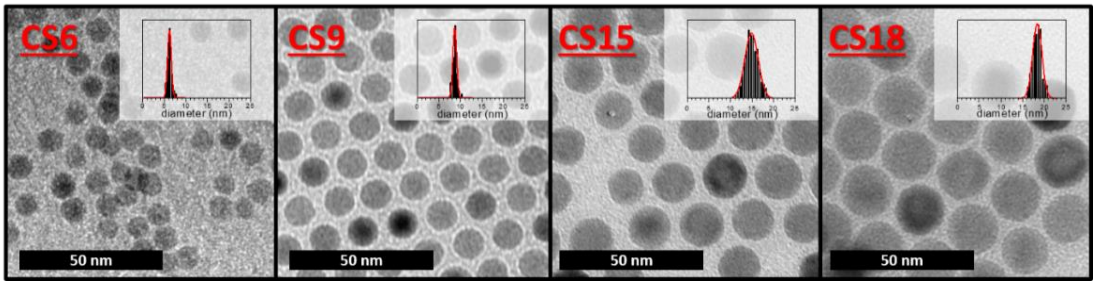

Figure 6.2: TEM images and particle size histograms for nanoparticle of 6 (CS6), 9 (CS9), 15 (CS15) and 18 nm (CS18).

As expected due to the increased reactivity of the metal-oleate precursor with decomposition temperature, [14,20,21] the control of the average particle size was achieved by setting the temperature at 300, 315, 335 and 350 °C for the synthesis of CS6, CS9, CS15 and CS18, respectively. In particular, the mean particles size dependence with decomposition temperature of ($Co^{2+}Fe^{3+}$)-oleate precursor was found to follow a linear behaviour, as shown in Figure 6.3.

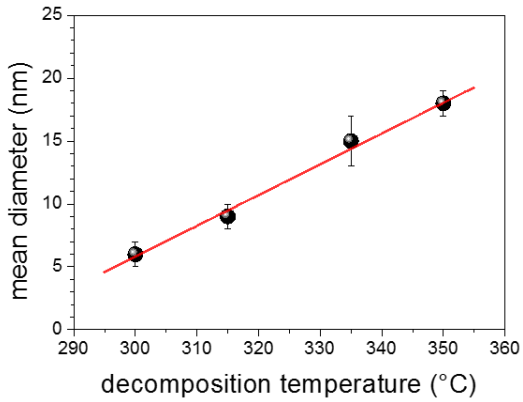

Figure 6.3: Nanoparticles size dependence on thermal decomposition temperature of ($Co^{2+}Fe^{3+}$)-oleate precursor.

High-Angle Annular Dark-Field (HAADF) images demonstrate the formation of a core|shell structure: Figure 6.4 clearly shows two different regions in the nanoparticle, an inner core with higher contrast and an outer shell with lower contrast. In order to corroborate the formation of a core|shell structure, the local fast Fourier transforms (FFT) of a HAADF images were analyzed. FFT images from core and shell regions, revealed the presence of similar *fcc* structures: the core region has the typical periodicity of a rock-salt phase ($Co_xFe_{1-x}O$), while the shell shows diffraction spots related to the cubic spinel structure ($Co_xFe_{3-x}O_4$), i.e. a 0.30 nm interplanar distance between (220) planes. In addition HAADF images were simulated for rock-salt|spinel core|shell structure, showing remarkably similarity with recorded ones, confirming thus the core|shell architecture.

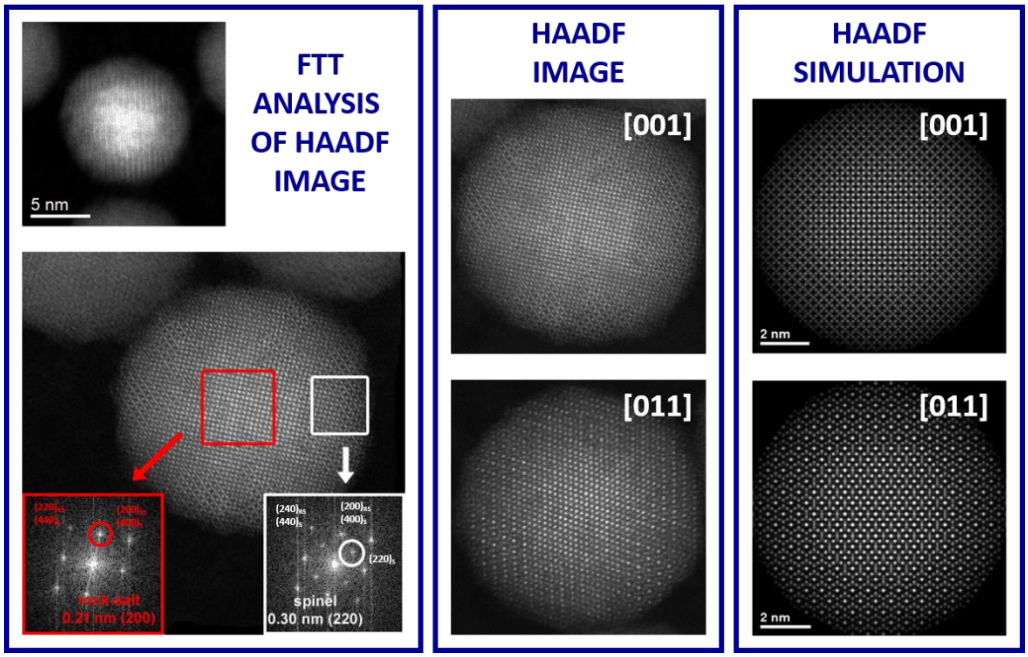

Figure 6.4: HAADF images: FFT analysis on the core and shell regions (left) and comparison between HAADF images and HAADF simulation for rock-salt|spinel core|shell nanoparticles.

Then, in order to assess the elemental distribution within the nanoparticles EELS analysis were performed (Figure 6.5). Elemental quantification shows a clear core|shell structure with a non-homogeneous distribution of iron, cobalt and oxygen along the nanoparticles diameter. Curiously, even if for each sample the ion distributions change with radial distance, the stoichiometry of the core and shell regions are the same for all the investigated samples, independently of particle size. The stoichiometry of the two regions was evaluated by analyzing the oxygen-to-metal ratio variation, shown in Figure 6.5-b. A sharp change from ~1.0 to ~1.3 occurs at a given radial distance for each sample, confirming the MO|M_3O_4 core|shell stoichiometry. In addition, since these compounds are characterized by the presence of only divalent ions in the MO core and by a combination of divalent and trivalent ions in the M_3O_4 shell, a variation in the cobalt-to-iron ratio should be expected in order to maintain charge neutrality (as discussed below, we can reasonably assume that only iron ions are in the trivalent state). In fact, while the iron content is mainly constant along the nanoparticles, cobalt is present in a higher amount into the inner region than in the outer one, the cobalt-to-iron ratio varying from 0.43 in the core to 0.25 in the shell. Furthermore, the Fe^{2+} and Fe^{3+} distribution in the nanoparticles was examined. EEL mapping, obtained by fitting reference spectra to the acquired spectrum image and shown in Figure 6.5-c, displays an evident segregation of iron ions with different oxidation states: Fe^{2+} ions are mostly confined in the core region, while Fe^{3+} ions are exclusively located in the shell.

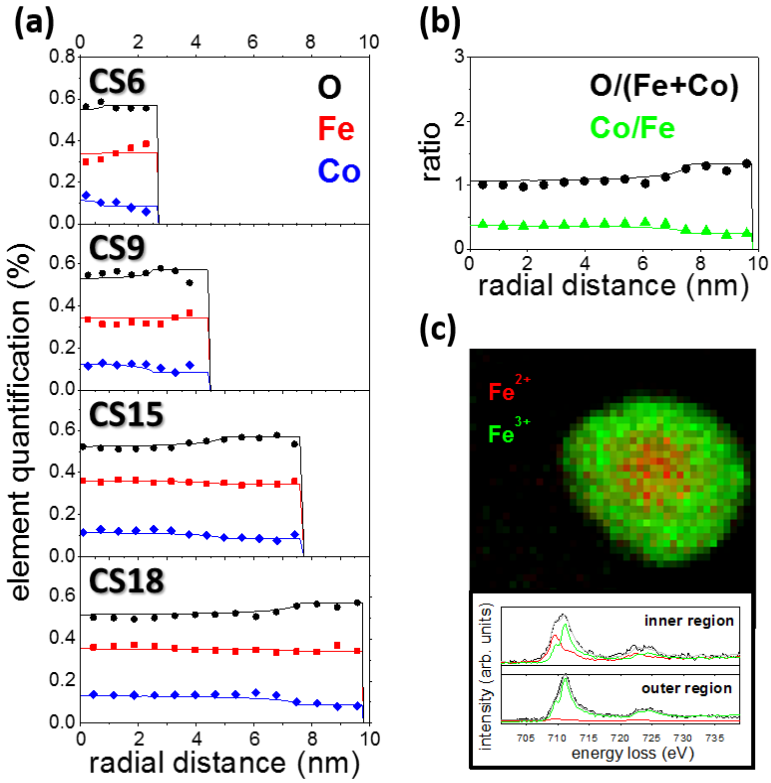

Figure 6.5: (a) Experimental and simulated EELS profiles for each sample of the series. (b) Experimental oxygen-to-metal and cobalt-to-iron ratios along the nanoparticle radius for CS18. The solid lines correspond to the elements amount or ratios estimated for a core|shell structure with composition $Co_{0.3}Fe_{0.7}O|Co_{0.6}Fe_{2.4}O_4$. (c) Iron ions mapping along the nanoparticles and relative emission spectra for CS9.

Combining all these results, core and shell structures can be finally assigned to rock-salt $Co_{0.25}Fe_{0.70}O$ and spinel $Co_{0.6}Fe_{2.4}O_4$ stoichiometries. Comparing different samples, it emerges that nanoparticles present a different average core diameter, which increases with the total particle size, while the shell thickness remains roughly constant (~2 nm) for all nanoparticles, independently of particle size, reaction temperature or solvent.

In addition, XRD analysis (Figure 6.6) confirms the presence of two crystallographic phases, which can be indexed as *fcc* rock-salt and cubic spinel phases; the structural parameters obtained from the Rietveld refinement are reported in Table 6.1. Interestingly, in larger nanoparticles (CS15 and CS18) the cell parameter of the rock-salt phase falls in between those expected for cobalt and iron monoxide (0.425 and 0.429 nm for CoO and FeO, respectively), confirming the formation of a mixed cobalt and iron monoxide.[22–24] Conversely, when the core particle size decreases, the rock-salt unit cell undergoes to a progressive contraction. On the other hand, the spinel phase presents a similar but opposite

behavior: the cell parameter of CS15 and CS18 corresponds to that expected for $Co_{0.6}Fe_{2.4}O_4$, [25] while a slight expansion is observed on decreasing the particle size. It has to be stressed that the deviation of the cell parameter from the bulk value, in our case, is not related to interface effects as it is observed in epitaxial films, where the cell parameter tends to the value of the substrate when the film becomes thinner. [26] On the contrary, in our case both cell parameter contraction and expansion arise from the shell pressure over the core, and *vice versa*, and are considered as a manifestation of coherent interface between the two phases. A similar behavior was indeed previously observed in $Fe_xO|Fe_3O_4$ core|shell nanoparticles, [12,13,27] In addition, it should be stressed that interphase mismatch between core and shell grows from small to large nanoparticles, from 0.2% for CS6 to 1.4% for CS18. This increase can be related to the loss of contraction or expansion suffered by the core or the shell in extremely confined system like small nanoparticles. Crystal sizes obtained from profile broadening analysis for rock-salt and spinel phases are also reported in Table 1. Due to the broadness of the diffraction peaks of the spinel structure and to the overlap between the peaks of the two phases, the following procedure was adopted: starting from the mean diameter values obtained from TEM image statistics, core diameter (d_C) and shell thickness (t_S) were estimated considering a solid sphere shape and a spherical crown, respectively with volume ratio equal to that obtained from Rietveld evaluation. With these assumptions we obtained that the as-synthesized nanoparticles have a constant shell thickness of ~1.4 nm and a core diameter which increases from 3.2 to 14.8 nm (see Table 6.1), in agreement with EELS results.

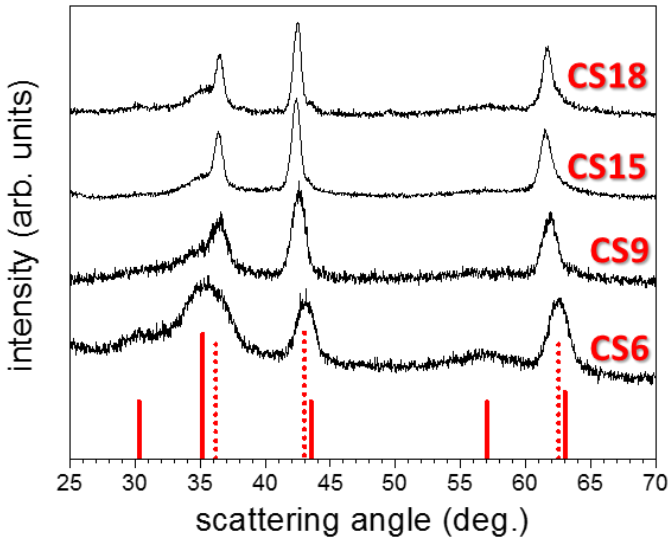

Figure 6.6: XRD patterns of the series of samples. The red lines below show the reflections corresponding to rock-salt (wüstite, dotted line) and spinel (magnetite solid line) crystal structures.

Table 6.1: Left: mean diameter ($\bar{d}$), core diameter (d_{core}), and shell thickness (t_{shell}) obtained from TEM images. Right: cell parameter (a), crystal size (D), core diameter (d_{core}) and shell thickness (t_{shell}) obtained from XRD patterns (RS and S stand for rock-salt and spinel, structure, respectively).

	TEM			XRD							
				Rock-Salt phase (RS)				*Spinel phase (S)*			
	$\bar{d}(\sigma)$ (nm)	d_{core} (nm)	t_{shell} (nm)	a_{RS} (nm)	D_{RS} (nm)	%$_{RS}$ (w%)	d_{core} (nm)	a_S (nm)	D_S (nm)	%$_S$ (w%)	t_{shell} (nm)
CS6	6(1)	2	2	0.420	6.3	13	3.2	0.842	2.3	87	1.4
CS9	9(1)	5	2	0.424	7.4	36	6.6	0.841	2.1	64	1.2
CS15	15(2)	11	2	0.426	14.0	57	12.6	0.841	2.6	43	1.2
CS18	18(1)	14	2	0.426	14.8	53	14.8	0.840	3.0	47	1.6

To conclude, the structural characterization (XRD, HAADF) denotes each sample has rock-salt|spinel core|shell architecture. In particular, also considering the EELS results, the formation of a series of $Co_{0.25}Fe_{0.70}O|Co_{0.6}Fe_{2.4}O_4$ core|shell nanoparticles with variable core diameter and constant shell thickness of ~2 nm is evidenced. The formation of AFM|FiM core|shell nanostructures by thermal decomposition of Fe^{3+}-oleate was previously reported in the literature. [9,13] Indeed, it has been shown that Fe^{3+}-oleate decomposition at high temperatures allows the formation of $Fe_xO|Fe_3O_4$ core|shell nanoparticles through the initial reduction of Fe^{3+} ions to Fe^{2+} due to the breakup of the oleate chain, forming Fe_xO nanoparticles. Later, the surface oxidation of Fe_xO during purification and separation processes leads to the formation of a Fe_3O_4 shell.[16] However, $Fe_xO|Fe_3O_4$ core|shell nanoparticles obtained from Fe^{3+}-oleate undergo a progressive oxidation and thus to the thickening of the Fe_3O_4 shell until the complete disappearance of the AFM core. [28] Conversely, in our case the core|shell structure does not change with the aging of the samples, probably thanks to the higher stability of Co^{2+} ions with respect to Fe^{2+} ones ($E^0_{Fe(III)/Fe(II)}$ = 0.77 V and $E^0_{Co(III)/Co(II)}$ = 1.82 V). [29] Finally, it should be noted that the close relationships between cell parameters of both phases (cell mismatch less than 2%) suggests that the spinel shell formation occurs by a topotaxial transformation of the particle surface through the oxidation of initial $Co_{0.3}Fe_{0.7}O$. Notably, this mechanism allows for the formation of a sharp boundary between the two phases. HAADF simulation images at [100] and [011] directions corroborate the good match between the core and shell observed in the experimental images (see Figure 6.4). [30] Interestingly, even for smaller nanoparticles (CS6) where the reduction in size was found to induce structural distortions (cell expansion and contraction of the spinel shell and rock-salt core, respectively), the good match between the two phases was preserved.

6.2 Magnetic properties of $Co_{0.3}Fe_{0.7}O$–(AFM)|$Co_{0.6}Fe_{2.4}O_4$–(FiM) core|shell nanoparticles

From the point of view of the magnetic properties $Co_{0.25}Fe_{0.70}O|Co_{0.6}Fe_{2.4}O_4$ core|shell nanoparticles can be considered as a single inverted system: that is, the AFM phase is placed in the core and the FiM one in the shell and the ordering temperature of the AFM phase, T_N ($Co_{0.3}Fe_{0.7}O$), expected to be between 198 and 291 K, is lower than that of the FiM one, T_C ($Co_{0.6}Fe_{2.4}O_4$) = 820 K. [31,32] Interestingly, the series of core|shell nanoparticles shows some characteristics which make it an ideal candidate to systematically address the effect of the size of AFM counterpart on the final magnetic properties of the nanosystem. [33,34] This effect has been much less studied than the influence of the FM size. [3] All the samples, indeed, exhibit the same morphology (narrow particle size distribution, spherical shape and constant 2 nm FiM shell thickness), a sharp interface and a high quality structural matching. At first, the temperature dependence of the magnetization after zero-field cooling (ZFC) and field cooling (FC) processes was measured (Figure 6.7).

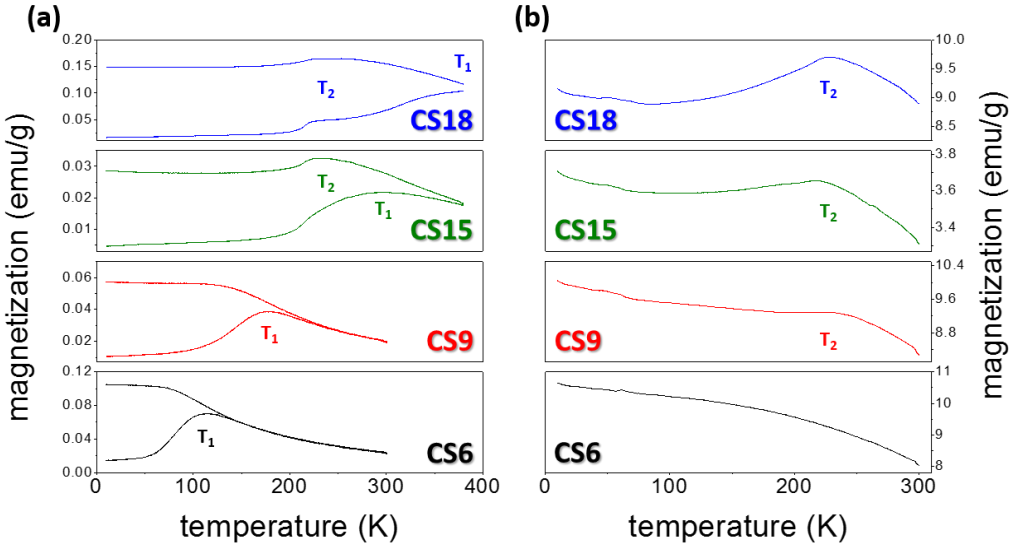

Figure 6.7: (a) Temperature dependence of magnetization for core|shell nanoparticles recorded at 50 Oe after ZFC-FC processes and (b) FC magnetization recorded at 30 kOe.

For all core|shell nanoparticles the ZFC curves present a maximum in magnetization at different temperatures (T_1) above which magnetization decays monotonically and merges with the FC curve. In addition, T_1 is size dependent (see Table 6.2) and increases with particle size. In particular, as reported in Figure 6.8, it scales with the volume of the FiM phase. This behavior is characteristic of superparamagnetic systems, and then, T_1 can be associated to the blocking temperature (T_B) of the FiM spinel shell phase ($Co_{0.6}Fe_{2.4}O_4$). [35] In addition, larger nanoparticles (CS18) are still blocked at room temperature, as expected for cobalt ferrite nanoparticles of 14 nm which is the equivalent particle size of a sphere

with the same volume of a crown sphere of 14 and 18 nm internal and external radius, respectively. [25] Furthermore, it should be noted that another maximum in magnetization (T_2) is observed at a fixed temperature $T_2 \approx 220$ K in the FC curves of CS15 and CS18. A similar increase in the magnetization is also visible in the ZFC curves, even if the kink becomes less prominent as particles size decreases. In order to elucidate the nature of the observed magnetic transitions, 30 kOe FC magnetization *vs.* temperature curves were acquired (see Figure 6.7-b). With the exception of the smallest nanoparticles (CS6), where AFM rock-salt phase is present only in small amount, at 30 kOe the FC curves always present a maximum in magnetization at 220 K. This temperature can be attributed to the T_N of the AFM rock-salt core phase. Notably, this value is intermediate between the T_N of bulk FeO and CoO (198 and 291 K, respectively). [36,37] As reported in the literature, indeed, there exists a linear dependence of T_N with cobalt amount in Co-doped wüstite, being FeO and CoO isostructural antiferromagnetic oxides. [38,39] The estimation of T_N for a $Co_{0.3}Fe_{0.7}O$ structure, assuming the linear dependence, [40] provides $T_N = 226$ K, that is very close to the experimental one. It deserves to be stressed that we observed T_N even for very low size of the AFM phase (5 nm). This result is rather surprising, since for FeO the appearance of the Néel transition is usually reported only for much larger nanoparticles size. [12] Moreover, for the smallest core|shell nanoparticles we cannot exclude that T_N is not visible just because of the too low contribution of the AFM phase. This hypothesis is indeed corroborated by the presence, also on this sample of a large H_E (see below), suggesting the disappearance of the ordering temperature should be rather connected to the progressive loss of structural order than to an intrinsic size effect.

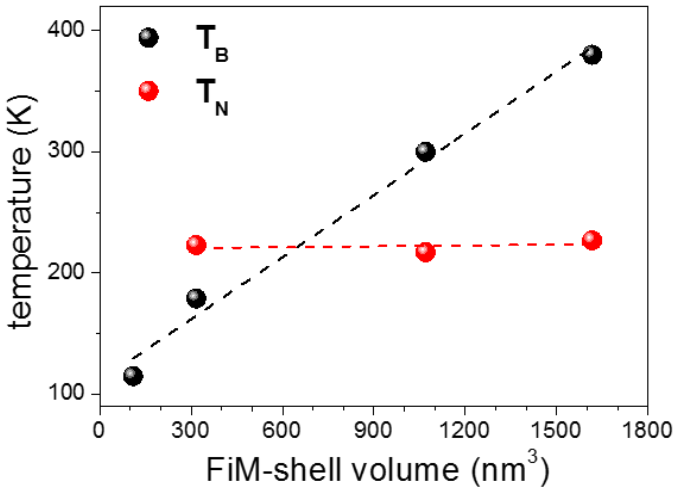

Figure 6.8: Dependence of T_B and T_N with FiM-shell volume.

Hysteresis loops, reported in Figure 6.9, were first measured at low temperature (10 K) following ZFC procedure. ZFC loops show large H_C, in agreement with those expected for cobalt ferrite nanoparticles with similar stoichiometry. [25] In particular, H_C values are

almost constant around 13 kOe, with only a small decrease (<10%) on passing from small to large particle size. The observed behavior, which is markedly different from that commonly observed in single phase magnetic nanoparticles, [25,41] may arise from a combination of size and morphological effects. In fact, the ZFC behavior is mainly determined by the FiM shell, which is characterized by a large surface-to-volume ratio because of its geometry. Moreover, due to the small shell thickness, we cannot exclude that non-coherent magnetization reversal processes are operating depending on the curvature of inner and outer surfaces. The ZFC hysteresis loops are well far from the saturation regime even at high fields, although the reversibility regime was reached close to the highest measuring field and no vertical shifts were observed. The non-saturation behavior can be explained by the presence of a high anisotropic AFM material.

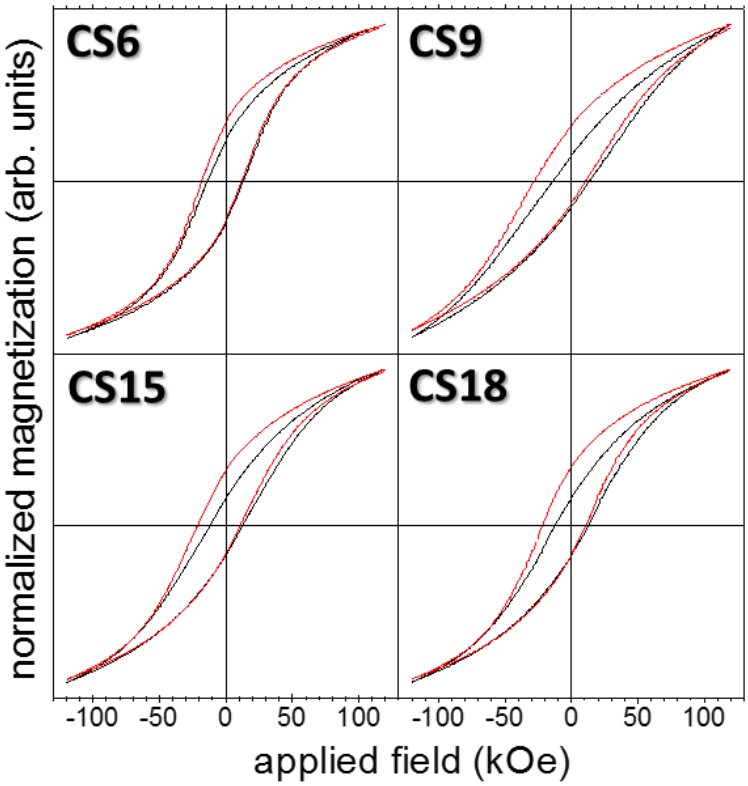

Figure 6.9: Hysteresis loops at 10K of core|shell nanoparticles recorded in a field range of ±120 kOe after ZFC (black) and 120 kOe FC (red) process.

In order to study the exchange coupling properties, low temperature hysteresis loops were measured also after FC from room temperature in a 120 kOe field. The loops show the presence of H_E, i.e. a loop-shift along the field axis, and an enhancement in coercivity, H_C^{FC}, denoting an increase in the effective magnetic anisotropy of the system. These features are typical for exchange coupled AFM and FM or FiM materials. [42]

Table 6.2: Left: blocking temperature (T_B) and Neél temperature (T_N) of core|shell nanoparticles. Right: coercive field (H_C) and exchange bias (H_E) measured at low temperature (10 K) both in ZFC and 120 kOe FC conditions.

	T_B (K)	T_N (K)	ZFC		120 kOe FC	
			H_C^{ZFC} (kOe)	H_E^{ZFC} (kOe)	H_C^{FC} (kOe)	H_E^{FC} (kOe)
CS6	115	-	13.5	0	15.0	3.2
CS9	179	223	13.7	0	19.3	8.6
CS15	300	217	12.4	0	16.2	5.5
CS18	380	227	12.6	0	16.3	5.5

Interestingly, we did not observe any vertical shift of the loops, as reported in previous works focused on similar AFM|FiM core|shell nanoparticles. [29,43,44] In these cases the shift was attributed to the role of uncompensated spins in the FiM layer. However, we believe this effect should be rather related to the fact that the maximum applied field is not large enough to reach the fully reversible regime, independently of any field cooling procedure. This is well demonstrated by the FC minor loop recorded only up to 70 kOe on CS9 and reported in Figure 6.10: conversely to the full loop, the minor cycle is largely shifted along the vertical axis.

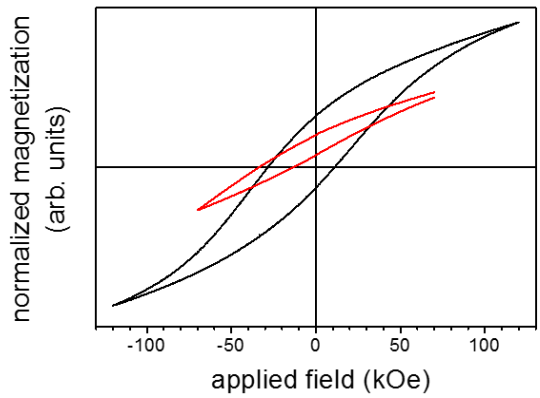

Figure 6.10: CS9 hysteresis loops recorded at 10 K in a field range of ± 70 kOe (red) and ± 120 kOe (black).

An extremely large H_E values, with a maximum of 8.6 kOe for 9 nm CS9 nanoparticles is observed in the FC hysteresis loops. To our knowledge, this corresponds to the largest H_E ever reported for core|shell nanoparticles and can be explained on the basis of high anisotropy of the AFM counterpart and of the high quality of the interface with the FiM shell, i.e. the excellent matching of the two lattices and the remarkable sharp interface. [3,30] Interestingly, the high magnetic anisotropy presented by both the core and shell regions

should theoretically quench H_E and produce the increase of the coercive field alone. [18,45,46] Conversely, in this system we observed simultaneously both phenomena. Indeed, while the demagnetizing branches are shifted towards larger fields, the magnetizing ones are perfectly superimposed with those of the ZFC loops, pointing out that the enhancement of H_C is related to the presence of H_E. Therefore, classical macroscopic H_E theories are not fully valid for core|shell nanoparticles, [2,3,47] and more sophisticated theories such as perpendicular coupling must be considered. [3,48] Interestingly, previous results on highly anisotropic core|shell nanoparticles have revealed different types of exchange coupling phenomena. If in some cases no H_E has been observed and this is ascribed to the high anisotropy of both counterparts, [45,46,49] in some others moderate and large H_E values were reported, although the anisotropy of the materials involved was similarly large. [43,44] However, in our opinion, the high-quality structural matching between core and shell regions and a sharp interface are crucial issue to realize excellent exchange-coupled materials. Another remarkable effect of exchange bias is that of largely increasing the area of the hysteresis loop. Since the loop area corresponds to the energy losses in a full cycle and hence to the magnetic energy stored in the material, [50] we can argue that this effect can be a powerful tool on the way of building up RE-free permanent magnets (see discussion below).

The temperature dependence of FC hysteresis loops, measured for CS18 further elucidated the nature of the observed magnetic transitions (T_1 and T_2). In Figure 6.11-b the dependence of H_C and H_E with temperature is plotted: both H_C and H_E display a dramatic reduction as the temperature increases. In particular, while H_C approaches zero at room temperature, H_E vanishes at 210 K. This behavior is in good agreement with the description given above: H_C disappears close to the observed T_B when the FiM spinel shell becomes superparamagnetic; conversely, H_E vanishes above the ordering temperature of the AFM-core, confirming indirectly the interpretation of T_2 as T_N of the AFM-core region. [3]

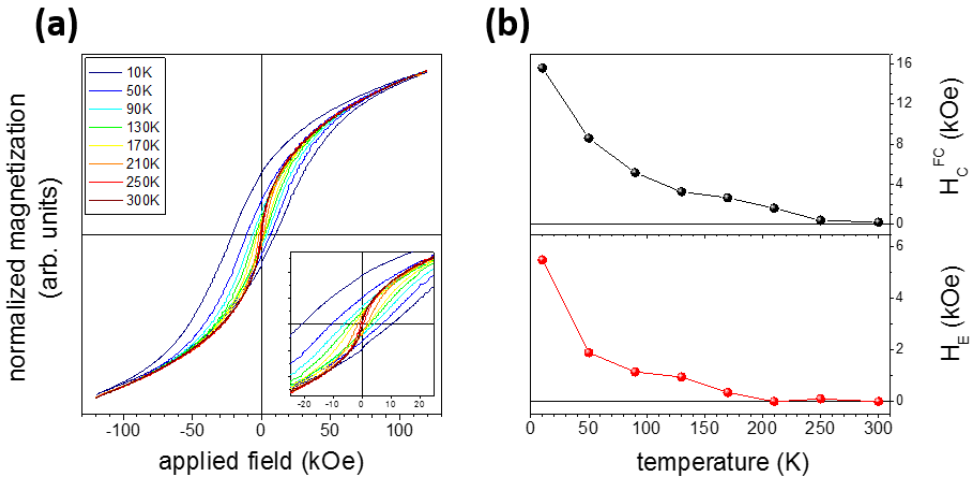

Figure 6.11: (a) CS18 hysteresis loops recorded at different temperature in a field range of ±120 kOe after a 120 kOe FC process from room temperature. (b) CS18 H_C^{FC} (black) and H_E (red) measured at different temperatures after a 120 kOe cooling process from room temperature.

Furthermore, the present series of AFM|FiM core|shell nanoparticles is an ideal candidate for a systematic analysis of the dependence of exchange-coupling effect on the size of the AFM core. In Figure 6.12 the dependencies of H_C and H_E as a function of the AFM-core diameter (d_{AFM}) are shown. Interestingly, both parameters show non-monotonic trend with d_{AFM}, as they exhibit a maximum for CS9 (d_{AFM} = 5 nm) and a subsequent decay to a value that remains constant for the two larger nanoparticles (CS15 and CS18).

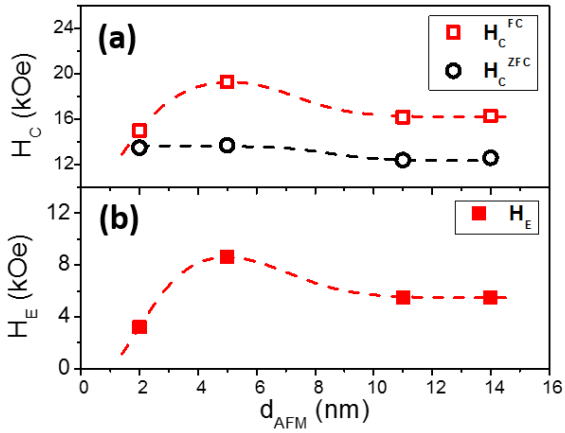

Figure 6.12: (a) H_C at 10 K as a function of d_{AFM}; H_C values have been obtained after FC at 120 kOe (red) or ZFC (black) process from room temperature. (b) H_E at 10 K as a function of d_{AFM} after FC at 120 kOe from room temperature. (The lines act as guides to the eyes).

Regarding H_E, its dependence is in good agreement with that theoretically predicted [3,51] and experimentally observed [3,52,53] in AFM|FM bilayers. The non-monotonic dependence can be understood by considering the concomitant effect of the energy barrier of the AFM material ($K_{AFM}V_{AFM}$) and the formation and growth of AFM domains, which are responsible for the onset and the maximum of H_E, respectively. [34,51] However, due to the reduced volume of our core|shell nanoparticles the formation and growth of AFM domains appears rather unlikely. An alternative explanation, recently proposed after some MonteCarlo simulations, suggests the competition between uncompensated spins of the core and shell regions as responsible of the H_E dependence in AFM|FiM core|shell nanoparticles. [54] Uncompensated spins, which comes mainly from the non-collinearity of the two AFM and FiM sublattices [55,56] and from structural defects, [57] have been demonstrated to be related to the exchange bias phenomena. [58] The non-monotonic dependence thus can be better attributed to a crossover in the relative number of uncompensated spins located in the FiM surface, i.e. the outer surface of the nanoparticles, or in the AFM-core/FiM-shell interface.

Also the H_C^{FC} dependence has been previously interpreted in terms of domain formation in highly anisotropic AFM materials [52] or of competition of uncompensated spins in the core|shell structure. [54] In our case, however, the maxima of H_C^{FC} and H_E occurs at the same d_{AFM}. This behavior, which is different from that reported in the literature for other exchange coupled systems where the maximum of H_C^{FC} is usually reached at lower size than H_E, clearly demonstrates that the increase of coercivity is driven by the presence of the induced bias in the demagnetizing branches of the loop. Therefore, the standard models which predict different trends for coercivity and exchange bias do not fully describe the behavior of AFM|FiM core|shell nanoparticles with high anisotropy of both components.

The evolution of the magnetic properties with the size of the AFM core provides precious information about the optimal relative amount of AFM and FiM (or ferromagnetic) phases to be combined to design an exchange-coupled permanent magnet. In our case, the relative increase of BH_{max} before and after the FC procedures, $BH_{max}^{FC}/BH_{max}^{ZFC}$, has the same non-monotonous trend observed for H_C and H_E ($BH_{max}^{FC}/BH_{max}^{ZFC}$ = 2, 7, 3, 1 for CS6, CS9, CS15 and CS18, respectively), confirming the strong effect of bias on the permanent magnet properties. More interestingly, we observed a very large increase of BH_{max} (more than 7 times for CS9), for a relatively low amount of AFM phase (ca. 20% in volume). Given the very low magnetization of AFM nanomaterials, [4] this aspect assumes a crucial relevance to preserve a high magnetic flux in the composite.

6.3 Oxidation of $Co_xFe_{1-x}O$(AFM)|$Co_xFe_{3-x}O_4$(FiM)

In the previous paragraph we have shown that thermal decomposition of ($Co^{2+}Fe^{3+}$)-oleate produces $Co_xFe_{1-x}O|Co_xFe_{3-x}O_4$ AFM|FiM core|shell nanoparticles with interesting magnetic properties, such as a remarkable H_E, as a consequence of both the quality of AFM-FiM interface and the high anisotropy of the constituent AFM and FiM phases. In addition, it has been observed that the formation the core|shell structure is driven by the oxidation of iron atoms, while the presence of cobalt ions has been revealed to be crucial to chemically stabilize the core|shell structure, avoiding the progressively oxidation process. Therefore, in order to better understand the role played by cobalt ions in the formation and stabilization of the core|shell nanostructures structure, the system was subjected to heating processes under air atmosphere in order to completely oxidize the core region. To this aim, 11 nm nanoparticles (sample M0) were synthesized following the previously reported procedure (section 6.1) setting a digestion temperature of 320 °C, and then were dispersed in 1-octadecene, heated up at 300 °C under a constant air bubbling and maintained for 5 min (M1) or 15 min (M2). It should be noted that large dwelling times led to the complete dissolution of the nanoparticles, probably due to the high temperature and the presence of oleic acid remaining onto nanoparticles surface.

First, TEM images were acquired to control the heated nanoparticles did not undergo relevant morphological transformation during the heating process. The micrographs (some selected examples are shown in Figure 6.13) demonstrates that the nanoparticles after the heating treatment maintain the same particle diameter and size distribution (11(1) nm) of the as-prepared sample.

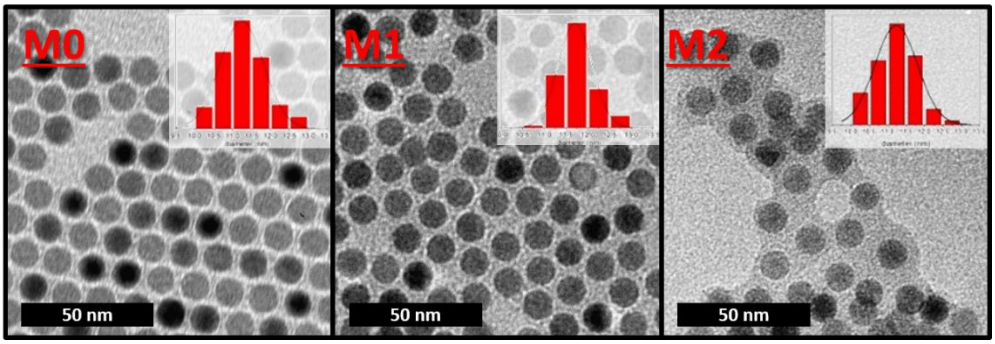

Figure 6.13: (*From the left*) TEM images and particle size histograms for nanoparticle of as-prepared sample core|shell nanoparticles (M0) and nanoparticles after the heating treatment (M1 and M2).

XRD analysis revealed that annealed samples do not have the pure spinel structure expected for completely oxidized nanoparticles. Indeed, samples M1 and M2 show a slightly modified diffraction pattern with respect to M0. The main observed discrepancy is the change in the relative intensity between the 2θ = 36-37° $(111)_{RS}$ and $(311)_S$ peaks from the rock-salt structure and spinel phases, respectively. The spinel peak intensity increases after the annealing process at expense of the $(111)_{RS}$ line, corroborating the growth of the spinel phase. On the other hand, all diffraction patterns are characterized by the main contribution of the $(220)_{RS}$ and $(200)_{RS}$ peaks at 2θ = 43° and 60° suggesting the nanoparticles maintain the same crystal structure after the treatment. Conversely, peaks related only to the spinel phase, i.e. $(311)_S$ and $(511)_S$, suffer a clear evolution narrowing and increasing in intensity, as expected for the growth of the more oxidized phase.

In addition, it can be observed that the diffractions peaks for the annealed samples present a clear shift towards larger angles, in agreement with the reduction of the cell parameters of both phases (see Table 6.3). Indeed, as extensively discussed in the previous paragraph, in sample M0 both structures have cell parameters strongly influenced by the extremely confined CS system, where the shell and the core suffer an expansion and contraction, respectively. Conversely, after annealing the cell parameter of the spinel phase decreases till it reaches the typical value of cobalt ferrite nanoparticles, [25] while that of the rock-salt slightly decreases in order to maintain a low mismatch between the two phases (0.1 %). The relative weight fraction obtained corroborated the increase of the spinel phase after the annealing process due to the oxidation of the inner rock-salt core (see Table 6.3). Finally, it should be noted that increasing the dwelling time (15 min, M2) does not substantially

modify the structure of the nanoparticles as all the parameters of both phases remain the same.

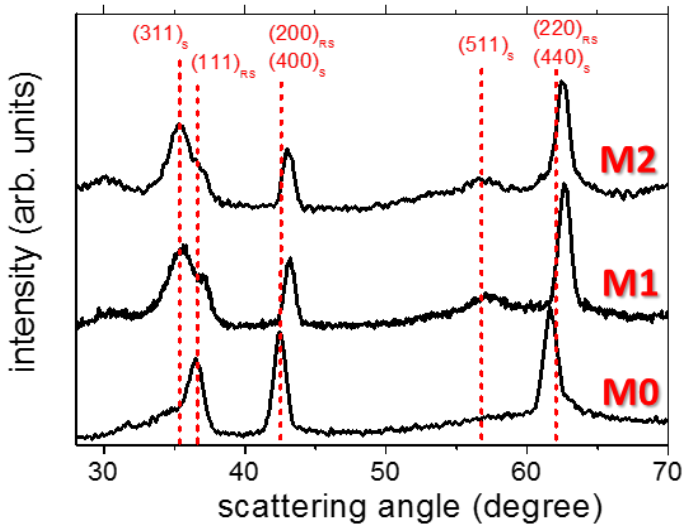

Figure 6.14: Powder XRD patterns for M0, M1 and M2 samples (indexed planes are labelled with RS and S for wüstite rock-salt and magnetite spinel structure, respectively).

Table 6.3: Cell parameter (*a*), crystal size (*D*) and phase amount (%) for rock-salt and spinel structure and lattice mismatch between the two phases.

	Rock-Salt phase (RS)			*Spinel phase (S)*			lattice mismatch (%)
	a_{RS} (nm)	D_{RS} (nm)	$\%_{RS}$ (w%)	a_S (nm)	D_S (nm)	$\%_S$ (w%)	
M0	0.422	19	33	0.842	5	67	0.1(1)
M1	0.419	16	20	0.838	7	80	0.0(1)
M2	0.420	15	18	0.838	7	82	0.1(1)

The composition of the nanoparticles was investigated through EELS analysis, performed by Giovanni Bertoni from CNR-IMEN of Parma (Italy) and Stuart Turner from the University of Antwerp (Belgium). Elemental quantification, reported in Figure 6.15, corroborates the expected $Co_{0.4}Fe_{0.6}O|CoFe_2O_4$ core|shell structure with non-homogeneous distribution of iron, cobalt and oxygen atoms along the nanoparticles diameter (see Fig. 3a) for M0 sample. Conversely, after the heating processes, EELS analysis revealed the loss of the core|shell structure with the complete oxidation of rock-salt to spinel phase. In fact, for M1 and M2 samples the M-O% (cobalt+iron and oxygen percentages) show a constant value along the nanoparticles, which matches the percentage expected for a pure spinel structure (M_3O_4). Moreover, EELS mapping shows an intermixed Fe^{2+}-Fe^{3+} ions in the whole nanoparticles. Furthermore, the distribution of Co and Fe experessed as percentage, along the

nanoparticles evolved from the step-like shape characteristic of the core|shell structure into a continuous gradual variation. In addition, it should be noted that cobalt percentages in M1 and M2 is considerably lower than in M0. The total amount of cobalt and iron in a whole nanoparticle evaluated by integrating the EELS signal of each samples confirms this behaviour: indeed a decrease of 25 % of the total cobalt amount was found in the heated samples.

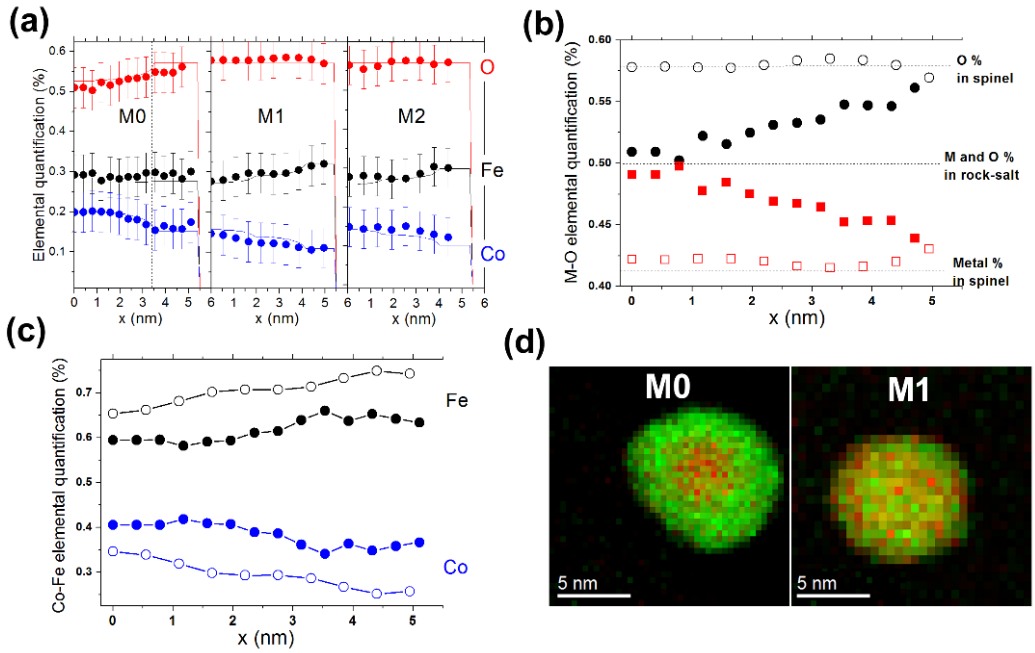

Figure 6.15: (a) Iron, cobalt and oxygen elemental quantification for samples M0, M1 and M2; (b) cobalt + iron, M, (circles) and oxygen, O, (squares) percentage for samples M0 (full symbols) and M1 (empty symbols); (c) bottom cobalt (blue) and iron (black) percentage for M0 (full symbols) and M1 (empty symbols); (d) Fe^{2+}/Fe^{3+} EELS mapping for s M0 and M1 samples, where green and red colors refers to Fe^{3+} and Fe^{2+}, respectively. Elemental quantification were performed along half nanoparticle.

Summarizing, the EELS analysis suggests the rock-salt to spinel oxidation occurs through Co^{2+} ions diffusion along the nanoparticles. Indeed, the oxygen deposition onto the nanoparticle surface, required for the oxidative process to occur, generates a potential gradient from the surface to the core region. [13,59] In addition, being the rock-salt phase a cation deficient non-stoichiometric oxides, [60,61] a cation ions diffusion through the vacancies could take place in order to maintain the particles electroneutrality during the oxygen deposition. [59] Therefore, as oxidation advances, a change in the cation density and, concomitantly, of the metal and oxygen percentage (M-O%) occurs leading to the observed graded evolution of Co-Fe% composition from the inner to outer region, while the characteristic sharp interface of core|shell nanoparticles is lost. In addition, it has to be

noted that the selective Co^{2+} ions diffusion during the oxidation process, which ends in a final depletion of cobalt content in the annealed nanoparticles, is in agreement with the required decrease in metal-to-oxygen and divalent-to-trivalent ions ratio. Indeed, as discussed above, because of the large difference in divalent metal ions reduction potentials, the phase evolution can occur only through a selective Fe^{2+} oxidation. Consequently, assuming a complete Fe^{2+} oxidation in the core, which has a $Co_{0.4}Fe_{0.6}O$ stoichiometry the amount of divalent cobalt ions (2/3 of total cations) is too large to stabilize the spinel structure (1/3 of divalent cations required, see figure Xxb); therefore the nanoparticles is forced to release this species in order to carry out the oxidation process. [62] This effect can also be observed in the as-prepared sample, where the cobalt-to-iron ratio decreases from the core to the shell region. Electron Paramagnetic Resonance experiment are currently underway in order to verify this hypothesis.

EELS analysis showed the oxidation occurs in the entire nanoparticles volume, while the XRD analysis suggests the presence of remaining rock-salt phase. In order to shed light on these contradictory indications, the local structure of the nanoparticles was further investigated through HR-TEM fast Fourier transforms (FFT) and their inverse ($_{inv}$FFT) analysis. Also this analysis was carried out by Giovanni Bertoni from CNR-IMEN of Parma (Italy). As expected, FFT images of M0 and M1 present both spots which can be related to the spinel and rock-salt phases (see Figure 6.16). [63,64]

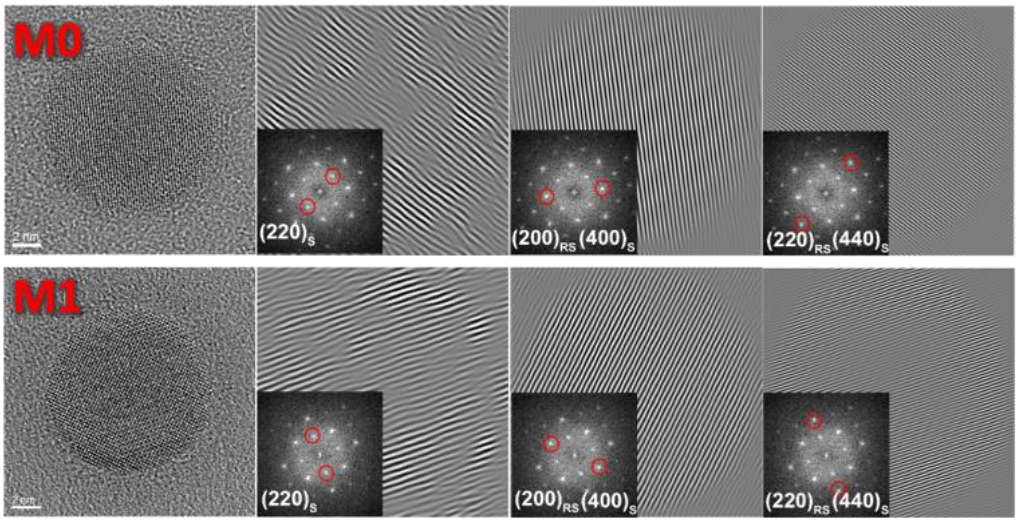

Figure 6.16: HR-TEM image and their respective $_{inv}$FFT for the $(220)_S$, $(200)_{RS}/(400)_S$ and $(220)_{RS}/(440)_S$ diffraction spots for sample M0 and M1.

The contribution of both phases can be separately studied: on one side considering the spots at 0.30 nm distance, which can be solely indexed as the spinel (220) planes, on the other the spots at 0.21 and 0.15 nm distances arising from the overlapping signals of (200)/(400) and (220)/(440) rock-salt/spinel planes. In particular, $_{inv}$FFT of (220) spinel spots for M0 presents a non-continuous structure in agreement with the shell morphology of the spinel

phase. Many dislocation defects can be observed in the image, corroborating the possible formation of antiphase boundaries previously shown in similar core|shell nanoparticles.[13] Conversely, both (200)/(400) and (220)/(440) rock-salt/spinel $_{inv}$FFT images display a well-defined structure in the entire nanoparticle without the presence of dislocation defects. The results obtained for M1 are similar: indeed, (200)/(400) and (220)/(440) rock-salt/spinel planes still present a well-defined structure along the whole nanoparticles. Conversely, (220) spinel fringes appear spread in the entire particle, i.e., the initial shell location is lost, showing a rather similar non-continuous structure with several defects. It has to be noted that the preservation of (200)/(400) and (220)/(440) rock-salt/spinel planes is in good agreement with what observed from XRD analysis. In addition, it suggests the nanoparticles oxidation occurs by topotaxial modification of pre-existing structure because of the reduced lattice misfit between the two oxygen RS and S sub-lattices, involving thus only a change in the distribution of the Co^{2+} cations. [65] Indeed, the oxidation process emerges to occurs by a topotaxial formation of the (400) and (440) spinel planes along the (200) and (220) rock-salt ones presenting equivalent structures where cations are intercalated in regular planar series at similar distances (see Figure 6.17). On the other hand, the spinel sub-lattices corresponding to the new planes has been revealed to present a high number of defects decreasing the overall spinel crystallinity.

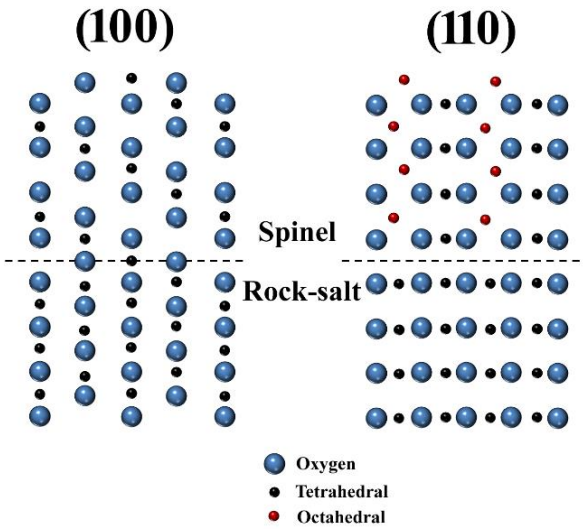

Figure 6.17: (100) and (110) planes for the rock-salt, spinel phases and their interface.

Finally, in order to average the information obtained in single nanoparticles, XMCD spectra at Fe and Co $L_{2,3}$ edges were recorded at low temperatures for sample M0 and M1. This experiment allowed for the verification of the oxidative process with a non-local experimental technique. As shown in Figure 6.18 it can be observed that for both samples the signal from cobalt ions remains almost unaltered showing the same profile of Co^{2+} ions in octahedral coordination. [66,67] However, looking at the Fe edge, while M0 shows the characteristics two peaks of the Fe^{2+} and Fe^{3+} in octahedral sites, the spectrum recorded for

the heated sample resembles that expected for a spinel structure where an extra peak appears corresponding to the Fe^{3+} in tetrahedral coordination. These observations strongly support the proposed oxidation mechanism.

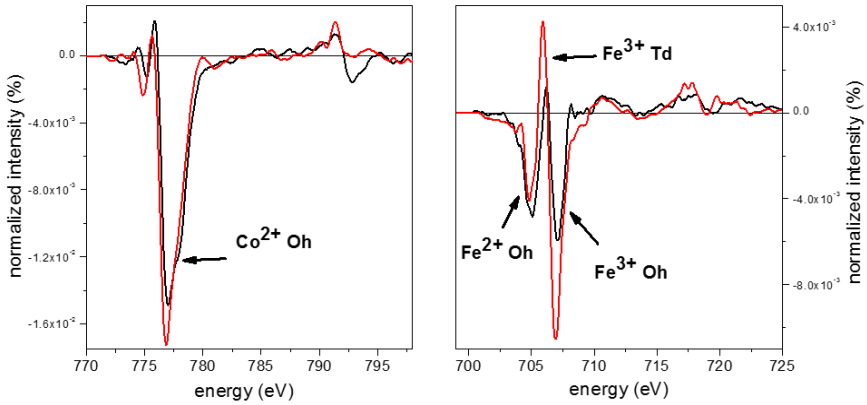

Figure 6.18: (a) Cobalt and (b) iron $L_{2,3}$ edges XMCD spectra for sample M0 and M1.

Summarizing, an oxidation process was applied to non-stoichiomtric core|shell cobalt ferrite nanoparticles to better understand the spinel shell formation in $Co_xFe_{1-x}O|Co_xFe_{3-x}O_4$ AFM|FiM core|shell nanoparticles. The structural characterization confirmed the presence of an oxidative process which results in the formation of a spinel phase through topotaxial modification along (200) and (220) planes of pre-existing rock-salt phase, explaining thus the good quality of the interfaces between the two phases that we obtained and thus the strong exchange-coupling interactions (see Figure 6.18). On the other hand, the formed spinel phase, despite of the perfect structural order along (400) and (440) planes, presents low crystallinity, which results from defects in spinel planes not present in the pristine rock-salt structure, e.g. (220) spinel plane. These defects are responsible for the low magnetization value of the system. Particularly, the presence of defects could arise from the ions rearrangement required for the achievement of the characteristic spinel stoichiometry. In addition, we found the Co^{2+} ions diffusion is a fundamental process for rock-salt to spinel oxidation. Therefore, the graded decrease of cobalt amount as well as its radial diffusion into the nanoparticles could hamper the spinel formation affecting its final crystallinity.

6.4 Conclusions

In summary, a series of narrowly size distributed $Co_{0.3}Fe_{0.7}O$(AFM)$|Co_{0.6}Fe_{2.4}O_4$(FiM) core|shell nanoparticles with mean diameter from 6 to 18 nm was synthesized through a one-pot thermal decomposition of a ($Co^{2+}Fe^{3+}$)-oleate precursor. The formation of the core|shell structure was obtained by topotaxial oxidation of the core region leading to a series of core|shell nanoparticles with variable AFM-core size and constant FiM-shell thickness. The excellent interphase matching and the well-defined core|shell morphology

and stoichiometry for all the series makes it a proper candidate for a systematic analysis of the exchange-coupling dependence on the AFM size in AFM|FiM core|shell nanoparticles. Accordingly, magnetic characterization has revealed ZFC hysteresis loops with large irreversible fields and H_C almost independent of particle size. In addition, upon field cooling the robust exchange-coupling between AFM and FiM phases was demonstrated to give rise to the largest values of H_E ever reported for core|shell nanoparticles (8.6 kOe) and to an enhanced H_C. The combination of these two effects leads to a significant increase of the energy stored in the material, even in a highly anisotropic material such as cobalt ferrite nanoparticles and for relatively low amount of AFM phase. Therefore, biasing is demonstrated to be a powerful strategy to improve the performance of RE- free permanent magnets. Interestingly, the FC process was found to affect the loop on the demagnetizing branches only, suggesting that classical macroscopic H_E theories do not accurately describes the behavior of high anisotropic core|shell nanoparticles. Both H_C^{FC} and H_E depict a non-monotonic trend with d_{AFM}, showing a maximum value at d_{AFM} = 5 nm. The observed trend for H_E was explained by the internal competition between uncompensated spins at the nanoparticles surface and core and shell interfaces.

Besides, more information about the mechanism underlying the surface oxidation of the nanoparticles was obtained by applying further oxidation stages. In particular, it was observed that the cobalt ferrite formation occurs from topotaxial modification of pre-existing cobalt and iron monoxide structure explaining the origin of the good quality interface between the two magnetic phases which, in turn, allows for a strong exchange-coupling interactions to occur, resulting in the observed large H_E.

References

[1] J.S. Jiang, A. Inomata, C. You, J.E. Pearson, S.D. Bader, Magnetic stability in exchange-spring and exchange-bias systems after multiple switching cycles, J. Appl. Phys. 89 (2001) 6817. doi:10.1063/1.1359787.

[2] W.H. Meiklejohn, C.P. Bean, New Magnetic Anisotropy, Phys. Rev. 102 (1956) 1413–1414. doi:10.1103/PhysRev.102.1413.

[3] J. Nogués, J. Sort, V. Langlais, V. Skumryev, S. Suriñach, J.S. Muñoz, et al., Exchange bias in nanostructures, Phys. Rep. 422 (2005) 65–117. doi:10.1016/j.physrep.2005.08.004.

[4] R.H. Kodama, S.A. Makhlouf, A.E. Berkowitz, Finite Size Effects in Antiferromagnetic NiO Nanoparticles, Phys. Rev. Lett. 79 (1997) 1393–1396. doi:10.1103/PhysRevLett.79.1393.

[5] J. Sort, S. Suriñach, J.S. Muñoz, M.D. Baró, J. Nogués, G. Chouteau, et al., Improving the energy product of hard magnetic materials, Phys. Rev. B. 65 (2002) 174420. doi:10.1103/PhysRevB.65.174420.

[6] F. Jimenez-Villacorta, L.H. Lewis, Advanced Permanent Magnetic Materials, in: J.M. Gonzalez Estevez (Ed.), Nanomagnetism, One Central Press, 2014: pp. 160–189.

[7] R.F.L. Evans, D. Bate, R.W. Chantrell, R. Yanes, O. Chubykalo-Fesenko, Influence of interfacial roughness on exchange bias in core-shell nanoparticles, Phys. Rev. B. 84 (2011) 092404. doi:10.1103/PhysRevB.84.092404.

[8] C. Leighton, J. Nogués, B.J. Jönsson-Åkerman, I.K. Schuller, Coercivity Enhancement in Exchange Biased Systems Driven by Interfacial Magnetic Frustration, Phys. Rev. Lett. 84 (2000) 3466–3469. doi:10.1103/PhysRevLett.84.3466.

[9] X. Sun, N.F. Huls, A. Sigdel, S. Sun, Tuning exchange bias in core/shell FeO/Fe3O4 nanoparticles., Nano Lett. 12 (2012) 246–51. doi:10.1021/nl2034514.

[10] A. Lak, M. Kraken, F. Ludwig, A. Kornowski, D. Eberbeck, S. Sievers, et al., Size dependent structural and magnetic properties of FeO-Fe3O4 nanoparticles., Nanoscale. 5 (2013) 12286–95. doi:10.1039/c3nr04562e.

[11] H. Khurshid, S. Chandra, W. Li, M.H. Phan, G.C. Hadjipanayis, P. Mukherjee, et al., Synthesis and magnetic properties of core/shell FeO/Fe3O4 nano-octopods, J. Appl. Phys. 113 (2013) 17B508. doi:10.1063/1.4794978.

[12] M. Estrader, A. López-Ortega, I. V Golosovsky, S. Estradé, A.G. Roca, G. Salazar-Alvarez, et al., Origin of the large dispersion of magnetic properties in nanostructured oxides: Fe(x)O/Fe3O4 nanoparticles as a case study., Nanoscale. 7 (2015) 3002–15. doi:10.1039/c4nr06351a.

[13] E. Wetterskog, C.W. Tai, J. Grins, L. Bergström, G. Salazar-Alvarez, Anomalous magnetic properties of nanoparticles arising from defect structures: topotaxial oxidation of Fe(1-x)O|Fe(3-δ)O4 core|shell nanocubes to single-phase particles., ACS Nano. 7 (2013) 7132–44. doi:10.1021/nn402487q.

[14] J. Park, K. An, Y. Hwang, J.-G. Park, H.-J. Noh, J.-Y. Kim, et al., Ultra-large-scale syntheses of monodisperse nanocrystals, Nat. Mater. 3 (2004) 891–895. doi:10.1038/nmat1251.

[15] S.G. Kwon, Y. Piao, J. Park, S. Angappane, Y. Jo, N.-M. Hwang, et al., Kinetics of monodisperse iron oxide nanocrystal formation by "heating-up" process., J. Am. Chem. Soc. 129 (2007) 12571–84. doi:10.1021/ja074633q.

[16] H.T. Hai, H.T. Yang, H. Kura, D. Hasegawa, Y. Ogata, M. Takahashi, et al., Size control and characterization of wustite (core)/spinel (shell) nanocubes obtained by decomposition of iron oleate complex., J. Colloid Interface Sci. 346 (2010) 37–42. doi:10.1016/j.jcis.2010.02.025.

[17] E. Fantechi, G. Campo, D. Carta, A. Corrias, C. de Julián Fernández, D. Gatteschi, et al., Exploring the Effect of Co Doping in Fine Maghemite Nanoparticles, J. Phys. Chem. C. 116 (2012) 8261–8270. doi:10.1021/jp300806j.

[18] G.C. Lavorato, E. Lima, D. Tobia, D. Fiorani, H.E. Troiani, R.D. Zysler, et al., Size effects in bimagnetic CoO/CoFe2O4 core/shell nanoparticles., Nanotechnology. 25 (2014) 355704. doi:10.1088/0957-4484/25/35/355704.

[19] R. Young, The Rietveld Method, Oxford University Press, 1993.

[20] N. Bao, L. Shen, W. An, P. Padhan, C. Heath Turner, A. Gupta, Formation Mechanism and Shape Control of Monodisperse Magnetic CoFe 2 O 4 Nanocrystals, Chem. Mater. 21 (2009) 3458–3468. doi:10.1021/cm901033m.

[21] R. Chen, M.G. Christiansen, P. Anikeeva, Maximizing hysteretic losses in magnetic ferrite nanoparticles via model-driven synthesis and materials optimization., ACS Nano. 7 (2013) 8990–9000. doi:10.1021/nn4035266.

[22] N.W. Denton, A. R. and Ashcroft, Vegard's law, Phys. Rev. A. 43 (1991) 3161–3164. doi:http://dx.doi.org/10.1103/PhysRevA.43.3161.

[23] S.B. Pongsai, Computational study on thermodynamics of mixing and phase behaviour for CoO/FeO and CoO/MnO solid solutions, J. Mol. Struct. 761 (2006) 171–175. doi:10.1016/j.theochem.2005.12.031.

[24] R.L. Clendenen, Lattice Parameters of Nine Oxides and Sulfides as a Function of Pressure, J. Chem. Phys. 44 (1966) 4223. doi:10.1063/1.1726610.

[25] A. López-Ortega, E. Lottini, C.D.J. Fernández, C. Sangregorio, Exploring the Magnetic Properties of Cobalt-Ferrite Nanoparticles for the Development of a Rare-Earth-Free Permanent Magnet, Chem. Mater. 27 (2015) 4048–4056. doi:10.1021/acs.chemmater.5b01034.

[26] J.C. Bean, L.C. Feldman, A.T. Fiory, S. Nakahara, I.K. Robinson1, GexSi1−x/Si strained-layer superlattice grown by molecular beam epitaxy, J. Vac. Sci. Techno. A. 2 (1984) 436. doi:10.1116/1.572361.

[27] B.B.P.B. Pichon, O. Gerber, C. Lefevre, I. Florea, S. Fleutot, W. Baaziz, et al., Microstructural and Magnetic Investigations of Wüstite-Spinel Core-Shell Cubic-Shaped Nanoparticles, Chem. Mater. 23 (2011) 2886–2900. doi:10.1021/cm2003319.

[28] C. Chen, R.-K. Chiang, H. Lai, C. Lin, Characterization of Monodisperse Wüstite Nanoparticles following Partial Oxidation, J. Phys. Chem. C. 114 (2010) 4258–4263. doi:10.1021/jp908153y.

[29] C.-J. Chen, R.-K. Chiang, S. Kamali, S.-L. Wang, Synthesis and controllable oxidation of monodisperse cobalt-doped wüstite nanoparticles and their core-shell stability and exchange-bias stabilization., Nanoscale. 7 (2015) 14332–43. doi:10.1039/c5nr02969d.

[30] M. Estrader, A. López-Ortega, S. Estradé, I. V Golosovsky, G. Salazar-Alvarez, M. Vasilakaki, et al., Robust antiferromagnetic coupling in hard-soft bi-magnetic core/shell nanoparticles., Nat. Commun. 4 (2013) 2960. doi:10.1038/ncomms3960.

[31] M. Sytnyk, R. Kirchschlager, M.I. Bodnarchuk, D. Primetzhofer, D. Kriegner, H. Enser, et al., Tuning the Magnetic Properties of Metal Oxide Nanocrystal Heterostructures by Cation Exchange, Nano Lett. 13 (2013) 586–593. doi:10.1021/nl304115r.

[32] A. Franco, F.C. e Silva, High temperature magnetic properties of cobalt ferrite nanoparticles, Appl. Phys. Lett. 96 (2010) 172505. doi:10.1063/1.3422478.

[33] X.S. Liu, B.X. Gu, W. Zhong, H.Y. Jiang, Y.W. Du, Ferromagnetic/antiferromagnetic exchange coupling in SrFe 12 O 19 /CoO composites, Appl. Phys. A. 77 (2003) 673–676. doi:10.1007/s00339-002-1762-4.

[34] G. Salazar-Alvarez, J. Sort, S. Suriñach, M.D. Baró, J. Nogués, Synthesis and size-dependent exchange bias in inverted core-shell MnO|Mn3O4 nanoparticles., J. Amer. Chem. Soc. 129 (2007) 9102–8. doi:10.1021/ja0714282.

[35] C.P. Bean, J.D. Livingston, Superparamagnetism, J. Appl. Phys. 30 (1959) S120. doi:10.1063/1.2185850.

[36] A.E. Berkowitz, K. Takano, Exchange anisotropy — a review, J. Magn. Magn. Mater. 200 (1999) 552–570. doi:10.1016/S0304-8853(99)00453-9.

[37] H. P. J. Wijn, Landolt-Börnstein - Numerical Data and Functional Relationships in Science and Technology, Vol. III/27G (Various Other Oxides), Springer-Verlag, Berlin/Heidelberg, 1992. doi:10.1007/b46090.

[38] M.A. Boubel, R.P. Mainard, H.G. Fousse, A.J. Pointon, F.R. Jeannot, The specific heat anomaly of solid solutions of isostructural antiferromagnetic oxides (pFeO—qCoO), Phys. Status Solidi (a). 35 (1976) 459–464. doi:10.1002/pssa.2210350206.

[39] P. Bracconi, Molecular-field treatment of the high temperature susceptibility and Néel temperature of type II antiferromagnetic solid-solutions xNiO−(1−x)CoO, J. Magn. Magn. Mater. 40 (1983) 37–47. doi:10.1016/0304-8853(83)90008-2.

[40] P. Mallick, N. C. Mishra, Evolution of Structure, Microstructure, Electrical and Magnetic Properties of Nickel Oxide (NiO) with Transition Metal ion Doping, Am. J. Mater. Sci. 2 (2012) 66–71. doi:10.5923/j.materials.20120203.06.

[41] M.F. Casula, P. Floris, C. Innocenti, A. Lascialfari, M. Marinone, M. Corti, et al., Magnetic Resonance Imaging Contrast Agents Based on Iron Oxide Superparamagnetic Ferrofluids, Chem. Mater. 22 (2010) 1739–1748. doi:10.1021/cm9031557.

[42] J. Nogués, I.K. Schuller, Exchange bias, J. Magn. Magn. Mater. 192 (1999) 203–232. doi:10.1016/S0304-8853(98)00266-2.

[43] M.I. Bodnarchuk, M. V Kovalenko, H. Groiss, R. Resel, M. Reissner, G. Hesser, et al., Exchange-coupled bimagnetic wüstite/metal ferrite core/shell nanocrystals: size, shape, and compositional control., Small. 5 (2009) 2247–52. doi:10.1002/smll.200900635.

[44] W. Baaziz, B.P. Pichon, Y. Liu, J.-M. Grenèche, C. Ulhaq-Bouillet, E. Terrier, et al., Tuning of Synthesis Conditions by Thermal Decomposition toward Core–Shell CoxFe1– xO@CoyFe3– yO4 and CoFe2O4 Nanoparticles with Spherical and Cubic Shapes, Chem. Mater. 26 (2014) 5063–5073. doi:10.1021/cm502269s.

[45] G.C. Lavorato, E. Lima, H.E. Troiani, R.D. Zysler, E.L. Winkler, Exchange-coupling in thermal annealed bimagnetic core/shell nanoparticles, J. Alloy. Compd. 633 (2015) 333–337. doi:10.1016/j.jallcom.2015.02.050.

[46] E.L. Winkler, E. Lima, D. Tobia, M.E. Saleta, H.E. Troiani, E. Agostinelli, et al., Origin of magnetic anisotropy in ZnO/CoFe2O4 and CoO/CoFe2O4 core/shell nanoparticle systems, Appl. Phys. Lett. 101 (2012) 252405. doi:10.1063/1.4771993.

[47] W.H. Meiklejohn, Exchange Anisotropy—A Review, J. Appl. Phys. 33 (1962) 1328. doi:10.1063/1.1728716.

[48] T.C. Schulthess, W.H. Butler, Consequences of Spin-Flop Coupling in Exchange Biased Films, Phys. Rev. Lett. 81 (1998) 4516–4519. doi:10.1103/PhysRevLett.81.4516.

[49] E. Lima, E.L. Winkler, D. Tobia, H.E. Troiani, R.D. Zysler, E. Agostinelli, et al., Bimagnetic CoO Core/CoFe2O4 Shell Nanoparticles: Synthesis and Magnetic Properties, Chem. Mater. (2012) 2–6.

[50] J.M.D. Coey, Magnetism and Magnetic Materials, Cambridge University Press, New York, 2010. www.cambridge.org/9780521816144.

[51] A.P. Malozemoff, Heisenberg-to-Ising crossover in a random-field model with uniaxial anisotropy, Phys. Rev. B. 37 (1988) 7673–7679. doi:10.1103/PhysRevB.37.7673.

[52] M. Ali, C.H. Marrows, B.J. Hickey, Onset of exchange bias in ultrathin antiferromagnetic layers, Phys. Rev. B. 67 (2003) 172405. doi:10.1103/PhysRevB.67.172405.

[53] Z. Shi, J. Du, S.-M. Zhou, Exchange bias in ferromagnet/antiferromagnet bilayers, Chin. Phys. B. 23 (2014) 027503. doi:10.1088/1674-1056/23/2/027503.

[54] M. Vasilakaki, K.N. Trohidou, J. Nogués, Enhanced magnetic properties in antiferromagnetic-core/ferrimagnetic-shell nanoparticles., Sci .Rep. 5 (2015) 9609. doi:10.1038/srep09609.

[55] J.T. Richardson, D.I. Yiagas, B. Turk, K. Forster, M. V. Twigg, Origin of superparamagnetism in nickel oxide, J. Appl. Phys. 70 (1991) 6977. doi:10.1063/1.349826.

[56] P. Miltényi, M. Gierlings, J. Keller, B. Beschoten, G. Güntherodt, U. Nowak, et al., Diluted Antiferromagnets in Exchange Bias: Proof of the Domain State Model, Phys. Rev. Lett. 84 (2000) 4224–4227. doi:10.1103/PhysRevLett.84.4224.

[57] K. Takano, R.H. Kodama, A.E. Berkowitz, W. Cao, G. Thomas, Interfacial Uncompensated Antiferromagnetic Spins: Role in Unidirectional Anisotropy in Polycrystalline Ni81Fe19/CoO Bilayer, Phys. Rev. Lett. 79 (1997) 1130–1133. doi:10.1103/PhysRevLett.79.1130.

[58] S. Roy, M.R. Fitzsimmons, S. Park, M. Dorn, O. Petracic, I. V. Roshchin, et al., Depth Profile of Uncompensated Spins in an Exchange Bias System, Phys. Rev. Lett. 95 (2005) 047201. doi:10.1103/PhysRevLett.95.047201.

[59] T. Maruyama, M. Ueda, Void Formation Induced by the Divergence of the Diffusive Ionic Fluxes in Metal Oxides Under Chemical Potential Gradients, J. Korean Ceram. Soc. 47 (2009) 8–18.

[60] M. MARTIN, Impurity diffusion of iron in cobalt oxide, Solid State Ionics. 28-30 (1988) 1230–1234. doi:10.1016/0167-2738(88)90362-1.

[61] M. Backhaus-Ricoult, R. Dieckmann, Defects and Cation Diffusion in Magnetite (VII): Diffusion Controlled Formation of Magnetite During Reactions in the Iron-Oxygen System, Berichte Der Bunsengesellschaft Für Phys. Chemie. 90 (1986) 690–698. doi:10.1002/bbpc.19860900814.

[62] R.M. Hazen, R. Jeanloz, Wüstite (Fe1-xO): A review of its defect structure and physical properties, Rev. Geophys. Sp. Phys. 22 (1984) 37 – 46. doi:10.1029/RG022i001p00037.

[63] E. Lottini, A. López-Ortega, G. Bertoni, S. Turner, M. Meledina, G. Van Tendeloo, et al., One-pot synthesis of strongly exchange coupled CoreShell nanoparticles with high magnetic anisotropy - Submitted, Submitted. (n.d.).

[64] A. López-Ortega, M. Estrader, G. Salazar-Alvarez, S. Estradé, I. V Golosovsky, R.K. Dumas, et al., Strongly exchange coupled inverse ferrimagnetic soft/hard, MnxFe3−xO4/FexMn3−xO4, core/shell heterostructured nanoparticles, Nanoscale. 4 (2012) 5138. doi:10.1039/c2nr30986f.

[65] S.R. Summerfelt, C.B. Carter, The movement of the spinel-NiO interface in thin films, Ultramicroscopy. 30 (1989) 150–156. doi:10.1016/0304-3991(89)90182-4.

[66] S.H. Oh, R.H. Shin, C. Lefèvre, A. Thomasson, F. Roulland, Y. Shin, et al., Incorporation of cobalt ions into magnetoelectric gallium ferrite epitaxial films: tuning of conductivity and magnetization, RSC Adv. 5 (2015) 34265–34271. doi:10.1039/C5RA03609G.

[67] J.. Hochepied, P. Sainctavit, M.. Pileni, X-ray absorption spectra and X-ray magnetic circular dichroism studies at Fe and Co L2,3 edges of mixed cobalt–zinc ferrite nanoparticles: cationic repartition, magnetic structure and hysteresis cycles, J. Magn. Magn. Mater. 231 (2001) 315–322. doi:10.1016/S0304-8853(01)00182-2.

Chapter 7

Conclusions and perspectives

The experimental work here presented is focused on the design of novel RE-free magnetic nanostructures for permanent magnet applications. To this aim, different strategies were exploited in order to better understand the correlation between the nanostructure and the material performances as permanent magnet. In particular, both single-phase nanoparticles and exchange-coupled bi-magnetic nanocomposites based on transition metal oxides (iron, cobalt, manganese and zinc oxides) were investigated, showing magnetic properties evolving with composition, structure, size and shape of the material.

First, thermal decomposition synthetic procedure was optimized for the preparation of monodisperse cobalt ferrite nanocrystals with average size distributed over a broad range. In particular, varying the metal precursor, the heating rate and the digestion time, a family of cobalt ferrite nanoparticles from 4 to 60 nm were synthesized through OA and OAm assisted thermal decomposition. The used synthetic approach provided the formation of nanoparticles with narrow size distribution, high crystallinity and controlled shape and stoichiometry allowing an accurate study of their size/shape-dependent evolution of magnetic properties. We found that cobalt ferrite nanoparticles present almost constant M_S and M_R values close to the bulk counterpart. Conversely H_C and K_{eff} depict a non-monotonic behaviour with two different maxima at low and room temperature. We explained the observed behaviour as originating from a combination of crossover on magnetic coherent/non-coherent rotation and/or shape induced demagnetization effect, which are responsible for the maximum at low temperature. On the other hand, thermal fluctuations of the blocked moment across the anisotropy energy barrier, being more important at lower size and higher temperature, lead to the H_C maximum shift to larger particle size at room temperature. In order to assess the suitability of the obtained cobalt ferrite nanoparticles as permanent magnet, the $(BH)_{max}$ energy product was evaluated. Interestingly, we found the maximum value ever reported in the literature for cobalt ferrite nanoparticles at room temperature, i.e. 2.1 MGOe (18 kJm^{-3}) for 40 nm NPs. Moreover, this investigation allowed us to establish, at least on the basis of $(BH)_{max}$, the potentiality of also single-phase cobalt ferrite nanoparticles alone, for the realization of RE-free permanent magnets

to be used in the intermediate region of the energy product map, where the latter are currently employed simply because standard ferrites do not have large enough $(BH)_{max}$. Indeed, if the possibility of compacting and orienting the magnetic anisotropy axes of the nanograins is taken into account, $(BH)_{max}$ as large as 8 MGOe (60 kJm^{-3}) can be in principle obtained, which is close to doubling the values achievable with standard transition metal based ferrites. Furthermore, by playing with the many parameters that define the physical properties of matter at the nanoscale, a further improvement of $(BH)_{max}$ can be envisaged. To this aim several strategies can be considered, such as increasing the particle magnetic moment through the control of the inversion degree of Co^{2+} ions in the spinel lattice, or by doping with diamagnetic divalent ions (e.g., Zn^{2+}). On the other hand, the presented nanoparticles are an excellent building block to design exchange-coupled systems with enhanced energy product.

Therefore, starting from these promising results, we decided to prepare hard|soft exchange-coupled magnetic nanoparticles. As a first attempt, the *seed-mediated* thermal decomposition procedure was investigated to synthesize hard|soft ferrites-based core|shell nanoparticles. In particular, varying the metal precursor concentration of the shell we found the propret conditions to avoid the homogeneous nucleation, i.e. the formation of pure soft magnetic phase nanoparticles, in favour of heterogeneous nucleation of the soft phase onto pre-synthesized cobalt ferrite seeds. In addition, the establishment of a coherent interface between core and shell regions were achieved resulting in the formation of high exchange-coupled systems. In fact, the magnetic characterization showed a softening of the composite (decrease of H_C, R and K_{eff}) as shell thickness was increased, confirming the obtainment of exchange-coupled hard|soft core|shell nanoparticles. Although, because of the similar magnetic moment of the constituent phase phases, the material softening was not accompanied by a sufficient increase in magnetization values able to increase the energy product, our results demonstrate that thermal decomposition is a viable technique to growth this kind of exchange couple nanosystems . Most importantly, we manage to synthesize core|shell nanoparticles with a high degree of exchange coupling, starting from large seeds, a mandatory requirement to fully exploit the properties of the hard core.

In order to prepare nanocrystals with larger M_S values to be used as soft phase, the thermal decomposition synthesis of manganese-zinc ferrite was investigated. Unfortunately, synthetic attempts demonstrated a decrease in crystallinity and purity of formed soft phase as the manganese and zinc amount is increased to achieve the $Mn_{0.6}Zn_{0.4}Fe_2O_4$ stoichiometry, corresponding to the largest magnetization values among ferrities. Indeed, the higher M_S we obtained, practically resembled that of pure magnetite nanoparticles and was provided by poorly doped ferrite nanoparticles ($Mn_{0.2}Zn_{0.1}Fe_{2.7}O_4$). Although, we do not have any conclusive explanation about this unexpected behaviour we can argue that the slower nucleation kinetics of manganese and zinc precursors or of their reaction intermediates, is the responsible for the poor crystallinity and the presence of satellite phases in the obtained nanoparticles. However, since both the presence of Mn^{2+} and Zn^{2+} ions and high nanoparticles crystallinity are required in order to obtain ferrites with large magnetic moment, further investigations would be necessary in order to prepare ferrite-based hard|soft exchange coupled systems for high performance RE-free permanent magnets applications. For this purpose, a possible strategy leading to incremental improvement of cobalt ferrite nanoparticles performances could the separation of

the Zn^{2+} and Mn^{2+} doping process in order to separately assess the optimal condition to achieve high crystalline nanoparticles. Indeed, the obtainment of $Mn_{0.6}Zn_{0.4}Fe_2O_4$ nanocrystal could be carried out through a first optimization of the synthesis of crystalline Zn-doped cobalt ferrite nanoparticles and a subsequent substitution of Co^{2+} ions with Mn^{2+} ones.

Among the possible alternative strategies for hard|soft nanocomposite production, we explored the partial reduction of hard magnetic oxides to their metallic form. Besides being a promising approach this method is appealing since in principle it can b easily scale up to the production of large amount of material. In particular, a series of exchange-coupled hard-soft $CoFe_2O_4$-FeCo nanocomposites, prepared through H_2 reduction of pre-synthesized cobalt ferrite nanoparticles, were investigated. The series of samples revealed improved magnetic performances with respect to the single-phase hard magnetic material. In particular, we observed a material softening as the amount of soft phase and the coupling degree between the two phases increase. In this case, because of the remarkably large magnetic moment of the FeCo phase, we observed a large enhancement of $(BH)_{max}$ (up to ten times with respect to the pre-synthesized cobalt ferrite nanoparticles) despite of the strong reduction of H_C. Nevertheless, we observed the largest $(BH)_{max}$ value for the weakly coupled nanocomposites. This experimental observation was explained in terms of the presence of a well-defined hard-soft interfaces assuring strong exchange coupling and facilitating the magnetization reversal though wall motion. Accordingly, a collapse in H_C and M_R occurred decreasing $(BH)_{max}$ of the nanocomposite. This interpretation was corroborated by MonteCarlo simulations. From this investigation we can then conclude that the optimization of the coupling degree is a fundamental parameter to optimize the material performances for developing RE-free permanent magnets.

Finally, exchange-coupling interactions based on exchange-bias were considered as an alternative strategy for the development of RE-free permanent magnets. Indeed, exchange-bias can lead to a concomitant increase in both H_C and M_R of the FiM and the combination of these two effects leads to a significant increase of the energy which can be stored in the material. However, in order to optimize the system for permanent magnet applications it is necessary to minimize the amount of AFM phase, which lowers the magnetization value of the final composites. Accordingly, exchange-coupled core|shell nanoparticles composed of high anisotropic FiM and AFM phases (non-stoichiometric cobalt ferrite and mixed iron-cobalt monoxides, respectively) were investigated. A series of narrowly size distributed $Co_{0.3}Fe_{0.7}O$-(AFM)|$Co_{0.6}Fe_{2.4}O_4$-(FiM) core|shell nanoparticles with constant FiM-shell thickness and variable AFM-core diameter were synthesized through a one-pot thermal decomposition of a ($Co^{2+}Fe^{3+}$)-oleate precursor. The formation of the core|shell structure was investigated by applying further oxidation stages. In particular, it was observed that the cobalt ferrite formation occurs from topotaxial modification of pre-existing cobalt and iron monoxide structure explaining the origin of the good quality interface between the two magnetic phases which, in turn, allows for a strong exchange-coupling interactions to occur.

The magnetic characterization revealed ZFC hysteresis loops with large irreversible fields and H_C almost independent of the particle size. In addition, upon field cooling the robust exchange-coupling between AFM and FiM phases was demonstrated to give rise to the largest values of H_E ever reported for core|shell nanoparticles (8.6 kOe) and to an enhanced H_C. Both H_C^{FC} and H_E

depict a non-monotonic trend with d_{AFM}, showing a maximum value at d_{AFM} = 5 nm, which was explained by the internal competition between uncompensated spins in the nanoparticles surface and core and shell interfaces. Importantly, core|shell nanoparticle presents significant H_E for remarkably small AFM size allowing the presence of only a small amount of AFM phase to improve the magnetic properties of the FiM one for permanent magnet applications. This was explained in terms of both the high anisotropic materials composing the core and shell regions and the high quality interface between the two magnetic phases facilitating the establishment of exchange-coupling interactions. In addition, the relative increase of $(BH)_{max}$ due to the presence of exchange-bias, quantified as the ratio between the values recorded after and before the FC procedures, presented the same non-monotonous trend observed for H_C and H_E with an increase of more than seven times the ZFC value for a relatively low amount of AFM phase (ca. 20% in volume). Given the very low magnetization of AFM nanomaterials, this aspect assumes a crucial relevance to preserve a high magnetic flux in the composite.

Concluding, different variations of nanostructures were analysed as potential strategies to optimize RE-free magnetic materials improving their performances for permanent magnet application. It emerged that, even if nano-sized hard magnetic phases such as cobalt ferrite show enhanced properties with respect to the bulk counterpart, particles orientation or surface modification (interfacial contact of magnetic phase with different properties) are required in order to achieve nanostructured material with desired $(BH)_{max}$ to replace low-performance RE-based permanent magnets. Moreover, we demonstrated that exchange-coupling between cobalt ferrite and soft FM or FiM could be a suitable strategies for permanent magnets production as long as the soft phase presents significantly larger M_S respect to cobalt ferrites. In addition, a proper optimization of the exchange-coupling degree should be considered in order to avoid an excessive softening of the magnetic material lowering the final performances as permanent magnet. Besides, the exchange-coupling between cobalt ferrite and AFM phase showed interesting evolution of nanocomposites magnetic properties, with a notably large increase of $(BH)_{max}$ as exchange-bias manifests. Importantly, we observed the use of high anisotropic materials and the high quality interface are key aspects to be considered in order to improve the material performances with considerably low AFM phases.

Appendix

Starting materials and chemicals

Metal-doped ferrites nanoparticles ($M_xFe_{3-x}O_4$, M = Co^{2+}, Mn^{2+}, Zn_{2+}) were synthesized using standard airless procedures and commercially available reagents. Benzyl ether (Bz_2O, 98%), lauric acid (LA, 98%), oleic acid (OA, 90%), oleylamine (OAm, >70%), 1,2-hexadecanediol (HDD, 90%), iron(III) acetylacetonate ($Fe(acac)_3$, ≥99%), cobalt(II) acetylacetonate ($Co(acac)_2$, ≥99%), manganese(II) acetylacetonate ($Mn(acac)_2$, ≥99%), zinc acetylacetonate ($Zn(acac)_2$, ≥99%), cobalt(II) chloride anhydrous ($CoCl_2$, ≥99%), manganese(II) chloride anhydrous ($MnCl_2$, ≥99%), zinc(II) chloride anhydrous ($ZnCl_2$, ≥98%). All starting materials were purchased from Sigma-Aldrich and used without further purification. $CoCl_2$ anhydrous was stored inside a glovebox.

The synthesis of cobalt and iron oxides core|shell nanoparticles ($Co_xFe_{1-x}O|Co_xFe_{3-x}O_4$) was carried out using standard airless procedures and commercially available reagents: 1-octadecene (ODE, 90%), docosane (DCE, 99%), ethanol (EtOH, >99.8%), hexane (Hx, >95%), oleic acid (OA, 90%), sodium oleate (NaOl, >97.0%), iron(III) chloride hexahydrate ($FeCl_3 \cdot 6H_2O$, >98%), cobalt(II) chloride hexahydrate ($CoCl_2 \cdot 6H_2O$, >98%). All starting materials were purchased from Sigma-Aldrich, except sodium oleate that was acquired from TCI America, and used without further purification.

Instrumentation

The characterization of nanoparticles synthesized in this work required the use of several techniques in order to investigate morphological, compositional and structural features, as well as the magnetic properties.

Transmission Electron Microscopy (**TEM**) analysis were performed at CE.M.E. (ICCOM-CNR) using a CM12 PHILIPS transmission electron microscope with a LaB_6 filament operating at 100 kV. Recorded images were further analysed with the ImageJ software. As for following

microscopic analysis, the nanoparticles were dispersed in hexane and then placed drop wise onto a carbon supported grid.

High Resolution High Angle Annular dark field images (**HAADF**) were acquired by Giovanni Bertoni and Stuart Turner at EMAT (University of Antwerp) on a FEI Titan FEI X-Ant-EM 'cubed' microscope equipped with a probe aberration corrector (probe size 0.08 nm, convergence 22 mrad, inner detector angle 50 mrad) operated at 300 kV. Simulated HAADF images on the core/shell particle were obtained with STEM_CELL using linear approximation, [1] taking into account the detector collecting angle (50 mrad – 180 mrad) and the nominal probe size (0.08 nm).

High Resolution Transmission Electron Microscopy images (**HR-TEM**) were acquired in collaboration with Giovanni Bertoni at IMEM-CNR on a JEOL JEM-2200FS operated at 200 keV. The analysis were performed setting the spherical aberration to a small negative value (~ -30 μm) to obtain a low delocalization and a high phase contrast transfer at high frequencies, and by filtering the elastic signal with the Ω-filter to further increase contrast. Electron Energy Loss Spectroscopy (**EELS**) was performed on the same instrument with the filter in spectroscopy mode. The quantification of O-K, Fe-$L_{2,3}$, and Co-$L_{2,3}$ were performed using EELSMODEL, by using a Likelihood derived fitter algorithm for Poisson statistics, to assure the highest possible accuracy and precision. [2] High resolution EEL maps for Fe valence were obtained at 120 kV with a Gatan Enfinium SR spectrometer and by exciting the monochromator, to reach an energy resolution of ~0.25 eV in the Fe-$L_{2,3}$ edge. Fe^{2+} and Fe^{3+} maps were obtained by fitting reference spectra to the acquired spectrum image. The simulations of the core/shell structure and the EEL profiles were done assuming a perfect match between wustite core and magnetite shell, and a full occupancy at the atomic sites.

Helium Ion Microscopy (**HIM**) analysis was performed at Consorzio GRINT (Empoli, FI) using an Orion Plus™ (Carl Zeiss) equipped with an Everhart-Thornley detector. Images were acquired in secondary electron mode with an acceleration voltage of 35 kV with a probe current ranging from 0.3 to 1.0 pA.

X-Ray Fluorescence (**XRF**) were performed at CRIST (Università degli Studi di Firenze). The determination of cobalt and iron concentration in the sample was performed using a Rigaku ZSX Primus spectrometer.

The microstructure of the nanoparticles was investigated by powder X-Ray Diffraction (**XRD**) using a Bruker New D8 ADVANCE ECO diffractometer equipped with a Cu Kα radiation and operating in θ–2θ Bragg Brentano geometry at 40kV and 40mA located at CRIST (Università degli Studi di Firenze). The measurements were carried out in the range 25-70°, with a step size of 0.03° and a collection time of 1.5 s. Quantitative analysis of the XRD data was performed with a full pattern fitting procedure based on the fundamental parameter approach (Rietveld method) [3] using Topas 2.0 (Bruker AXS) or Maud [4] software.

X-ray Absorption Spectroscopy (**XAS**) X-ray and magnetic Circular Dichroism (**XMCD**) measurements were performed at the Circular Polarization (CiPo) line of ELETTRA synchrotron radiation facility (Trieste). XAS and XMCD spectra were recorded at the Fe-$L_{2,3}$ and Co-$L_{2,3}$ edges using total electron yield mode at 10 K at high magnetic field. The XMCD signal was normalized by the area of the XAS spectra after correcting for the background. XAS and XMCD measurements were performed on nanoparticles placed drop wise onto a carbon supported grid.

The magnetic properties of the samples were measured on tightly packed powdered samples using vibrating sample mode (VSM) magnetometer with 120 kOe (MagLab VSM12T-Oxford) and 90 kOe (VSM option on Quantum Design PPMS) maximum field located at LAMM (Università degli Studi di Firenze). Magnetization versus temperature measurements were performed in zero-field cooled (ZFC) and field cooled (FC) conditions with 50 Oe or 30 kOe probe fields. Hysteresis loops were measured in ZFC or FC conditions after cooling from room temperature to the desired temperature with an applied field corresponding to the maximum value of the investigated field range. AC susceptibility measurements were performed using a SQUID magnetometer (Quantum Design) working in the 0.1-1000 Hz frequency range.

References:

[1] G. Bertoni, V. Grillo, R. Brescia, X. Ke, S. Bals, A. Catellani, et al., Direct Determination of Polarity, Faceting, and Core Location in Colloidal Core/Shell Wurtzite Semiconductor Nanocrystals, ACS Nano. 6 (2012) 6453–6461. doi:10.1021/nn302085t.

[2] G. Bertoni, J. Verbeeck, Accuracy and precision in model based EELS quantification., Ultramicroscopy. 108 (2008) 782–90. doi:10.1016/j.ultramic.2008.01.004.

[3] R. Young, The Rietveld Method, Oxford University Press, 1993.

[4] L. Lutterotti, MAUD program, (n.d.).

Aknowledgements

I would like to highlight this Thesis is the outcome of three years of hard work of mine and many other people, which I want to sincerely acknowledge.

First, I want to acknowledge my advisors Dr. Claudio Sangregorio for his competence and his support in the time of research and writing of this Thesis and Prof. Andrea Caneschi for his willingness.

Besides, I would like to express my sincere thanks to Dr. Alberto López-Ortega for generously sharing his time and knowledge in our three years long cooperative work and Dr. César de Julian Fernández for his impressive knowledge and motivation.

Last, but not least, I especially want to thanks all my office mates who shared with me all the best and hardest moments of being a PhD student and the LAMM staff for being so cooperative and welcoming.

Vorrei ringraziare la mia “estesa” famiglia per l’incoraggiamento, in particolare un grazie speciale ai i miei genitori per la loro costante fiducia, il loro supporto incondizionato e per il loro grande esempio.

Inoltre, vorrei ringraziare tutti gli amici che in modo diverso hanno contribuito a smorzare i fallimenti ed a gioire dei successi.

Questa sezione non potrebbe essere completa senza ringraziare Serena (+17...) e Claudio per aver reso speciali questi 9 anni di “chimica”.

Infine, ma non meno importante, voglio ringraziare Lorenzo per la sua comprensione ed il suo costante ed instancabile sostegno.